Modelling and Control of Doubly-Fed Induction Generator Systems in Wind Turbine Applications

by

Mwana Wa Kalaga Mbukani

Thesis presented in partial fulfilment of the requirements for the degree of Master of Engineering (Electrical) in the Faculty of Engineering at Stellenbosch University

Supervisor: Dr. N. Gule

March 2017

Declaration

By submitting this thesis electronically, I declare that the entirety of the work contained therein is my own, original work, that I am the sole author thereof (save to the extent explicitly otherwise stated), that reproduction and publication thereof by Stellenbosch University will not infringe any third party rights and that I have not previously in its entirety or in part submitted it for obtaining any qualification.

Date: March 2017

Abstract

The need to reduce the world's carbon foot print has led to a significant rise in wind energy generation. The doubly-fed induction generator (DFIG) is one of the most popular wind turbine generators partly due to its low rated back-to-back converter. A constant DC-link voltage in the doubly-fed induction generator system's back to back converter allows for bidirectional power flow of the rotor power. Hence, effective control of the DC-link voltage is necessary. The presence of the switching elements in the back-to-back converter creates harmonics in the systems. LCL and L filters are mostly used to mitigate the harmonics.

DFIGs are mainly connected to the grid, however, they can be used in stand-alone mode in isolated rural areas, where there are low loads with no grid connection. DFIGs in the stand-alone mode have to be controlled such that they provide voltage and frequency stability at varying load conditions and changing wind speeds.

In this thesis, the power control of the grid-connected DFIG systems in wind turbine applications is presented. Power factor regulation is conducted since it helps in the reduction of the costs linked to the capacitor bank. Maximum power point tracking is also investigated. DC-link voltage control is analysed whereby the grid-side converter is controlled as a voltage-source converter.

A comparative analysis of the LCL filter and L filter for switching frequencies below 5 kHz is done and described in this thesis. This is important for systems with low sampling frequencies. Furthermore, in this thesis, the control of a stand-alone DFIG together with simulation result, is presented. Experimental results are also given to demonstrate the effectiveness of the developed rotor-side control algorithm on a DFIG test bed.

Opsomming

Die behoefte om die wêreld se koolstof spoor te verminder het gelei tot 'n groot toename in die windopwekking van energie. Die dubbel-gevoerde induksie generator is een van die mees gewilde wind-turbine opwekkers, gedeeltelik weens die lae kapasiteit rug-aan-rug omsetter. Die konstante GS-bus spanning in die induksie generator sisteem se rug-aan-rug omsetter maak twee-rigting vloei van die rotordrywing moontlik. Daarom is doeltreffende beheer van die GS-bus spanning nodig. Die teenwoordigheid van die skakelelemente in die rug-aan-rug omsetter skep harmoniek in die sisteme. LCL en L filters word meestal gebruik om die harmoniek te verminder.

Dubbel-gevoerde induksie generators word meestal aan die network gekonnekteer, maar kan ook in alleen-staan modus gebruik word vir verafgeleë landelike gebiede met lae las en sonder network konneksies. Hierdie alleenstaande generators moet so beheer word dat hulle stabiele spanning en frekwersie onder verskillende lastoestande en windspoede kan verskaf.

In hierdie tesis word die beheer van die drywing in die network-verbinde Dubbel-gevoerde induksie generator sisteme in die windturbine toepassings bespreek. Regulering van die arbeidsfaktor word toegepas aangesien dit bydra tot die verlaging van kostes wat gekoppel is aan die kapasitorbank. Die maksimum drywingspunt opsporing word ook ondersoek. Die GS-bus spanningsbeheer word geanaliseer waar tyders die netwerk-kant se omsetter as 'n spanningsbron beheer word.

'n Vergelykende ontleding van die LCL en die L filters vir skakel frekwensies onder 5 kHz is gedoen en in hierdie tesis beskryf. Dit is belangrik, veral in sisteme met lae monster frekwensies. Die beheer van 'n alleenstaande Dubbel-gevoerde induksie generator en die simulasie resultate word beskryf. Die resultate van die eksperimente word gegee om die doeltreffendheid van die ontwerpte rotor kant beheer algoritme op n Dubbel-gevoerde induksie generator toetsbed demonstreer.

Acknowledgements

I would like to express my sincere gratitude to the following people:

- My supervisor Dr N. Gule for his trust and guidance throughout these two years.
- Everyone in the EMLab, for their suggestions and comments on this project.
- My family, for their unconditional love and invaluable support towards me.

Contents

List of Figures

List of Tables

Nomenclature

Acronyms

2S	Two-stage
3S	Three-stage
BESS	Battery energy storage system
CSP	Concentrating solar power
DPC	Direct power control
DTC	Direct torque control
DFIG	Doubly-fed induction generator
DFIM	Doubly-fed induction machine
DVC	Direct voltage control
EMF	Electromotive force
FOC	Field-oriented control
FPGA	Field programmable gate array
GSC	Grid-side converter
IG	Induction generator
IM	Induction machine
IVC	Indirect voltage control
LSC	Load-side converter
MPPT	Maximum power point tracking
PCC	Point of common coupling
PLL	Phase locked loop
PV	Photovoltaic
RSC	Rotor-side converter
SG	Synchronous generator
SV-PWM	Space vector pulse width modulation
THD	Total harmonic distortion
VI	Virtual instrument
VOC	Voltage-oriented control
VSC	Voltage-source converter

WECS	Wind energy conversion system

Symbols

f_s	Sampling frequency	[Hz]
i	Current	[A]
V_{dc}	DC-link voltage	[V]
v	Instantaneous voltage	[V]
θ	Rotation angle	[rad]
τ_{em}	Electromagnetic torque	[Nm]
τ_m	Mechanical torque	[Nm]
ψ	Flux linkage	[V/s]
P	Active power	[W]
Q	Reactive power	[Var]
s	slip	
ω_s	Stator angular speed	[rad/s]
ω_r	Rotor angular speed	[rad/s]
Ω_m	Mechanical angular speed	[rad/s]
ω_{slip}	slip angular speed	[rad/s]
T_s	Sampling period	[s]
p	Laplace operator	
t	Time	[s]

Subscripts

d	Real axis of the synchronous dq0-reference frame
m	Magnetising
q	Imaginary axis of the synchronous dq0-reference frame
s	With reference to the stator
r	With reference to the rotor
σ	Leakage
α	Real axis of the stationary $\alpha\beta$0-reference frame
β	Imaginary axis of the stationary $\alpha\beta$0-reference frame

Chapter 1

Introduction

In recent years, there has been an incredible rise in wind energy generation due to factors such as; the state policies on reducing the carbon footprint, the competitive cost of the wind-generated electricity and the environmental attributes [1]. A significant growth of the wind generation worldwide is depicted in Figure 1.1. It can be seen that there is a forecast of an increase in wind energy generation between year 2017 and 2020 of about 200 GW.

According to [4], South Africa is an ideal country for wind energy generation due to its plentiful wind resources, ample suitable sites and modern high voltage infrastructure. By the end of 2013, the installed wind energy capacity in South Africa was at 10 MW [4]. The South African Wind Energy Association estimates that by 2025, the wind energy might supply as much as 20 percent of the country's demand [4]. Furthermore, the country's long-term plan is to reach 8.4 GW in wind energy generation by 2030 [3, 4].

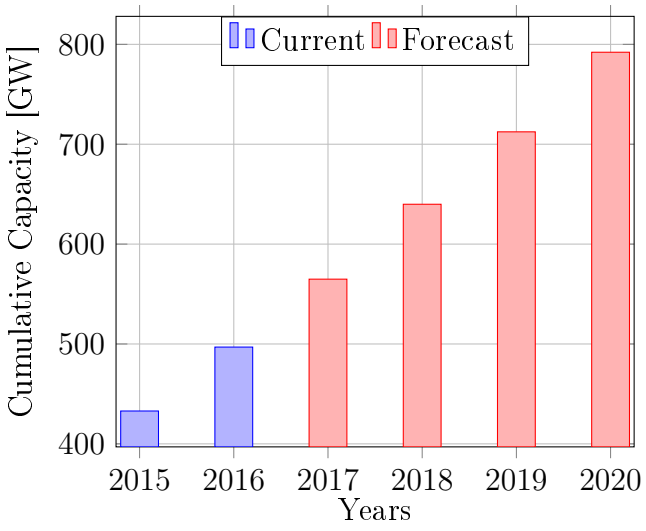

Figure 1.1: Estimated global cumulative installed capacity of wind energy [2]

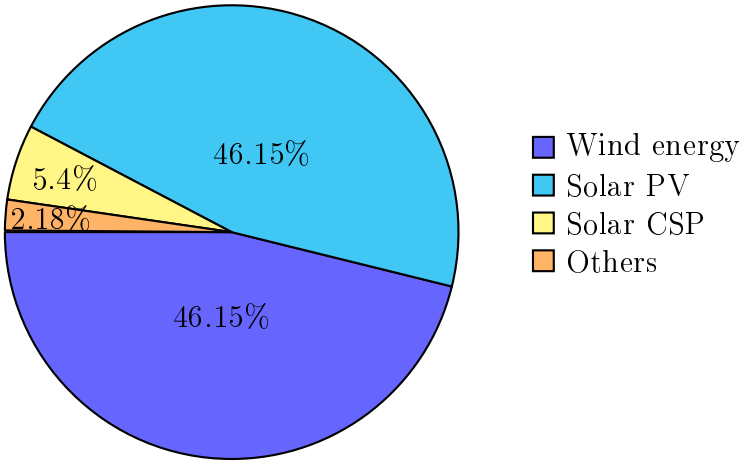

Figure 1.2: Projection of the installed renewable energy in South Africa by 2030 [3]

By 2030, the projection of the installed renewable energy in South Africa is depicted in Figure 1.2. It can be clearly seen that out of a total of 18.4 GW of renewable energy generation both the wind energy generation and solar photovoltaic (PV) accounts for 46.15 %. The concentrating solar power (CSP) represents 5.4 % while the electrical energy coming from other renewable energy sources (biomass, bio-gas, landfill gas, small hydro) represents 2.17 %.

Polinder et *al.* discussed the trends in wind turbine generator systems whereby the doubly-fed induction generator is the most popular wind turbine generators [5]. It is also argued that the doubly-fed induction machine remains one of the most sought after generator for the coming years [5] since it has the advantage of having the back-to-back converter rated at 30 % of the rated power of the generator [6].

Because of this popularity, especially in wind turbine applications, there has been extensive research on control systems of the doubly-fed induction generator. In the literature, research on pitch control and yawning control system of the wind turbines and the control systems of stand-alone and grid-connected wind energy conversion systems based on the doubly-fed induction generator (DFIG) can be found. In this thesis, only the control systems of wind energy conversion systems based on the DFIG (stand-alone mode and grid-connected mode) are considered. This thesis addresses the issues of the power regulation together with the power factor regulation and that of maximum power point tracking linked to the wind energy generation. Also, the stability of the voltage and frequency in stand-alone mode is discussed.

1.1 Literature Review

1.1.1 Grid-Connected DFIG System

The main components of the DFIG system is depicted in Figure 1.3. It can be seen that the grid-connected DFIG system is composed of the back-to-back converter. The rotor-side converter (RSC) is directly connected to the rotor of the DFIG. The grid-side converter (GSC) is connected to the grid through a filter in order to mitigate the harmonics generated by the back-to-back converter. The stator side of the DFIG and the output of the filter are connected to the grid through a transformer, as depicted in Figure 1.3. The transformer allows the doubly-fed induction generator system to match the grid voltage level. The switching elements of the grid-side converter and the rotor-side converter are controlled by the grid-side converter control and the rotor-side converter control, as depicted in Figure 1.4.

1.1.1.1 Rotor-Side Converter Control

There has been several vector control techniques discussed and presented for grid-connected DFIG systems in wind turbine applications. Generally, the vector control of the grid-connected doubly-fed induction generator system in wind energy conversion system consists of controlling the rotor currents using the alignment of the rotating dq0-reference frame along the stator flux space vector (field-oriented control) [7–10] or the stator voltage space vector (voltage-orientated control) [11, 12].

The field-oriented control technique is the most popular vector control technique used in WECS based on the DFIG [7]. Vector control based on stator flux-oriented control of WECS based on the DFIG was developed in [8]. Although, field-oriented vector control is popularly used, a discussion on the feasibility of the stator voltage-oriented control (VOC) is proposed in [11], but

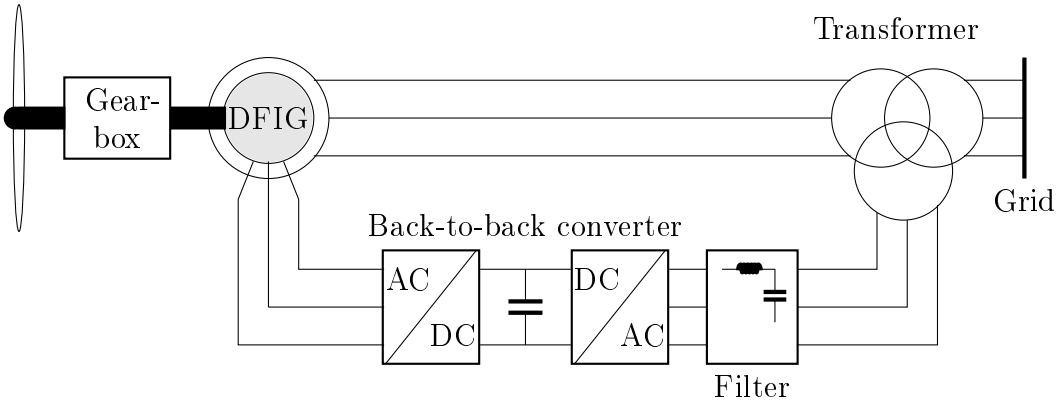

Figure 1.3: Grid-connected DFIG system schematic

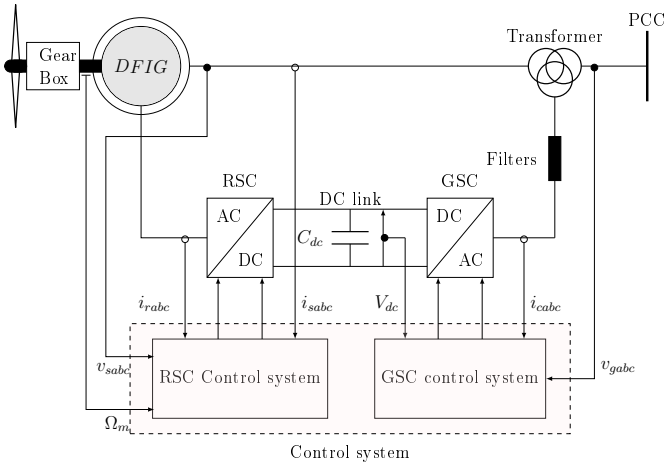

Figure 1.4: Control scheme of the DFIG system

only speed control was considered [11]. Through various operating conditions, a good performance of the proposed control strategy is also shown.

The stability study of the DFIG control using the VOC was conducted in [12], where the authors concluded that for the inner current control, the size of the magnetising inductance is critical for the area where the DFIG is stable and that of the stator resistance is critical for the tuning of the inner PI controller where better damping of the poles of the systems can be achieved. In [13], the authors discussed an encoder-less control of the active and reactive powers of the grid-connected DFIG using a rotor position phase locked loop. Also, the MPPT is achieved with the proposed control strategy [13]. A sensorless control of a single voltage-source converter (VSC) of a grid-connected DFIG using the stator flux-based model reference adaptive system algorithm is discussed in [14], where it is found that when comparing the traditional configuration of the DFIG and that of a single VSC, the generated active and reactive powers are almost similar.

A survey of the control techniques in grid-connected DFIG systems was conducted in order to satisfy the grid code in [15], where it is highlighted that the advanced control using the field-oriented control (FOC), the direct torque control (DTC) and the direct power control (DPC) are still necessary to improve the performance of the DFIG system during steady state and transient operating conditions [15]. However, the new grid code requires the wind turbines to remain connected during grid faults. Hence, the fault-ride-through control strategies are also important [15]. The fault-ride-through grid code of the grid-connected DFIG system is discussed in [16].

For a typical variable-speed wind turbine, the optimum power captured by the wind turbine is directly proportional to the cubic of the rotational speed of the turbine [8, 9, 17]. The MPPT control algorithm for power regulation is

discussed in [17], where the aim is to regulate the power factor of the overall wind turbine.

1.1.1.2 Grid-Side Converter Control

The aims of the grid-side converter (GSC) control in DFIG systems are to maintain the DC-link voltage approximately to a constant value in order to allow a bidirectional power flow of the rotor power. Another aim of the GSC is the power factor regulation. Here, the vector control technique is mostly adopted to this end. The grid-side converter control is similar to that of the voltage-source converters (VSC) [8]. The GSCs operate mostly under unity power factor and the GSC in WECS based on the DFIG are mostly pulse width modulation (PWM) converter current regulated [7, 18]. An analysis of the decoupled d-q control of the DFIG control algorithm was conducted in [19], where the authors found that the active and reactive powers control of the GSC depends on the nature of the line to which the DFIG system is connected.

1.1.2 Stand-Alone DFIG System

The stand-alone DFIG system schematic is depicted in Figure 1.5. As shown in the figure, an auxiliary DC source which provides the initial excitation current is connected to the DC bus. Further, the stand-alone DFIG system is connected directly to the loads (linear loads, non-linear loads). The control of the load-side converter (LSC) in stand-alone DFIG systems is similar to that of the grid-side converter in grid-connected DFIg systems except that in stand-alone mode the LSC control can be extended to include harmonic mitigation.

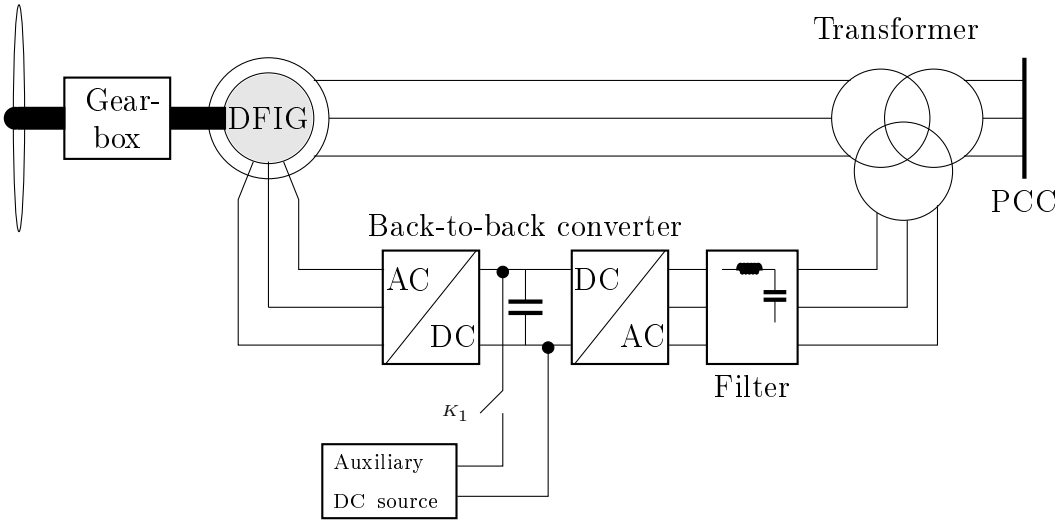

Figure 1.5: Stand-alone DFIG system schematic

1.1.2.1 Rotor-Side Converter Control

In stand-alone operating conditions the voltage and frequency stability are amongst the main issues since the system is not connected to a grid anymore. Pena et *al* investigated the stand-alone operation of DFIG system in wind turbine operation [20]. They proposed the control of the voltage magnitude by regulating the magnetising current using the rotor current [20]. Given the fact that there is no synchronisation needed the same authors suggested that the system frequency can be fixed by assigning a constant value using the control algorithm.

On the other hand, the direct voltage control (DVC) is suggested in [21], where the voltage magnitude is directly regulated. The advantage of this control method is that it does not depend on the system parameters as they change during the functioning of the machine [21]. Besides, the control strategy on for the frequency stability is similar to that discussed in [20]. They found that the direct voltage control shows better accuracy than the method discussed in [20].

In [22], the authors discussed about the control of the stand-alone operations of the DFIG system in an isolated island. Aktarujjaman et *al.* analysed the DFIG system in stand-alone mode with a battery energy storage system (BESS). The BESS permitted an optimal frequency stability with the use of f–P and Q–V droop characteristics together with a dump load [22]. The drawback of this control method is the cost of the BESS and the so called advantage of the DFIG systems with 30 % of the rated power of the generator since the back-to-back converter should handle the extra-power of the BESS. Similar approach is discussed in [23], where Ooi and Zhang analysed the synchronisation when there is lost of the main grid and how the stand-alone DFIG system has to maintain the voltage and frequency [23]. They included a secondary control algorithm in case the main grid is lost [23]. A good performance of the control algorithm is shown.

Other issues in stand-alone mode are the power quality since the load in stand-alone are mostly unbalanced and non-linear. In order to address these issues together with the voltage and frequency stability, Koczara and Iwanski proposed a control system which includes the positive sequence and negative sequence [24]. The positive sequence consists of the main control (voltage frequency and magnitude regulation). The secondary control system focuses on voltage asymmetry correction. Similar to the DVC used in [21], Jain and Ranganathan proposed not only a control algorithm to maintain the voltage and frequency stability but also they included an active filtering using the shunt active filtering [25]. An experimental implementation of the stand-alone DFIG system is described in [26], where the authors compare the stand-alone DFIG system with and without a BESS. It was found that the stand-alone

DFIG system with a BESS is able to extract maximum power compared to the conventional ones.

1.1.3 Harmonic Filtering

The back-to-back converter are one of the components of the doubly-fed induction generator systems. The back-to-back converter is composed of switching elements that are the main source of harmonics in the power system. In order to connect the VSCs to the grid, it is mandatory to comply with the IEEE standard 519-2014 in terms of the harmonics. Passive filters are the most popular option, when it comes to mitigate the harmonics in the power system. The most common filter is the L filter which consists of only an inductance. Although the LC filter can be used in order to mitigate high frequency harmonics, the LCL filter is the most sustainable filter. The LCL filter is the most suitable due to its low cost because of the reduced size of the inductance compared to the L filter.

There are two different trends in terms of the design of the LCL filter. Some authors use the LCL conventional filter based on the LCL filter having its resonant frequency between ten times the line frequency and half the switching frequency [27–30]. On the other hand, some authors suggested the LCL filter design using optimisation methods [28, 31] where Piasecki et *al.* used the multi-objective optimisation while Zeng et *al.* considered the optimisation of the quality index which includes all the performance factors of the LCL filter. Compared to the the conventional LCL filter deign method, the latest method takes into consideration the physical filter size (core, conductor size...).

In addition, there have been research on the topology of the LCL filters in order to reduce the inductance sizes. in [32], an LCL-LC filter topology is suggested together with parameters design methods. Compared to the conventional LCL filter topology, the proposed topology provides better performance with smaller inductance size. Wang and Wu suggested a L-LCL filter topology together with is design method [33]. The proposed L-LCL filter shows good performance.

Recently, a review on LCL filter is discussed in [34] where it is highlighted that most research on LCL filter has been done for switching frequencies higher than 5 kHz. The performance of the LCL filter for the switching frequencies less than 5 kHz has not been investigated yet. Hence, an investigation on the LCL filter performance for lower switching frequencies and the design of the LCL filter is investigated in this thesis. In addition a comprehensive design procedure is given, together with the control of the grid connected voltage-source converter based on the design LCL filter.

1.2 Aims and Objectives

The aims of this research project are the modelling of the wind energy conversion system (WECS) based on DFIG system (in grid-connected and stand-alone mode); the design of the control strategies of the WECS based on the DFIG (in grid-connected and stand-alone mode); and, the experimental implementation of the proposed control algorithm of the WECS based on the DFIG. In order to achieve these aims the objectives of this thesis are as follows;

- Model of the wind energy conversion system based on the DFIG system;
- Design of the LCL filter;
- Comparative study of the L and LCL filter for switching frequencies less than 5 kHz;
- Control of the grid/load-side converter ;
- Control of the rotor-side converter of the WECS based on the DFIG(in stand-alone mode and grid-connected mode);
- Test the developed control algorithm of the rotor-side converter in grid-connected WECS based on the DFIG in the laboratory.

1.3 Scope of the Research Project

Due to the time constraint, only the inner current controller of the RSC in grid-connected WECS based on the DFIG was implemented in the laboratory.

1.4 Contributions

The contributions of this thesis are:

- A comparative study based of effectiveness factors between the LCL filter and the L filter designed for switching frequencies lower than 5 kHz is discussed in Chapter 3.
- A control algorithm of the rotor-side converter based on voltage-oriented control without the sensors of the three-phase stator current is proposed in Chapter 4. The proposed control algorithm regulates the stator active and reactive powers using the three-phase rotor current in grid-connected mode. The regulation of the stator power factor is also provided by the proposed control algorithm.

1.5 List of Publications

MWK. Mbukani, N. Gule, "Analysis and control of a grid-connected three-phase PWM voltage-source converters based on LCL filter," *Southern African Universities Power Engineering Conference (SAUPEC)* (accepted for publication).

MWK. Mbukani, N. Gule, "Investigation of the stator voltage-oriented vector control of the rotor side converter in DFIG systems," *Southern African Universities Power Engineering Conference (SAUPEC)* (accepted for publication).

1.6 Thesis Outline

The remainder of the thesis is organised as follows;

- **Chapter 2**: In this chapter, a thorough model of the wind energy conversion system based on the DFIG is described. Further, the DFIG dynamic model is simulated in MATLAB/SIMULINK.
- **Chapter 3**: The control algorithm of the grid-side converter is discussed. In addition, a comprehensive LCL filter design procedure and a design example are also presented. The design procedure of the PI controllers is also discussed. Moreover, Simulation of the grid-side converter during dynamic operating conditions are also displayed. Furthermore, a comparative study of L filter and LCL filter for switching frequency less than 5 kHz is also presented.
- **Chapter 4**: The control strategies of the rotor-side converter in both stand-alone and grid-connected WECS based on the DFIG are presented in this chapter. Further, a design method for the PI controller is also described. Finally, the performances of the RSC for both stand-alone and grid-connected DFIG systems through simulations in MATLAB/SIMULINK are provided.
- **Chapter 5**: In this chapter, the description of the test bench is provided. The hardware and software details are also described. Further, the testing of the performance of the inner current controller of the grid-connected WECS based on the DFIG discussed in Chapter 4 is provided.
- **Chapter 6**: The conclusion is drawn with regards to the findings. Moreover, the possibilities of future research are also discussed.

Chapter 2

DFIG-Based WECS Modelling

An overview of the modelling of a doubly-fed induction generator (DFIG) system is presented in this chapter. Also, the dynamic models of the relevant systems helping in the control algorithm of the DFIG system are given. The modelling of the DFIG systems described in this chapter is based on [35, 36].

2.1 Wind Turbine Systems

Several wind energy conversion system (WECS) topologies exist depending on the generator technology and the intended applications. The WECSs can also be distinguished by the fact that some operate at fixed speed and some at variable speed. The fixed-speed WECS are directly connected to the grid and they achieve optimum aerodynamic efficiency at a single wind speed while the variable-speed WECS are connected to the grid through a back-to-back converter and can achieve optimum aerodynamic efficiency with several wind speeds. Also, one can distinguish between direct-drive WECSs and geared WECSs by the presence or not of a gearbox.

2.1.1 Fixed-Speed Wind Turbine

The fixed-speed wind turbine based on the induction generator (IG) is depicted in Figure 2.1, where the wind turbine generator is connected to the grid through a soft starter and a transformer. Also, a capacitor bank connected in parallel to regulate the power factor of the fixed-speed wind turbine generator, as displayed Figure 2.1. The rotor speed depends directly on the gearbox and the pole-pairs of the IG. Hence, this results on a reduced magnetising losses at low wind speed. However, the downside of the fixed-speed wind turbine is that it has to operate with a constant speed even when the wind speed varies. The fixed-speed wind turbine based on the IG led the wind market until 2003 [37]. The absence of the gearbox reduces considerably the weight and the losses associated with the gearbox [38].

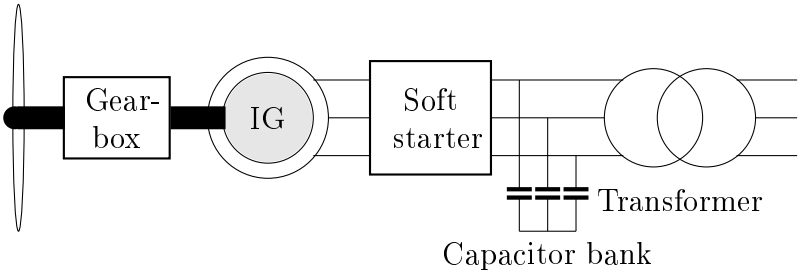

Figure 2.1: Fixed-speed wind turbine with an induction generator

2.1.2 Variable-Speed Wind Turbine

The variable-speed wind turbine with a gearbox is shown in Figure 2.2. The wind turbine is connected to the grid through the transformer and the back-to-back converter. The presence of the back-to-back converter allows the wind turbine to operates at fixed frequency regardless of the wind speed. They are mostly equipped with DFIGs and PMGs [37]. The advantage of the system depicted in Figure 2.2 is its well developed robust control.

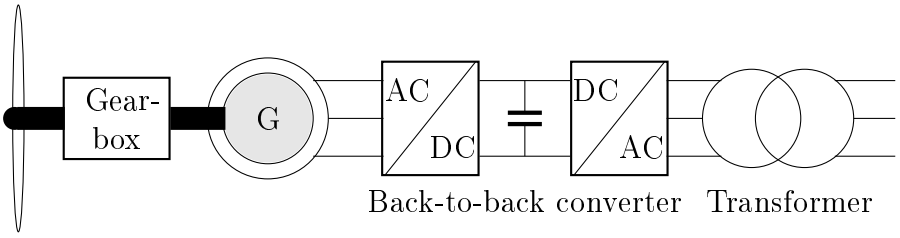

Figure 2.2: Variable-speed wind turbine

Since the gearbox makes the wind turbine heavier, it has a lower reliability. The system shown in Figure 2.3 is more reliable for wind generators that have more pole-pairs such as the synchronous generator and the permanent magnet synchronous generator whereby the rotor speed will depend on the pole-pairs.

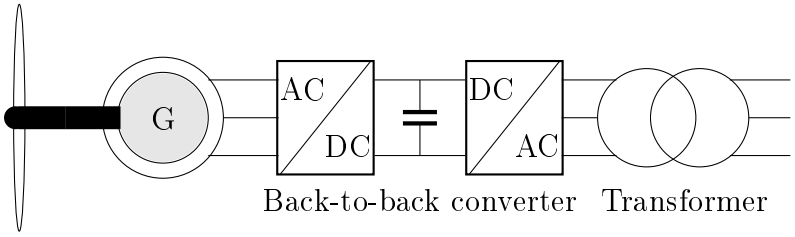

Figure 2.3: Variable-speed wind turbine (gearbox-less)

2.1.3 Variable-Speed Wind Turbine based on the DFIG

The variable-speed wind turbine equipped with the DFIG is shown in Figure 2.4. This system consists of the doubly-fed induction generator (DFIG), the back-to-back converter (grid-side converter and rotor-side converter), the DC-link bus, and the transformer. In this configuration, the back-to-back converter is rated at 30 % of the rated power of the generator. However, the downside of this system is that since the stator of the DFIG is directly connected to the grid, there is a need for synchronisation compared to the system discussed in Section 2.1.2. Also, since the rotor of the DFIG consumes power at sub-synchronous operating conditions, this system has a lower efficiency when operating at that particular operating condition.

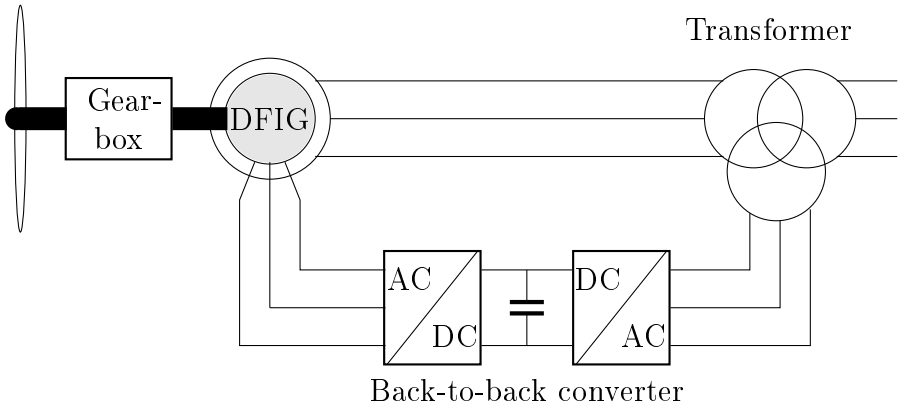

Figure 2.4: Common configuration of DFIG system

2.2 Wind Turbine Generators

In WECS, the DFIG, the permanent mangent generator (PMG) and the synchronous generator (SG) are the most popular wind turbine generators [39]. A comparison of three generators in WECS (the 3-stage (3S) geared DFIG, the direct-drive (DD) SG and the DD PMG with regards to weight, cost and losses is displayed in Table 2.1. It can be seen that the weight of the WECS-based direct-drive PMG is roughly four times higher than that of the WECS-based

Table 2.1: Comparison between three generators published in [40]

	3S geared DFIG	Direct drive SG	Direct drive PMG
Weight	100%	≈850 %	≈450 %
Stator radius	100%	≈600 %	≈600 %
Estimation of the total cost	100%	120%	≈105%
Power losses	100%	95%	≈65%

of the 3-stage geared DFIG. For the same power, the stator diameter of the WECS-based on direct-drive PMG is about six times higher than that of a DFIG, as shown in Table 2.1. The typical composition of wind turbine is displayed in Figure 2.5 where each component of the WECS is clearly highlighted.

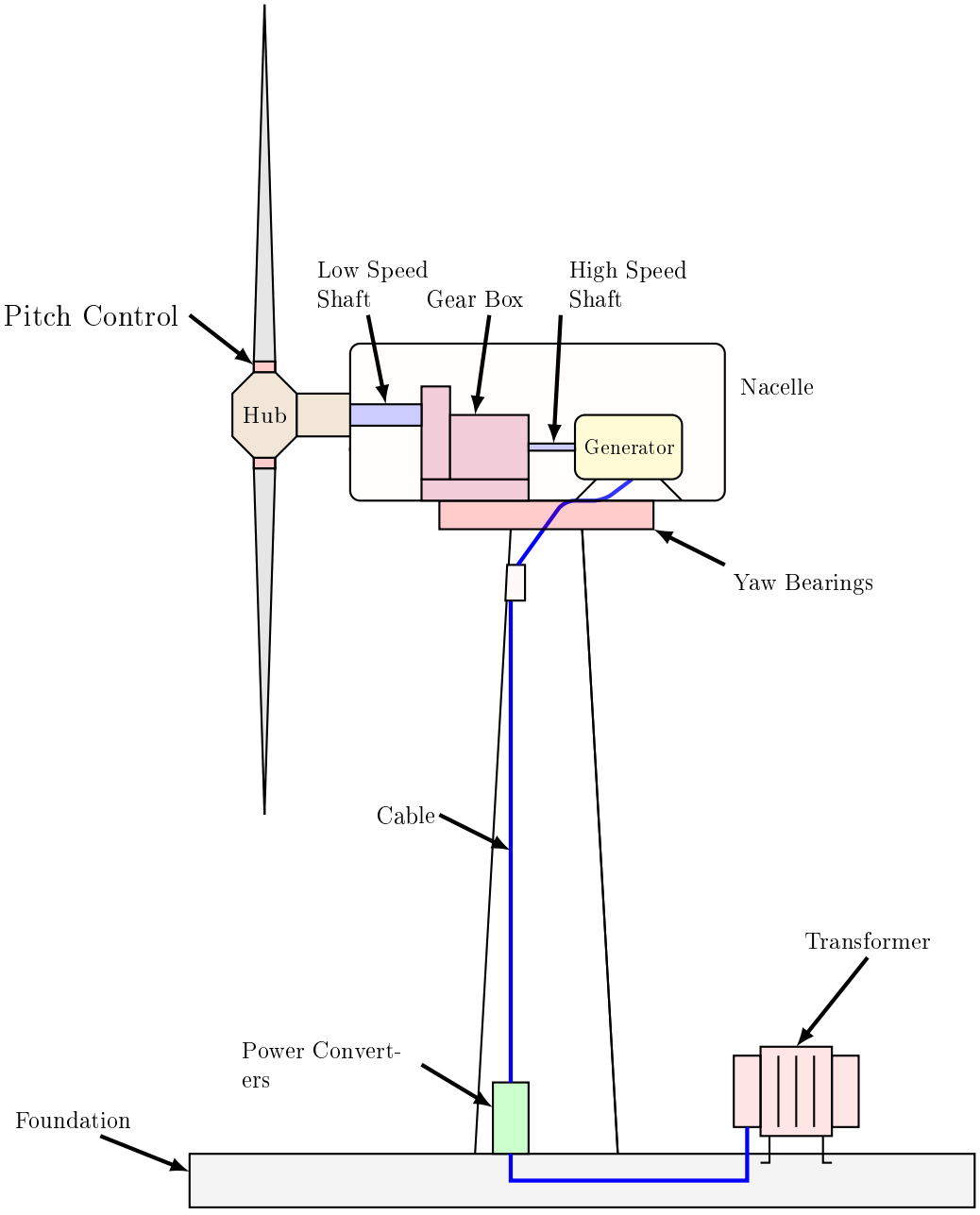

Figure 2.5: Schematic diagram of wind turbine component

2.3 Aerodynamic Conversion

The mechanical power captured by the wind turbine is given by

$$P_m = \frac{1}{2} C_p \rho \pi r^2 V_{wind}^3, \tag{2.1}$$

where C_p is the power coefficient; r is the radius of the turbine propeller; V_{wind} is the wind speed; and, ρ is the air density. The power coefficient expresses the ratio between the power captured by the wind turbine and the total wind power available. This power coefficient (C_p) is a function of the tip-speed ratio and the pitch angle. It is worth noticing that there is a maximum power coefficient which optimises the capture of mechanical power for a given wind turbine. The tip-speed ratio is given by

$$\lambda = \frac{\Omega_m r}{m V_{wind}}, \tag{2.2}$$

where Ω_m is the mechanical shaft speed of the generator; m is the gear-box ration. The power coefficient can be approximated as [41];

$$C_p = 0.73\Big(\frac{151}{\lambda_k} - 0.58\beta - 0.002\beta^{2.14} - 13.2\Big)e^{-18.5\lambda_k}, \tag{2.3}$$

with

$$\frac{1}{\lambda_k} = \frac{1}{\frac{1}{\lambda - 0.02\beta} - \frac{0.003}{\beta^3+1}}, \tag{2.4}$$

where λ is the tip speed ratio and β is the pitch angle. The power coefficient is a specific characteristic of a given wind turbine. An example of a typical relationship between the power coefficient and the tip-speed ratio is depicted in Figure 2.6.

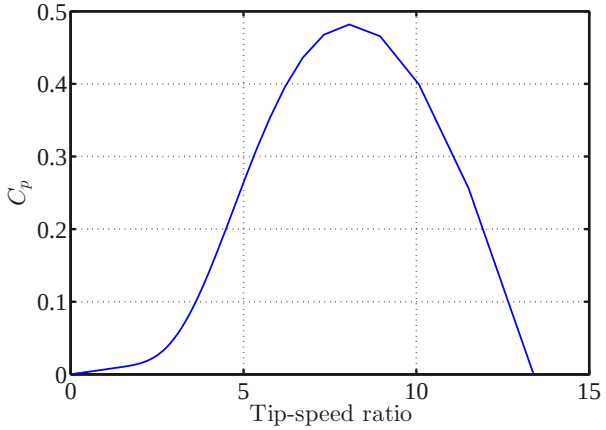

Figure 2.6: Tip-speed ratio(λ) versus power coefficient(C_p)

2.4 Working Principle of The Doubly-Fed Induction Machine

The doubly-fed induction machine (DFIM) is an induction machine that can be fed from the stator terminals as well as from the rotor terminals at the same time. For the following discussions, it is assumed that the stator and rotor windings are sinusoidally distributed and the air gap is uniform. When the stator windings are directly connected to a stiff grid in case of grid-connected DFIM, the stator voltage pulsates at the grid/stator frequency. The working principle of a doubly-fed induction machine with different frequency levels (with f_s for the stator/grid side and f_r for the rotor side) is displayed in Figure 2.7. The frequency of the stator voltage is given by

$$\omega_s = 2\pi f_s, \tag{2.5}$$

where f_s is the fixed grid/stator frequency. When the rotor of the DFIM rotates, there is an induced electromotive force (EMF) in the rotor windings that rotates at slip frequency. Since the induced EMF in the rotor windings depends on the relative speed between the stator frequency and the electrical rotor shaft speed, both the current and voltage in the rotor windings will depend on the slip angular speed. The slip angular frequency is given by

$$\omega_{slip} = \omega_s - \omega_r, \tag{2.6}$$

where ω_{slip} is the slip angular frequency and ω_r is the electrical angular shaft speed. The common term used to describe the relationship between the stator angular speed and the electrical angular shaft speeds is given by

$$s = \frac{\omega_s - \omega_r}{\omega_r}, \tag{2.7}$$

where s is the slip. The relationship between the mechanical and the electrical angular shaft speed is given by

$$\omega_r = \left(\frac{P}{2}\right)\Omega_m, \tag{2.8}$$

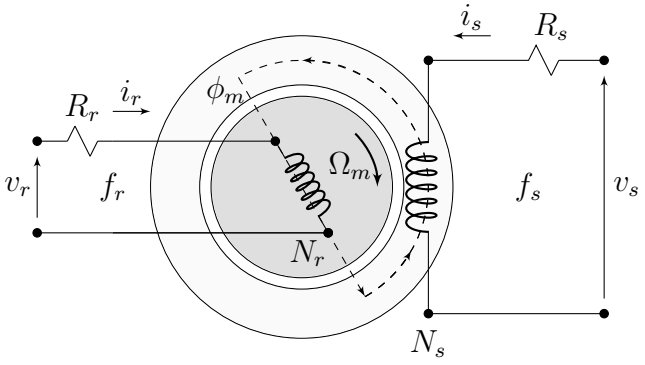

Figure 2.7: Single-phase doubly-fed induction machine representation

where P represents the number of poles in the stator of the DFIG and Ω_m denotes the mechanical shaft speed.

There are three operating conditions of the DFIM depending on the rotor shaft speed. They are the sub-synchronous mode , the super-synchronous mode and the synchronous mode. The relationship between the angular slip frequency and the stator angular frequency is given by

$$\omega_{slip} = s\omega_s. \tag{2.9}$$

Furthermore, the relationship between the stator frequency and slip frequency can be expressed as

$$f_{slip} = sf_s, \tag{2.10}$$

where f_{slip} is the slip frequency.

2.5 Power Flow in DFIG Systems

As mentioned in Section 2.4, three operating modes with each having a specific power flow can be distinguished. These are the synchronous operating mode, the super-synchronous operating mode and the sub-synchronous operating mode. The signs of different power according to the operating mode in DFIG system are displayed in Table 2.2. P_s is the electrical stator power, s is the slip and P_r is the rotor electrical power, and P_m is the mechanical power. Without going any deeper, the rotor electrical power can be expressed as a function of the stator power. The rotor power can be expressed as

$$P_r = -sP_s. \tag{2.11}$$

And, the total power generated by the lossless DFIG system is given by

$$P_g = P_s + P_r = (1 - s)P_s, \tag{2.12}$$

where P_g is the total power generated by the DFIG system. From Equation (2.11), it can be seen that, the sign of the rotor active power (generated or consumed) depends on the sign of the slip. It is negative when the system operates in super-synchronous operating mode and positive when the system operates in sub-synchronous mode.

Table 2.2: Generated Power signs

slip range	Operating modes	Power sign
$0 < s < 1$	sub-synchronous mode	$P_s > 0$,$P_r < 0$ and $P_m > 0$
$s = 0$	synchronous mode	$P_s > 0$, $P_r = 0$ and $P_m > 0$
$s > 0$	super-synchronous mode	$P_s > 0$,$P_s > 0$ and $P_m > 0$

A. Synchronous Operating Mode

In synchronous mode, the slip is zero, the electrical angular shaft speed is equal to the stator angular speed. As a consequence, there is no induced EMF in the rotor windings since this EMF in the rotor windings depends on the relative speed between the stator angular speed and the electrical shaft speed. Thus the DFIG acts as a synchronous generator. This operating mode does not allow for the production of power from the rotor side of the DFIG. For a lossless DFIG system, the power flow in this operating mode is illustrated in Figure 2.8. From Equation (2.11), it can be seen that the total power generated by the lossless DFIG system is composed only of the stator power.

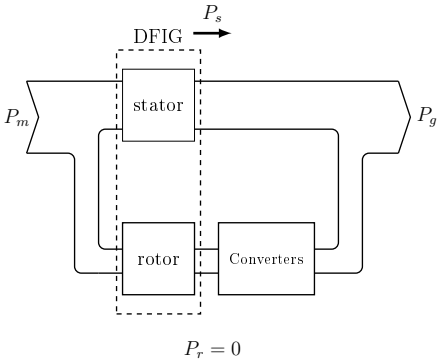

Figure 2.8: Power flow scheme in synchronous operating mode

B. Sub-synchronous Operating Mode

In sub-synchronous operating mode, the electrical angular shaft speed is less than that of the stator flux. Hence the slip is positive. In this operating mode, the rotor consumes the power coming from the grid. The power flow scheme of the sub-synchronous operating mode is depicted in Figure 2.9. When the DFIG operates in sub-synchronous mode the slip is positive

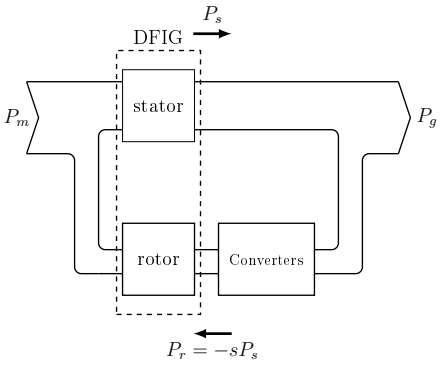

Figure 2.9: Power flow scheme in sub-synchronous operating mode

and therefore the rotor consumes the power passing through the DC-link capacitor from the grid. The DC-link capacitor is used as the storage element in the DFIG system.

C. Super-synchronous Operating Mode

In super-synchronous operating mode the slip is negative. Both the stator and rotor side of the DFIG supply active power to the grid. The total power is composed of the stator power and the rotor power. In super-synchronous operating mode, the rotor side of the DFIG provides the active power to the grid through the DC-link bus. As a consequence, the DC-link voltage tends to increase, this is the reason why the control of the grid-side converter is meant to maintain the DC-link voltage constant.

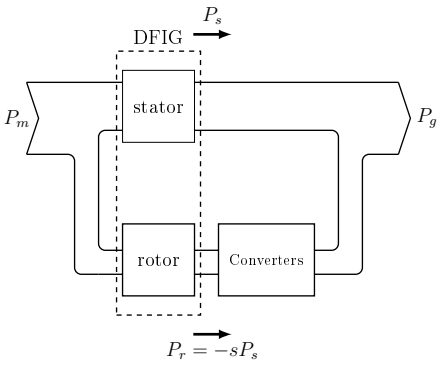

Figure 2.10: Power flow scheme in super-synchronous operating mode

2.6 Modelling of the Doubly-Fed Induction Generators

In this section, it is assumed the DFIG is symmetrical and that its windings are ideal. The relationships between different entities are given in the ABC reference frame as well as in the synchronous dq0-reference frame. Furthermore, an example of how the machine behaves during free acceleration is given.

2.6.1 DFIG modelling in ABC reference frame

The induction machine scheme is illustrated in Figure 2.11. In Figure 2.11, $\boldsymbol{v_{sabc}}$ and $\boldsymbol{v_{rabc}}$ are the instantaneous three-phase stator and rotor voltages, respectively; and, $\boldsymbol{i_{sabc}}$ and $\boldsymbol{i_{rabc}}$ are the three-phase stator and rotor currents, respectively. Using Faraday and Kirchoff's laws in the stator and rotor windings of the DFIG, the voltage equations of the induction machine are given by

$$\boldsymbol{v_{sabc}} = \boldsymbol{R_s i_{sabc}} + \frac{d\boldsymbol{\psi_{sabc}}}{dt} \tag{2.13}$$

and

$$\boldsymbol{v_{rabc}} = \boldsymbol{R_r i_{rabc}} + \frac{d\boldsymbol{\psi_{rabc}}}{dt}, \tag{2.14}$$

where $\boldsymbol{\psi_{sabc}}$ and $\boldsymbol{\psi_{rabc}}$ express the three-phase rotor and stator flux linkages, respectively; In the above equations where

$$(\boldsymbol{f_{sabc}})^T = \begin{bmatrix} f_{sa} & f_{sb} & f_{sc} \end{bmatrix} \tag{2.15}$$

$$(\boldsymbol{f_{sabc}})^T = \begin{bmatrix} f_{ra} & f_{rb} & f_{rc} \end{bmatrix}, \tag{2.16}$$

where $\boldsymbol{f}$ denotes the current, the voltage and the flux linkage. The superscript T expresses the transpose term. The subscripts s and r denote the parameters from the stator and rotor. $\boldsymbol{R_s}$ and $\boldsymbol{R_r}$ are the diagonal matrix with stator

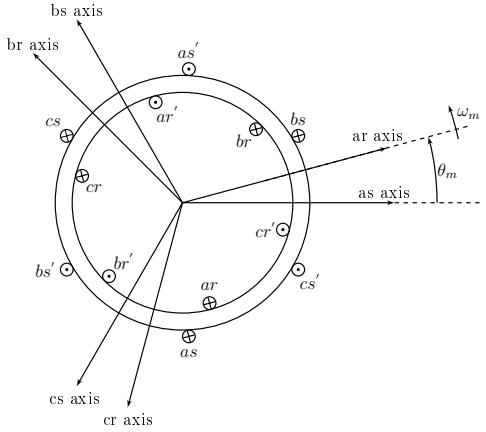

(a) Induction machine scheme

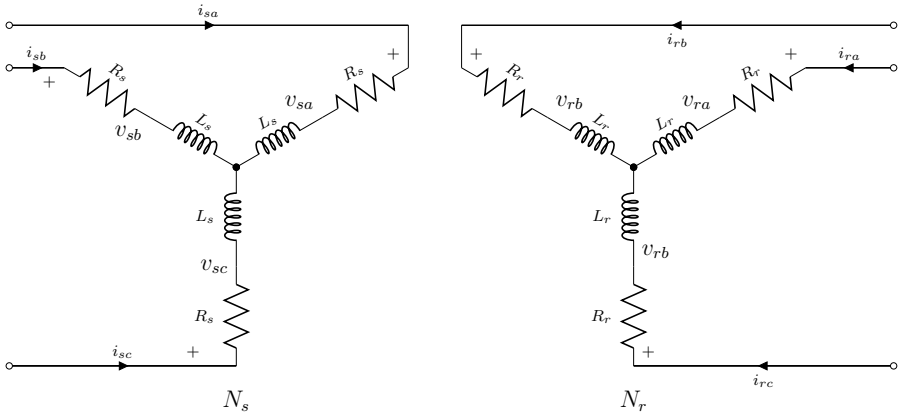

(b) Wye-connected symmetrical induction machine windings scheme

Figure 2.11: Induction machine scheme:

resistance and rotor resistance as elements, respectively. The rotor resistance and stator resistances are given by

$$\boldsymbol{R_s} = \begin{bmatrix} R_s & 0 & 0 \\ 0 & R_s & 0 \\ 0 & 0 & R_s \end{bmatrix} \tag{2.17}$$

and

$$\boldsymbol{R_r} = \begin{bmatrix} R_r & 0 & 0 \\ 0 & R_r & 0 \\ 0 & 0 & R_r \end{bmatrix}, \tag{2.18}$$

where R_s and R_s are the per-phase stator and rotor resistances. When referring all the rotor parameters to stator, the expression of the rotor voltage is given by

$$\boldsymbol{v'_{rabc}} = \boldsymbol{R'_r i'_{rabc}} + \frac{d\boldsymbol{\psi'_{rabc}}}{dt}, \tag{2.19}$$

where

$$\boldsymbol{v'_{rabc}} = \frac{N_s}{N_r}\boldsymbol{v_{rabc}}, \qquad \boldsymbol{i'_{rabc}} = \frac{N_r}{N_s}\boldsymbol{i_{rabc}}, \qquad \boldsymbol{\psi'_{rabc}} = \frac{N_s}{N_r}\boldsymbol{\psi_{rabc}}, \tag{2.20}$$

and

$$\boldsymbol{R'_r} = \left(\frac{N_s}{N_r}\right)^2 \boldsymbol{R_r}, \tag{2.21}$$

where the superscript ' denotes the rotor parameters referred to the stator.

The three-phase flux linkages can be expressed as a function of the three-phase currents and the inductances by

$$\begin{bmatrix} \boldsymbol{\psi_{sabc}} \\ \boldsymbol{\psi'_{rabc}} \end{bmatrix} = \begin{bmatrix} \boldsymbol{L_s} & \boldsymbol{L'_{sr}} \\ (\boldsymbol{L'_{rs}})^t & \boldsymbol{L'_r} \end{bmatrix} \begin{bmatrix} \boldsymbol{i_{sabc}} \\ \boldsymbol{i'_{rabc}} \end{bmatrix}. \tag{2.22}$$

In Equation (2.22), the winding inductances of the DFIG are given by

$$\boldsymbol{L_s} = \begin{bmatrix} L_{sl} + L_{sm} & -\frac{1}{2}L_{sm} & -\frac{1}{2}L_{sm} \\ -\frac{1}{2}L_{sm} & L_{sl} + L_{sm} & -\frac{1}{2}L_{sm} \\ -\frac{1}{2}L_{sm} & -\frac{1}{2}L_{sm} & L_{sl} + L_{sm} \end{bmatrix}, \tag{2.23}$$

$$\boldsymbol{L'_{sr}} = \frac{N_s}{N_r}L_{sr} = L_{sm}\begin{bmatrix} \cos\theta_r & \cos(\theta_r + \frac{2\pi}{3}) & \cos(\theta_r - \frac{2\pi}{3}) \\ \cos(\theta_r - \frac{2\pi}{3}) & \cos\theta_r & \cos(\theta_r + \frac{2\pi}{3}) \\ \cos(\theta_r + \frac{2\pi}{3}) & \cos(\theta_r - \frac{2\pi}{3}) & \cos\theta_r \end{bmatrix}, \tag{2.24}$$

and

$$\boldsymbol{L'_r} = \left(\frac{N_s}{N_r}\right)^2 \boldsymbol{L_r} = \begin{bmatrix} L'_{rl} + L_{sm} & -\frac{1}{2}L_{sm} & -\frac{1}{2}L_{sm} \\ -\frac{1}{2}L_{sm} & L'_{rl} + L_{sm} & -\frac{1}{2}L_{sm} \\ -\frac{1}{2}L_{sm} & -\frac{1}{2}L_{sm} & L'_{rl} + L_{sm} \end{bmatrix}. \tag{2.25}$$

In Equation (2.23)−((2.25)), L_{sl} and L_{sm} are the leakage and magnetising inductances of the stator windings, respectively. $L_{sr}^{'}$ is the amplitude of the mutual inductance of the stator and rotor windings. $L_{rl}^{'}$ is the leakage inductance of the rotor windings referred to the stator windings. From Equation (2.24), it can be noted that the mutual inductance of the stator windings and the rotor windings depend on the rotor angle. The electrical rotor angle is given by

$$\theta_r = \int_0^t \omega_r dt + \theta_r(0), \tag{2.26}$$

where $\theta_r(0)$ is the initial value of the electrical rotor angle. The electrical rotor angle is time dependant. Hence, it is necessary to transform the machine variables and parameters into a reference frame that makes the mutual inductances of the stator and rotor windings to be considered constant.

2.6.2 DFIG Modelling in dq0-reference Frame

The reference frames can be used for machine variable transformation in order to eliminate the time dependency of the mutual inductance of the machine. Some reference frames are displayed in Figure 2.12. In Figure 2.12, (α, β) is the stationary reference frame which can be considered as the stator reference frame; (d_s, q_s) is the synchronous reference frame; and, (d_r, q_r) is the rotating reference frame linked to the rotor.

The transformation of stator variables into an arbitrary dq0-reference frame is given by

$$\boldsymbol{f_{sdq0}} = \vec{f} = \boldsymbol{T_s} \boldsymbol{f_{sabc}}, \tag{2.27}$$

where

$$\boldsymbol{T_s} = \sqrt{\frac{2}{3}} \begin{bmatrix} \cos(\theta_{dq}) & \cos(\theta_{dq} - \frac{2\pi}{3}) & \cos(\theta_{dq} + \frac{2\pi}{3}) \\ \sin(\theta_{dq}) & \sin(\theta_{dq} - \frac{2\pi}{3}) & \sin(\theta_{dq} + \frac{2\pi}{3}) \\ \frac{1}{\sqrt{2}} & \frac{1}{\sqrt{2}} & \frac{1}{\sqrt{2}} \end{bmatrix} \tag{2.28}$$

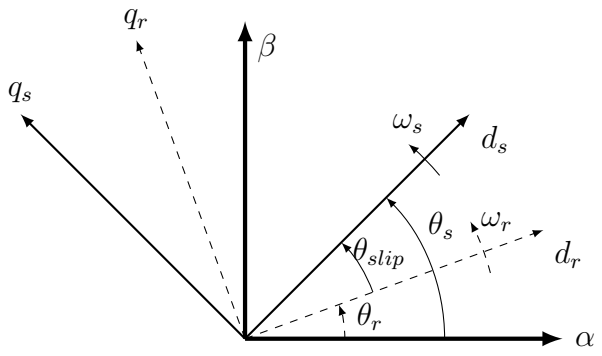

Figure 2.12: Reference frame schemes

and

$$\theta_{dq} = \int_0^t \omega_{dq} dt + \theta_{dq}(0). \tag{2.29}$$

In the above equations $\vec{f}$ is the vector notation of the machine parameters into the synchronous reference frame; θ_{dq} is the angle between the stationary reference frame and the arbitrary dq0-reference frame; ω_{dq} is the angular speed at which the arbitrary dq0-reference frame rotates; T_s is the transformation matrix from ABC reference frame to the arbitrary dq0-reference frame; and, $\theta_{dq}(0)$ is the initial value of the angle between the stationary reference frame and the arbitrary dq0-reference frame.

When the arbitrary dq0-reference frame is rotating at synchronous angular frequency, it yields

$$\omega_{dq} = \omega_s \tag{2.30}$$

and

$$\theta_{dq} = \theta_s, \tag{2.31}$$

where $\theta_s = \int_0^t \omega_s dt + \theta_s(0)$ is the angle between the stationary reference frame and the synchronous reference frame, as shown in Figure 2.12. Hence, the arbitrary dq0-reference frame rotating at synchronous angular speed is called the synchronous reference frame.

Expressing Equation (2.19) into synchronous dq0-reference frame using the transformation in Equation (2.28) yields

$$\begin{bmatrix} v_{sd} \\ v_{sq} \\ v_{s0} \end{bmatrix} = R_s \begin{bmatrix} i_{sd} \\ i_{sq} \\ i_{s0} \end{bmatrix} + \frac{d}{dt} \begin{bmatrix} \psi_{sd} \\ \psi_{sq} \\ \psi_{s0} \end{bmatrix} + \omega_s \begin{bmatrix} -\psi_{sq} \\ \psi_{sd} \\ 0 \end{bmatrix}, \tag{2.32}$$

where v_{sd} and v_{sq} are the d-axis and q-axis stator voltage; i_{sd} and i_{sq} are the d-axis and q-axis stator current; and, ψ_{sd} and ψ_{sq} are the d-axis and q-axis stator flux linkages.

On the rotor side, the transformation of rotor variables into the synchronous dq0-reference frame is given by

$$\boldsymbol{f_{rdq0}} = \boldsymbol{T_r f_{rabc}} \tag{2.33}$$

where

$$\boldsymbol{T_r} = \sqrt{\frac{2}{3}} \begin{bmatrix} \cos(\theta_r) & \cos(\theta_r - \frac{2\pi}{3}) & \cos(\theta_r + \frac{2\pi}{3}) \\ \sin(\theta_r) & \sin(\theta_r - \frac{2\pi}{3}) & \sin(\theta_r + \frac{2\pi}{3}) \\ \frac{1}{\sqrt{2}} & \frac{1}{\sqrt{2}} & \frac{1}{\sqrt{2}} \end{bmatrix} \tag{2.34}$$

and

$$\theta_{slip} = \int_0^t \omega_{slip} dt + \theta_{slip}(0). \tag{2.35}$$

In Equation (2.34), $\omega_{slip} = \omega_s - \omega_r$ is the relative angular speed between the rotating rotor frame and the synchronous dq0-reference frame; and, θ_{slip} denotes the relative angle between the synchronous reference frame and the rotating rotor reference frame.

The expression of the three-phase rotor voltage into the synchronous dq0-reference frame yields

$$\begin{bmatrix} v_{rd}^{'} \\ v_{rq}^{'} \\ v_{r0}^{'} \end{bmatrix} = R_r^{'} \begin{bmatrix} i_{rd}^{'} \\ i_{rq}^{'} \\ i_{r0}^{'} \end{bmatrix} + \frac{d}{dt} \begin{bmatrix} \psi_{rd}^{'} \\ \psi_{rq}^{'} \\ \psi_{r0}^{'} \end{bmatrix} + (\omega_s - \omega_r) \begin{bmatrix} -\psi_{rq}^{'} \\ \psi_{rd}^{'} \\ 0 \end{bmatrix}, \tag{2.36}$$

where $v_{rd}^{'}$ and $v_{rd}^{'}$ are the d-axis and q-axis rotor voltages reported to the stator windings; $i_{rd}^{'}$ and $i_{rq}^{'}$ are the d-axis and q-axis rotor currents reported to the stator windings; and, $\psi_{rd}^{'}$ and $\psi_{rq}^{'}$ are the d-axis and q-axis rotor flux linkages reported to the stator windings.

The three-phase stator and rotor flux linkages into the synchronous dq0-reference frame are given by

$$\begin{bmatrix} \boldsymbol{\psi_{sdq0}} \\ \boldsymbol{\psi_{rdq0}^{'}} \end{bmatrix} = \begin{bmatrix} \boldsymbol{T_s L_s (T_s)^{-1}} & \boldsymbol{T_s L_{sr}^{'} (T_r)^{-1}} \\ \boldsymbol{T_r (L_{sr}^{'})^T (T_s)^{-1}} & \boldsymbol{T_r L_r^{'} (T_r)^{-1}} \end{bmatrix} \begin{bmatrix} \boldsymbol{i_{sdq0}} \\ \boldsymbol{i_{rdq0}^{'}} \end{bmatrix}, \tag{2.37}$$

where

$$\boldsymbol{T_s L_s (T_s)^{-1}} = \begin{bmatrix} L_{sl} + L_m & 0 & 0 \\ 0 & L_{sl} + L_m & 0 \\ 0 & 0 & L_{sl} \end{bmatrix}, \tag{2.38}$$

$$\boldsymbol{T_r L_r^{'} (T_r)^{-1}} = \begin{bmatrix} L_{rl}^{'} + L_m & 0 & 0 \\ 0 & L_{rl}^{'} + L_m & 0 \\ 0 & 0 & L_{rl}^{'} \end{bmatrix}, \tag{2.39}$$

and

$$\boldsymbol{T_r (L_{sr}^{'})^T (T_s)^{-1}} = \boldsymbol{T_s L_{sr}^{'} (T_r)^{-1}} = \begin{bmatrix} L_m & 0 & 0 \\ 0 & L_m & 0 \\ 0 & 0 & 0 \end{bmatrix}. \tag{2.40}$$

In Equation (2.38)−(2.40), L_{sl} and $L_m = \frac{3}{2} L_{sm}$ denote the leakage inductance and the magnetising inductance; and, $L_{rl}^{'}$ is the leakage inductance referred to the stator windings.

Substituting Equations (2.39), (2.38) and (2.40) into Equations (2.37), the expressions of the stator and rotor flux linkages becomes

$$\psi_{sd} = L_{sl} i_{sd} + L_m (i_{sd} + i_{rd}^{'}) \tag{2.41}$$

$$\psi_{sq} = L_{sl} i_{sq} + L_m (i_{sq} + i_{rq}^{'}) \tag{2.42}$$

$$\psi_{s0} = L_{sl} i_{s0} \tag{2.43}$$

$$\psi_{rd}^{'} = L_{rl}^{'} i_{rd}^{'} + L_m (i_{sd} + i_{rd}^{'}) \tag{2.44}$$

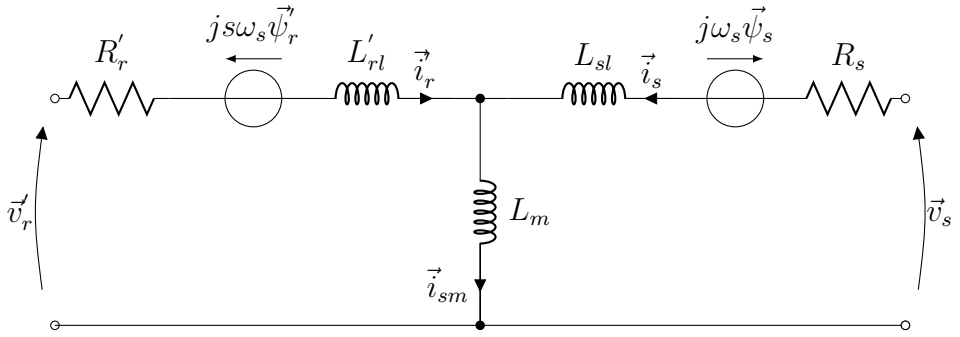

Figure 2.13: DFIG Equivalent Circuit in dq0-reference Frame

$$\psi_{rq}' = L_{rl}' i_{rq}' + L_m(i_{sq} + i_{rq}') \tag{2.45}$$

$$\psi_{r0}' = L_{rl}' i_{r0}. \tag{2.46}$$

The equivalent circuit of the DFIG resulting from the voltage and flux linkage expressions is depicted in Figure 2.13.

Equation (2.32) and Equation (2.36) can be rewritten by replacing the operator $\frac{d}{dt}$ with the Laplace operator p. Hence, the stator voltage space vector and the rotor voltage space vector become

$$v_{sd} = R_s i_{sd} + p\psi_{sd} - \omega_s \psi_{sd} \tag{2.47}$$

$$v_{sq} = R_s i_{sq} + p\psi_{sq} + \omega_s \psi_{sq} \tag{2.48}$$

$$v_{s0} = R_s i_{s0} + p\psi_{s0} \tag{2.49}$$

$$v_{rd}' = R_r' i_{rd}' + p\psi_{rd}' - (\omega_s - \omega_r)\psi_{rd}' \tag{2.50}$$

$$v_{rq}' = R_r' i_{rq}' + p\psi_{rq}' + (\omega_s - \omega_r)\psi_{rq}' \tag{2.51}$$

$$v_{r0}' = R_r' i_{r0}' + p\psi_{r0}'. \tag{2.52}$$

The stator active and reactive powers of the DFIG are given by

$$P_s = \Re\left(\left(\tfrac{3}{2}\right)\vec{v}_s\bar{\vec{i}}_s\right) = \frac{3}{2}(v_{sd}i_{sd} + v_{sq}i_{sq}) \tag{2.53}$$

and

$$Q_s = \Im\left(\left(\tfrac{3}{2}\right)\vec{v}_s\bar{\vec{i}}_s\right) = \frac{3}{2}(v_{sq}i_{sd} - v_{sd}i_{sq}), \tag{2.54}$$

where P_s is the stator active power; Q_s is the stator reactive power; and, $\bar{\vec{i}}_s$ is the conjugate of the stator current space vector.

In the rotor side, the rotor active and reactive powers are given by

$$P_r = \Re\left(\left(\tfrac{3}{2}\right)\vec{v}_r'\bar{\vec{i}}_r'\right) = \frac{3}{2}(v_{rd}'i_{rd}' + v_{rq}'i_{rq}') \tag{2.55}$$

and

$$Q_r = \Im\left(\left(\tfrac{3}{2}\right)\vec{v}_r'\bar{\vec{i}}_r'\right) = \frac{3}{2}(v_{rq}'i_{rd}' - v_{rd}'i_{rq}'), \tag{2.56}$$

where P_r is the rotor active power; Q_r is the rotor reactive; and, $\overline{\vec{i}}_r$ is the conjugate of the rotor current space vector.

The electromagnetic torque can be given by

$$\tau_{em} = \left(\frac{3}{2}\right)\left(\frac{P}{2}\right)(\psi_{sd}i_{sq} - \psi_{sq}i_{sd}) \tag{2.57}$$

or

$$\tau_{em} = \left(\frac{3}{2}\right)\left(\frac{P}{2}\right)(\psi'_{rd}i'_{rq} - \psi'_{rq}i'_{rd}), \tag{2.58}$$

where τ_{em} is the electromagnetic torque and P is the number of poles of the machine.

2.6.3 Mechanical Equation

The relationship between the electromagnetic torque and the mechanical torque can be expressed by

$$J\frac{d\Omega_m}{dt} + B\Omega_m = \tau_m - \tau_{em}, \tag{2.59}$$

where J is the inertia; Ω_m is the shaft angular speed; τ_m is the mechanical torque of the machine; and τ_{em} is the electromagnetic torque.

2.6.4 Simulink Implementation of The DFIG Model

The expressions of stator and rotor currents of the DFIG into the synchronous dq0-reference frame are obtained by rewriting Equation (2.41)−(2.46) as follows;

$$i_{sd} = \frac{1}{L_{sl}}(\psi_{sd} - \psi_{md}) \tag{2.60}$$

$$i_{sq} = \frac{1}{L_{sl}}(\psi_{sq} - \psi_{mq}) \tag{2.61}$$

$$i_{s0} = \frac{1}{L_{sl}}\psi_{s0} \tag{2.62}$$

$$i'_{rd} = \frac{1}{L'_{rl}}(\psi'_{rd} - \psi_{md}) \tag{2.63}$$

$$i'_{rq} = \frac{1}{L'_{rl}}(\psi'_{rq} - \psi_{mq}) \tag{2.64}$$

$$i'_{r0} = \frac{1}{L'_{rl}}\psi'_{r0}, \tag{2.65}$$

where

$$\psi_{md} = \frac{1}{\frac{1}{L_m} + \frac{1}{L'_{rl}} + \frac{1}{L_{sl}}}\left(\frac{\psi_{sd}}{L_{sl}} - \frac{\psi'_{rd}}{L'_{rl}}\right) \tag{2.66}$$

and

$$\psi_{mq} = \frac{1}{\frac{1}{L_m} + \frac{1}{L'_{rl}} + \frac{1}{L_{sl}}} \left(\frac{\psi_{sq}}{L_{sl}} - \frac{\psi'_{rq}}{L'_{rl}} \right). \tag{2.67}$$

By substituting Equation (2.60)−(2.65) into Equation (2.47)−(2.52) and re-arranging these expressions, yields

$$p\psi_{sd} = v_{sd} - \omega_s \psi_{sq} + \frac{R_s}{L_{sl}}(\psi_{md} - \psi_{sd}) \tag{2.68}$$

$$p\psi_{sq} = v_{sq} + \omega_s \psi_{sd} + \frac{R_s}{L_{sl}}(\psi_{mq} - \psi_{sq}) \tag{2.69}$$

$$p\psi_{s0} = v_{s0} + \frac{R_s}{L_{sl}}\psi_{s0} \tag{2.70}$$

$$p\psi'_{rd} = v'_{rd} - (\omega_s - \omega_r)\psi'_{rq} + \frac{R'_r}{L'_{rl}}(\psi_{md} - \psi'_{rd}) \tag{2.71}$$

$$p\psi'_{rq} = v'_{rq} - (\omega_s - \omega_r)\psi'_{rd} + \frac{R'_r}{L'_{rl}}(\psi_{mq} - \psi'_{rq}) \tag{2.72}$$

$$p\psi'_{r0} = v'_{r0} + \frac{R_r}{L'_{rl}}\psi'_{r0}. \tag{2.73}$$

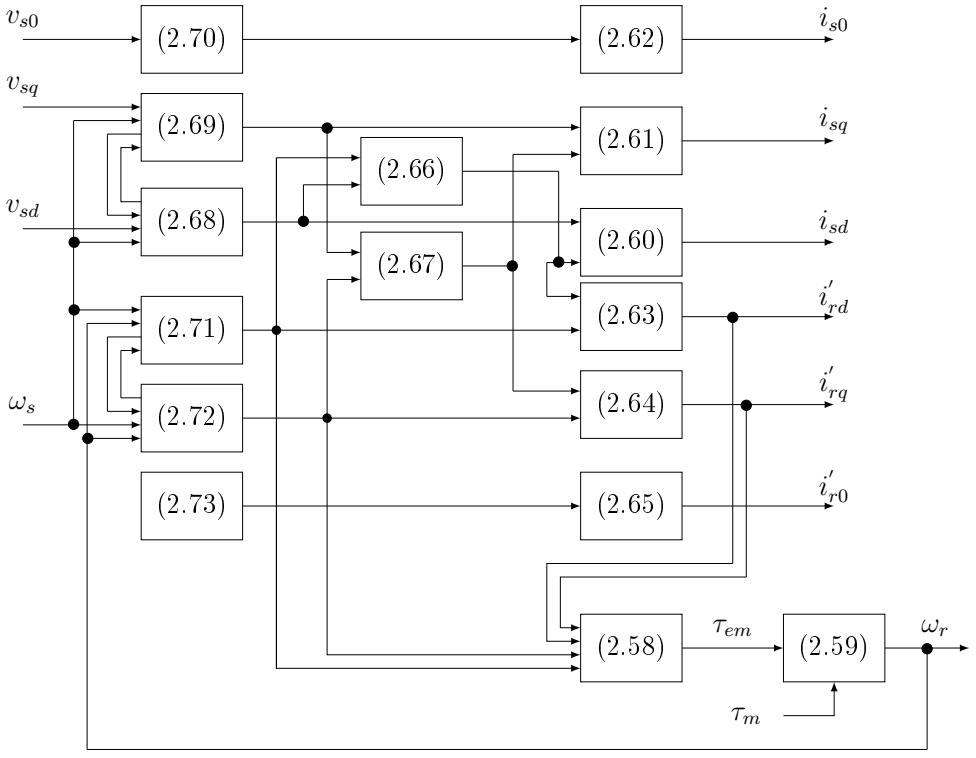

Figure 2.14: Induction machine implementation

From the current expressions displayed in Equations (2.60)−(2.65), the flux linkage expressions depicted in Equations (2.68)−(2.73), (2.66) and (2.67), and the mechanical shaft speed given in Equation (2.59) together with the torque expression displayed in Equation (2.58), a MATLAB/SIMULINK model of the DFIG is built, as depicted in Figure 2.14.

2.6.4.1 Free Acceleration Characteristics

The free acceleration characterisitics observed in this simulation were conducted in MATLAB/SIMULINK, are that of a 3 hp, 4 pole, 60 Hz, 3 phase induction motor. The machine parameters of that induction machine are taken from [35]. The machine parameters are displayed in Table B.5. The DFIG model presented in Section 2.6.4 is used for the simulation of the induction motor, since short-circuiting the rotor of this DFIG model leads to a normal induction machine. Hence, the simulation is conducted with the rotor voltages being equal to zero.

The three-phase stator and rotor current characteristics during free acceleration is illustrated in Figure 2.15. The torque and speed characteristics during free acceleration are displayed in Figure 2.16. These figures are obtained from applying a rated three-phase stator voltage to the stator windings of the induction motor initially stalled. The mechanical shaft speed increases until it reaches the synchronous speed of 1800 rpm, as shown in Figure 2.16(b) due to the fact that losses (friction and windage losses) are not taken into consideration. At stall, the impedance of the induction machine is composed only of the the stator resistance and stator leakage reactance in series with the rotor resistance and rotor leakage reactance, which implies that the starting current is almost ten times higher than their rated values as displayed in Figure 2.15. Besides, the applied stator voltage is at its at rated value as well.

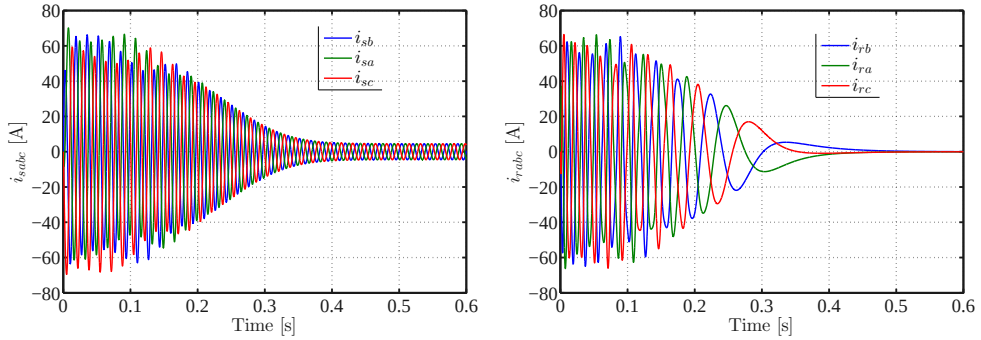

(a) (b)

Figure 2.15: Free Acceleration test: (a) three-phase stator current ; (b) three-phase rotor current

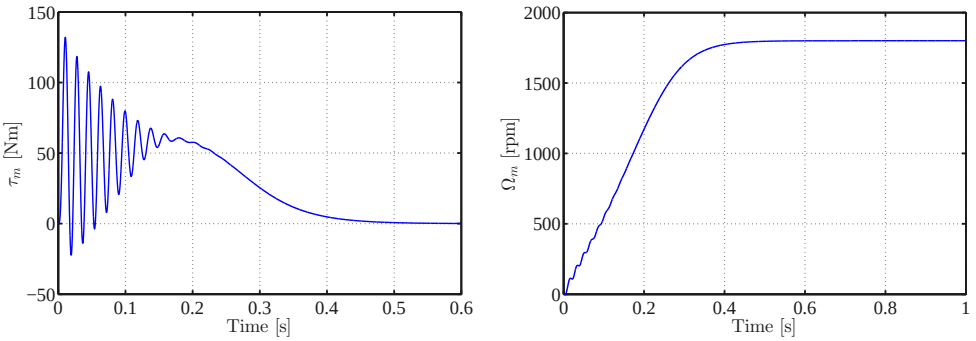

(a) (b)

Figure 2.16: Free acceleration test: (a) electromagnetic torque ; (b) rotor angular shaft speed

Another noticeable pattern is that the envelope of the machine currents varies only during the transient period, as displayed in Figure 2.15. The starting torque is also quite high, as shown in Figure 2.16(a). The starting torque is at about ten times the rated torque and the electromagnetic torque decays with time as shown in Figure 2.16(a). Also, from Figure 2.16(a), it can be seen that the electromagnetic torque at the starting of the induction machine varies at a frequency of about 60 Hz between a relatively positive range of values.

2.7 Back-to-back converter Modelling

Assume that the grid-side converter (GSC) of the back-to-back converter of the DFIG system consists of a three-phase two-level voltage-source converter (VSC), as depicted in Figure 2.17. It can be seen that the VSC is composed of six power switches. Each power switch is composed of two semi-conductors connected as depicted in Figure 2.18. Generally, a free-wheeling diode is used for the protection of the main semi-conductor (IGBTs, GTOs, MOSFETs,...). In addition, each phase leg is composed of two power switches. In order to

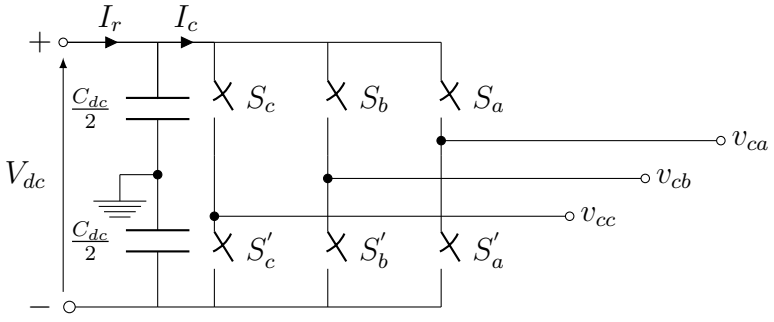

Figure 2.17: Schematic of the power switches of a VSC

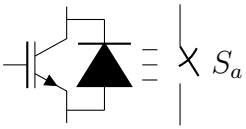

Figure 2.18: Power switch composition

avoid short-circuiting the DC link at the same leg, when the upper power switch is closed (ON or 1), the lower power switch should be open (OFF or 0). Hence, the switching state of the upper power switch and lower switch of the same leg are complementary with dead time included.

From Figure 2.17, the instantaneous three-phase leg voltage are given by

$$v_{ac} = v_{an}(t) + v_{nN}(t), \tag{2.74}$$

$$v_{bc} = v_{bn}(t) + v_{nN}(t) \tag{2.75}$$

and

$$v_{cc} = v_{cn}(t) + v_{nN}(t). \tag{2.76}$$

In Equations (2.74)−(2.76), $v_{ac}(t)$, $v_{bc}(t)$ and $v_{cc}(t)$ are the instantaneous phase A, B and C leg voltages of the VSC, respectively; $v_{an}(t)$, $v_{bn}(t)$ and $v_{cn}(t)$ are the phase A,B,C to neutral voltages, respectively; and v_{nN} is the common mode voltage. Assume that the VSC is connected to a symmetrical three-phase resistive load yields

$$v_{an}(t) + v_{bn}(t) + v_{cn}(t) = 0. \tag{2.77}$$

By summing Equation (2.74) − (2.76), the voltage between the negative point of the DC-link bus and the neutral is given by

$$v_{nN} = \frac{1}{3}(v_{ac}(t) + v_{bc}(t) + v_{cc}(t)). \tag{2.78}$$

Substituting Equation (2.78) into Equation (2.74) − (2.76), the instantaneous line-to-neutral voltage yields

$$v_{an} = \frac{2}{3}v_{ac}(t) - \frac{1}{3}(v_{bc}(t) + v_{cc}(t)), \tag{2.79}$$

$$v_{bn} = \frac{2}{3}v_{bc}(t) - \frac{1}{3}(v_{ac}(t) + v_{cc}(t)) \tag{2.80}$$

and

$$v_{cn} = \frac{2}{3}v_{cc}(t) - \frac{1}{3}(v_{ac}(t) + v_{bc}(t)). \tag{2.81}$$

The dynamic behavior of the DC-link voltage is given by

$$\frac{dV_{dc}}{dt} = I_r - I_c, \tag{2.82}$$

where V_{dc} is the DC-link voltage; I_r is the DC current coming from the rotor-side converter; and I_c is the current heading to the grid-side converter.

The value of the converter voltage is obtained using the Equations (2.79) – (2.81), knowing that the leg voltages are given by

$$v_{ac} = S_a \frac{V_{dc}}{2}, \tag{2.83}$$

$$v_{bc} = S_b \frac{V_{dc}}{2} \tag{2.84}$$

and

$$v_{cc} = S_c \frac{V_{dc}}{2}. \tag{2.85}$$

In Equations (2.83)–(2.85), S_a, S_b and S_c are the switching function of the upper power switches. It is important to notice that when S_a is ON, $S_a = 1$ and when $S_a = 0$ is OFF. The eight switching states and different values of the line-to-neutral converter voltage are displayed in Table 2.3. It can be seen from Table 2.3 that the maximum amplitude of the line- to-neutral reference voltage is $\frac{2V_{dc}}{3}$.

On the other hand, the vector representation of the instantaneous reference three-phase converter voltage is given by

$$\vec{v}_{ref} = \frac{2}{3}\left(v_{an}(t)e^{j0} + v_{bn}(t)e^{\left(j\frac{2\pi}{3}\right)} + v_{cn}(t)e^{\left(j\frac{4\pi}{3}\right)}\right) = v_\alpha + jv_\beta. \tag{2.86}$$

It is worth noticing that the reference voltage space vector rotates at line angular frequency on the hexagonal plan, shown in Figure 3.8. Equating the real part and the imaginary part in Equation (2.86) yields

$$v_\alpha = \frac{2}{3}\left(v_{an}(t) + v_{bn}(t)\cos\left(\frac{2\pi}{3}\right) + v_{cn}(t)\cos\left(\frac{2\pi}{3}\right)\right) \tag{2.87}$$

and

$$v_\beta = \frac{2}{3}\left(v_{bn}(t)\sin\left(\frac{2\pi}{3}\right) - v_{cn}(t)\sin\left(\frac{2\pi}{3}\right)\right). \tag{2.88}$$

Table 2.3: Switching states

Switching gates	S_a	S_b	S_c	$v_{an}(t)$	$v_{an}(t)$	$v_{an}(t)$	$v_{ab}(t)$	$v_{bc}(t)$	$v_{ca}(t)$
K_0	0	0	0	0	0	0	0	0	0
K_1	1	0	0	$\frac{2V_{dc}}{3}$	$\frac{-V_{dc}}{3}$	$\frac{-V_{dc}}{3}$	V_{dc}	0	$-V_{dc}$
K_2	1	1	0	$\frac{V_{dc}}{3}$	$\frac{V_{dc}}{3}$	$\frac{-2V_{dc}}{3}$	0	V_{dc}	$-V_{dc}$
K_3	0	1	0	$\frac{-V_{dc}}{3}$	$\frac{2V_{dc}}{3}$	$\frac{-V_{dc}}{3}$	$-V_{dc}$	$-V_{dc}$	0
K_4	0	1	1	$\frac{-2V_{dc}}{3}$	$\frac{V_{dc}}{3}$	$\frac{V_{dc}}{3}$	$-V_{dc}$	0	V_{dc}
K_5	0	0	1	$\frac{-V_{dc}}{3}$	$\frac{-V_{dc}}{3}$	$\frac{2V_{dc}}{3}$	0	$-V_{dc}$	V_{dc}
K_6	1	0	1	$\frac{V_{dc}}{3}$	$\frac{-2V_{dc}}{3}$	$\frac{V_{dc}}{3}$	V_{dc}	$-V_{dc}$	0
K_7	1	1	1	0	0	0	0	0	0

Table 2.4: Reference voltage space vectors with switching states

Space vector	Switching state	Space vector value
$\vec{v}_0$	[000]	$\vec{v}_0 = 0$
$\vec{v}_1$	[100]	$\vec{v}_1 = \frac{2}{3}V_{dc}e^{j0}$
$\vec{v}_2$	[110]	$\vec{v}_2 = \frac{2}{3}V_{dc}e^{j\frac{\pi}{3}}$
$\vec{v}_3$	[010]	$\vec{v}_3 = \frac{2}{3}V_{dc}e^{j\frac{2\pi}{3}}$
$\vec{v}_4$	[011]	$\vec{v}_4 = \frac{2}{3}V_{dc}e^{j\frac{3\pi}{3}}$
$\vec{v}_5$	[001]	$\vec{v}_5 = \frac{2}{3}V_{dc}e^{j\frac{4\pi}{3}}$
$\vec{v}_6$	[101]	$\vec{v}_6 = \frac{2}{3}V_{dc}e^{j\frac{5\pi}{3}}$
$\vec{v}_7$	[111]	$\vec{v}_7 = 0$

In Equation (2.87) and Equation (2.88), v_α and v_β are the real and imaginary parts of the reference voltage space vector. From Table 2.4, it can be seen that the reference converter voltage space vector varies at a rate of sixty degree. It is worth noticing that the reference voltage space vector comes from the control algorithm. The schematic of the RSC is depicted in Figure 2.19. The modelling of the RSC is similar to that of the GSC.

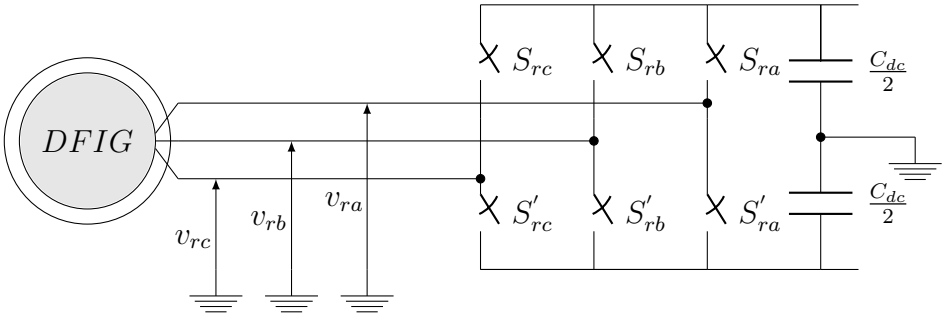

Figure 2.19: Machine Side Converter Scheme

2.8 Passive Filter models

The reason for using a filter is to attenuate the harmonics produced by the back-to-back converter. In this subsection two types of filters are modelled, the LCL filter and the L filter. In addition the LCL design procedure is also discussed.

2.8.1 LCL Filter

The per-phase LCL filter configuration is depicted in Figure 2.20. The mathematical model of the wye-connected LCL filter is given by

$$C_f \frac{d\vec{v}_f}{dt} = \vec{i}_g - \vec{i}_c - j\omega_s C_f \vec{v}_f, \tag{2.89}$$

$$L_g \frac{d\vec{i}_g}{dt} = \vec{v}_g - \vec{v}_f - (R_g + j\omega_s L_g)\vec{i}_g \tag{2.90}$$

and

$$L_c \frac{d\vec{i}_c}{dt} = \vec{v}_f - \vec{v}_c - (R_c + j\omega_s L_c)\vec{i}_c. \tag{2.91}$$

In Equations (2.89)−(2.91), $\vec{v}_f$ is the filter capacitor voltage space vector; $\vec{v}_g$ is the grid voltage space vector; $\vec{v}_c$ denotes the converter voltage space vector; $\vec{i}_g$ is the grid current space vector and $\vec{i}_c$ is the converter current space vector; L_c, L_g and C_f are the converter inductance, the grid inductance and the capacitor filter of the LCL filter, respectively; and, ω_s, R_c and R_g are the synchronous angular speed, the converter resistance and the grid resistance, respectively. The Laplace operator can be expressed in terms of frequency as follows;

$$p = j\omega, \tag{2.92}$$

where $p = j\omega$ represents a harmonic angular frequency. From Equation (2.89), Equation (2.90) and Equation (2.91) together with the assumption that only the converter voltage is the harmonics source (i.e the grid voltage is being considered short-circuited), the transfer function of the LCL filter is deduced. The LCL filter scheme at high harmonic components is depicted in Figure 2.21. Neglecting the damping resistance in the LCL filter, the transfer function of the LCL filter is given by

$$H_{lcl}(p) = \frac{i_g}{v_c} = \frac{1}{L_c L_g C_f p^3 + (L_c + L_g)p}, \tag{2.93}$$

where $H_{lcl}(p)$ is the transfer function of the undamped LCL filter.

On the other hand, when the damping resistance is taken into consideration, the damped LCL filter transfer function is given by

$$H_{dlcl}(p) = \frac{i_g}{v_c} = \frac{C_f R_d p + 1}{L_c L_g C_f p^3 + C_f (L_c + L_g) R_d p^2 + (L_c + L_g)p}, \tag{2.94}$$

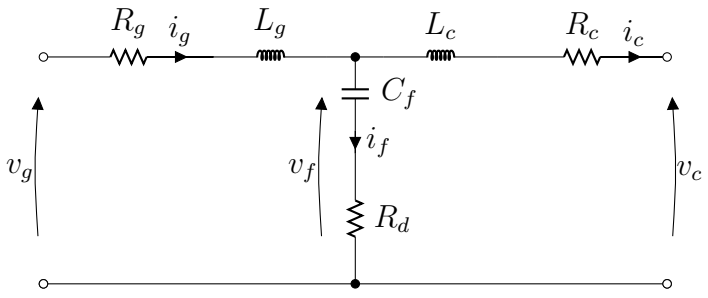

Figure 2.20: Per-phase LCL filter scheme

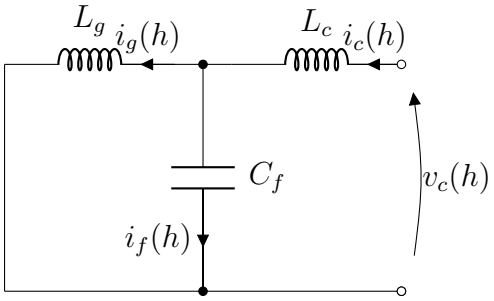

Figure 2.21: Per-phase LCL filter at harmonic frequency

where $H_{dlcl}(p)$ is the transfer function of the damped LCL filter. The harmonic attenuation of the LCL filter without damping is given by

$$\left|\frac{i_g(h)}{v_c(h)}\right| = \frac{1}{\omega_h L_c L_g C_f |\omega_{res}^2 - \omega_h^2|}, \tag{2.95}$$

$$\left|\frac{i_c(h)}{v_c(h)}\right| \approx \frac{1}{\omega_h L_c} \tag{2.96}$$

and

$$\left|\frac{i_g(h)}{i_c(h)}\right| \approx \frac{1}{L_g C_f |\omega_{res}^2 - \omega_h^2|}. \tag{2.97}$$

In Equation (2.95)−(2.97), $\omega_{res}^2 = \frac{L_c + L_g}{L_c L_g C_f}$ is the angular resonant speed; Subscript h denotes the harmonic order; and, $\omega_h = 2\pi f_h$ is the angular frequency at harmonic frequency h. Those LCL filter attenuation is effective when the LCL filter is properly damped [27].

2.8.2 L Filter

The per-phase scheme of the L filter is shown in Figure 2.22, where R_T and L_T denote the filter resistance and the filter inductance, respectively; and, v_g and v_c are the grid and converter voltages respectively. At first glance, from Figure 2.22, it can be seen that, in contrast to the LCL filter, the three-phase converter current is the same as the three-phase grid current.

The mathematical model of the single-phase L filter is given by

$$v_g = R_T \vec{i}_g + L_T \frac{d\vec{i}_c}{dt} + \vec{v}_c. \tag{2.98}$$

The transfer function is deduced from Equation (2.98), assuming that only the converter is the source of harmonics components in the system, as shown in Figure 2.23. This yields

$$H_l(p) = \frac{i_c}{v_c} = \frac{1}{L_T p + R_T}, \tag{2.99}$$

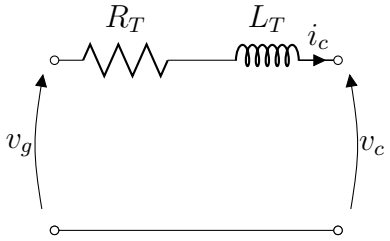

Figure 2.22: Per-phase L filter scheme

where $H_l(p)$ is the transfer function of the L filter.

Substituting Equation (2.92) into Equation (2.99) and assuming a higher frequency $L_T^2\omega_h^2 >> R_T^2$, the filter attenuation is given by

$$|H_l(j\omega_h)| \approx \frac{1}{\sqrt{L_T^2\omega_h^2}}, \tag{2.100}$$

where $|H_l(j\omega_h)|$ denotes the L filter attenuation; and, ω_h is the angular speed of at harmonic frequency.

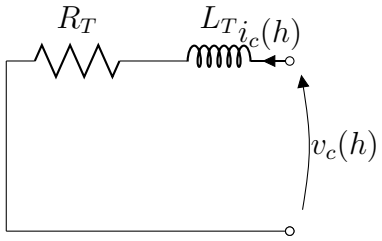

Figure 2.23: Per-phase L filter scheme at harmonic frequency

2.9 Conclusion

An overview of different configurations of wind turbine systems and the modelling of the whole DFIG system in wind turbine applications were presented. A DFIG model was built in MATLAB/SIMULINK and the performance of that model during free acceleration is satisfactory.

Chapter 3

Grid/Load Side Converter Control

In this chapter, the implementation of the phase locked loop and that of the space vector pulse width modulation are discussed. Moreover, a design procedure of the LCL filter is given and a control algorithm of the grid/load side converter is proposed. Also, the design of the PI controller parameters is also presented. Further, a comparative study of the L filter and the LCL filter is conducted from an effectiveness point of view and the simulation of the grid-connected grid-side converter is presented. Since the control of the grid-side converter and that of the load-side converter in DFIG system are both similar, only the grid-side converter is treated in this chapter.

3.1 GSC Configuration

The grid-side converter (GSC) of DFIG systems can be seen as a three-phase grid-connected voltage-source converter (VSC). The per-phase schematic of the GSC and its control system are depicted in Figure 3.1. The grid-side

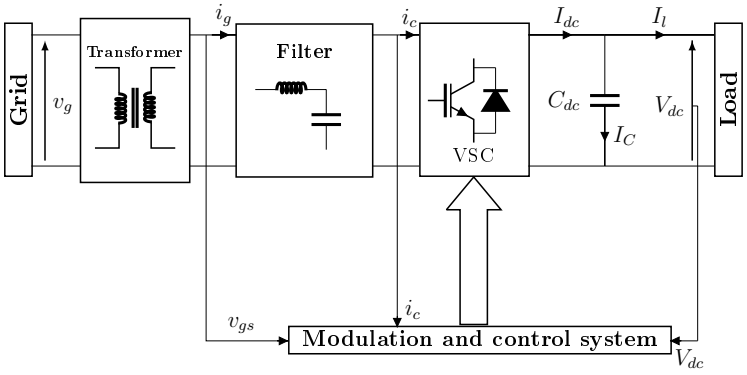

Figure 3.1: Schematic of the per-phase grid-connected VSC

converter is composed of the AC side, the DC side and the control system. The AC side consists of the grid, the transformer, the filter as well as the voltage-source converter. The filter enhances the power quality of the GSC by mitigating high harmonic frequencies generated by the switching elements of the VSC. Hence, the design of the LCL filter is discussed in the following section. On the other hand, the DC side is composed of a DC-link capacitor and the load. In this thesis, the grid voltage is assumed purely sinusoidal and without internal impedance.

The control system of the GSC is composed of several modules such as the PI controllers, the phase locked loop and the SV-PWM function and the variable transformation functions (Clark transformation, Park transformation, inverse Clark transformation). All These functions are discussed in the following sections.

3.2 LCL Filter Design Procedure

The algorithm of the LCL filter design is depicted in Figure 3.2. The conventional LCL filter design procedure used in this thesis is similar to the LCL design procedure that is discussed in [27, 42]. In the above-mentioned LCL filter design procedure, the line frequency, the power rating of the converter and the switching frequency are used as inputs. This approach consists of five steps that enable the proper design of the LCL filter parameters. This approach is very dependent on the rated values of the system.

1. Select the current ripple on the converter side in order to design the converter inductance (L_c), then the value of the converter inductance is calculated using an index κ for their relationship. The total inductance $L_T = L_c + L_g$ should be lower than or equal to 0.1 per-unit (pu) in order to reduce the losses in the system. The expressions of the converter inductance and the grid inductance are given by [43]

$$L_c = \frac{V_{dc}}{24 f_{sw} \Delta i_m}, \tag{3.1}$$

and

$$L_g = \kappa L_c. \tag{3.2}$$

In Equation (3.1) and Equation (3.2), Δi_m is the current ripple; L_c and L_g are the converter and grid inductance, respectively; and, κ is the index of the relation between the grid inductance and the converter inductance. The grid inductance L_g is found using the Equation (3.2).

2. Choose the reactive power to be consumed at rated conditions. Then, determine the filter capacitor value by selecting k as a percentage of the

consumed rated reactive power in the system. Hence, the LCL filter capacitor is given by

$$C_f = kC_b, \tag{3.3}$$

where C_f is the filter capacitor and C_b is the base capacitor of the system. This value of k should not exceed 5% of the rated reactive power.

3. Select the desired current ripple attenuation by using the the expression below ;

$$\frac{i_g(h_{sw})}{i_c(h_{sw})} = \frac{1}{|1 + \kappa(1 - x.k)|}. \tag{3.4}$$

In Equation (3.4), $h_{sw} = \frac{\omega_{sw}}{\omega_n}$ indicates the harmonic order of switching frequency of the electrical variable; ω_{sw} is the angular speed at switching frequency; ω_b is the angular speed of the system; $i_g(h_{sw})$ is the the grid

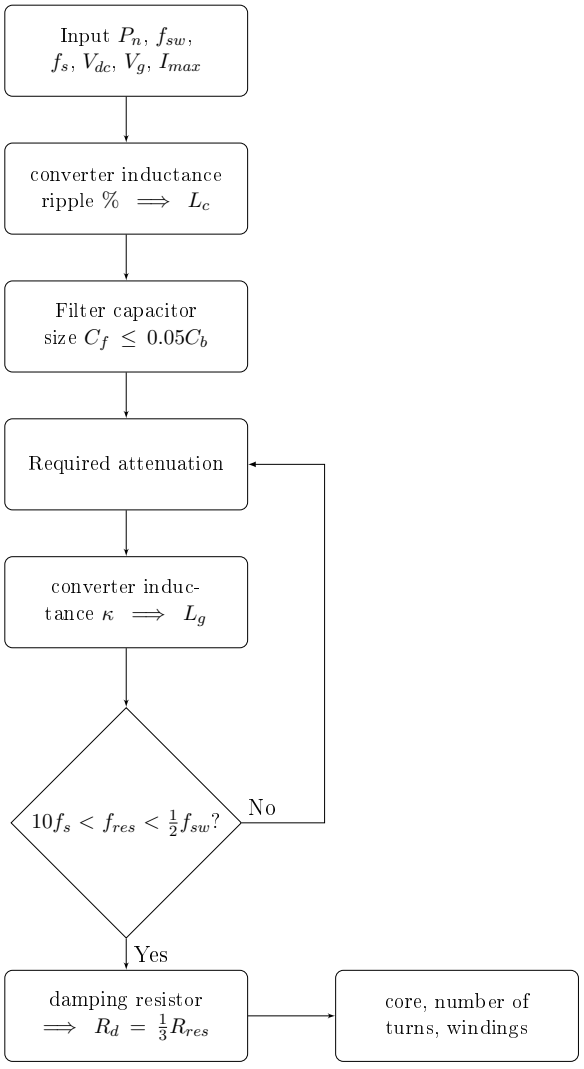

Figure 3.2: Algorithm of the LCL filter design

current harmonic at switching frequency; $i_c(h_{sw})$ is the converter current at switching frequency; and, $x = L_c C_b \omega_{sw}^2$ is a constant.

4. Verify the resonant frequency by using the expression below;

$$f_{res} = \frac{1}{2\pi}\sqrt{\frac{L_c + L_g}{L_c L_g C_f}}. \tag{3.5}$$

In Equation (3.5), f_{res} is the resonant frequency of the filter. It is advised that the resonant frequency should range from ten-times the line frequency to half of the switching frequency [27, 42]. If this condition is not fulfilled then return to step 2) or 3) to change the value of either the filter capacitor or the value of the harmonic attenuation.

5. Select the passive damping so that the efficiency remains within acceptable range. The value of the damping resistor is limited since it can cause losses that affect the efficiency of the system. It is advised that this value should be one-third of the capacitor impedance at resonance frequency [27]. The damping resistor (R_d) is given by

$$R_d = \frac{1}{3}R_{res} = \frac{1}{6\pi f_{res} C_f}, \tag{3.6}$$

where R_{res} is the capacitor filter impedance at resonant frequency.

3.2.1 LCL Filter Design Example

The parameters of the inverter to be used in the laboratory are displayed in Table 3.1. Besides the information about the per-unit system to be used in the LCL filter design, an example is displayed in Table 3.2. Given these parameters a design example is conducted as follows;

1. Choose a current ripple which is 13.5 % of the maximum current of the system, the converter inductance is determined using Equation (3.1), then the $L_c = 4$ mH .

Table 3.1: VSI parameters to be used in the Lab

Parameters	Values
Power	8.7 kV A
Line-to-line voltage	380 V
Current	12 A
Switching frequency	2.5 kHz
Frequency	50 Hz

Table 3.2: VSI per-unit system

Base parameter	value
Base power	8.7 kV A
Base voltage	310.26 V
Base current	18.69 A
Base impedance	16.596 Ω
Base inductance	52.8 mH
Base capacitor	191.799 μF
Base frequency	50 Hz

2. Choose a filter capacitor that is $C_f = 9.6\ \mu$F with regards to the constraint that the filter capacitor should be less or equal to 5 % of the rated capacitor of the system.

3. Choose the filter current attenuation to be 18.66 % in Equation (3.4) lead to a value of $\kappa = 0.75$. Using the relationship between the grid and converter inductances displayed in Equation (3.2), the grid inductance value is $L_g = 3$ mH. Notice that by choosing this current attenuation the total inductance of the filter $L_T \approx 0.132$ pu which is beyond the limit of proposed total inductance which should be less or equal to 0.1 pu due to the losses in the system. However, the design of the filter is a trade-off between the power losses and the harmonics level in the system. Furthermore, the choice of the switching frequency is a trade-off between harmonics and the burden computation of the computer in the laboratory.

4. Verifying the resonant frequency obtained using Equation (3.5) yields the resonant frequency $f_{res} = 1.24013$ kHz which is well within the range.

5. The the value of the damping resistor is chosen to be 5 Ω .

The resistance values of the grid inductance and converter are $R_c = R_g = 0.1\ \Omega$ since it is suggested in [44] that the Joule losses to be set to a value under 1 % of the rated power. From the design above, the LCL filter parameters depicted in Table 3.3 are obtained. The bode plot of the LCL filter without a damping

Table 3.3: LCL parameters

Filter parameter	values
L_c	4 mH
L_g	3 mH
C_f	9.6 μF
R_d	5 Ω
$R_T = R_c + R_g$	0.2 Ω

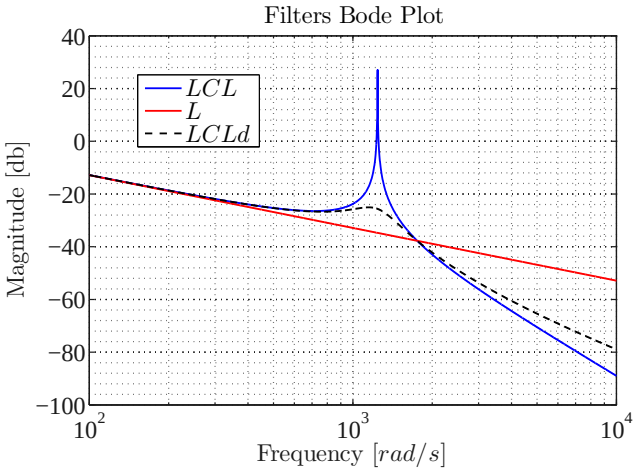

Figure 3.3: Filter bode plots

resistor, the L filter and the damped LCL filter are depicted in Figure 3.3 and were obtained using the parameters displayed in Table 3.3. The L filter in Figure 3.3, is obtained by summing the grid and converter inductances. It can be seen that there is an attenuation of the resonance peak when applying the damping resistor. Moreover, at the lower frequencies the LCL filter behaviour is similar to that of the L filter, as shown in Figure 3.3.

3.3 Phase Locked Loop Implementation

The phase locked loop (PLL) provides the grid voltage angle necessary when using the concept of vector alignment along a chosen reference frame axis. The phase locked loop is largely discussed in [45]. Assume that the grid voltage space vector is expressed by

$$\vec{v}_g = V_m e^{j\theta_g}, \tag{3.7}$$

where $\vec{v}_g$ is the grid voltage space vector; θ_g is the angle of the grid voltage; and, V_m is the maximum amplitude of the phase to neutral grid voltage. From Figure 3.4, the grid voltage vector can be represented in the synchronous dq0-

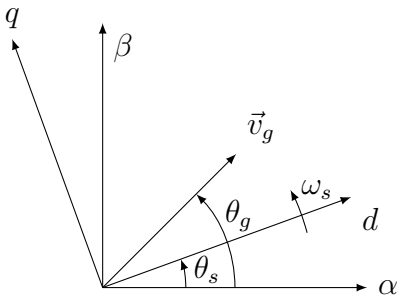

Figure 3.4: Grid voltage Representation

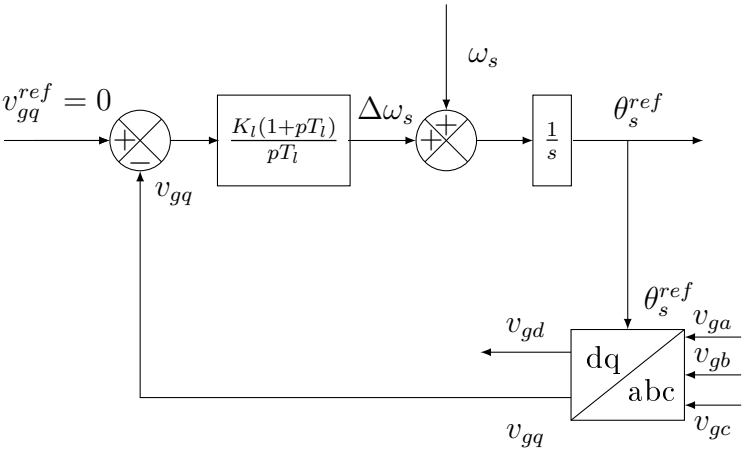

Figure 3.5: PLL control loop

reference frame using the expressions below;

$$\begin{bmatrix} v_{gd} \\ v_{gq} \end{bmatrix} = \begin{bmatrix} V_m \cos(\theta_g - \theta_s) \\ V_m \sin(\theta_g - \theta_s) \end{bmatrix}. \tag{3.8}$$

In Equation (3.8), v_{gd} and v_{gd} are the d-axis and q-axis grid voltage; and, θ_s is the angle of the synchronous dq0-reference frame; and, θ_g is the angle of the grid voltage space vector.

At small signal with the approximation of the sine and cosine in Equation (3.8)

$$\begin{bmatrix} \delta v_{gd} \\ \delta v_{gq} \end{bmatrix} \approx \begin{bmatrix} V_m(1 - \frac{\delta\theta^2}{2}) \\ V_m(\delta\theta) \end{bmatrix}, \tag{3.9}$$

is obtained, where $\delta\theta = \theta_g - \theta_s$ is a small variation of the angle between the grid voltage and the synchronous dq0-reference frame. From Equation (3.9), it can be seen that δv_{gq} is equal to zero when the grid voltage angle and the reference frame angle are equal $\theta_g = \theta_s$. Then, the synchronous dq0-reference frame is said to be aligned along the d-axis of the synchronous dq0-reference frame.

When accounting a sample delay, the plant of the PLL is given by

$$H_{plant}(p) = \Big(\frac{1}{1 + pT_s}\Big)\Big(\frac{V_m}{p}\Big), \tag{3.10}$$

The closed loop of the PLL is depicted in Figure 3.5. From Figure 3.5, the open loop transfer function of the PLL control loop is given by

$$H_{ol}(p) = \Big(\frac{K_l(1 + pT_l)}{pT_l}\Big)\Big(\frac{1}{1 + pT_s}\Big)\Big(\frac{V_m}{p}\Big), \tag{3.11}$$

Table 3.4: Grid parameters

Parameters	values
V_m	311 V
f_g	50 Hz
T_s	$\frac{1}{8000}s$

where K_l and T_l are the proportional gain and the integral time constant of the PI controller; and T_s is the sampling time. The parameters of the PI controller of the PLL are tuned using Symmetrical Optimum as below [18];

$$T_l = a^2 T_s, \tag{3.12}$$

$$K_l = \frac{1}{aV_m T_s}, \tag{3.13}$$

and

$$\omega_c = \frac{1}{aT_s}. \tag{3.14}$$

In Equation (3.14), ω_c is the cross-over frequency of the PI controller and a is the normalisation factor.

3.3.1 Calculation of the PI parameters

It is advised that the cross-over frequency of the PI controller of the PLL should be close to the grid frequency [45]. The design of the PI controller should be done for a cross-over frequency value of $\omega_c \approx 314$ rad/s. Given the parameter of the grid as shown in Table 3.4, the parameters of the PI controller of the PLL are deduced as shown below;

$$a = \frac{5000}{2\pi 50} = 15.91, \tag{3.15}$$

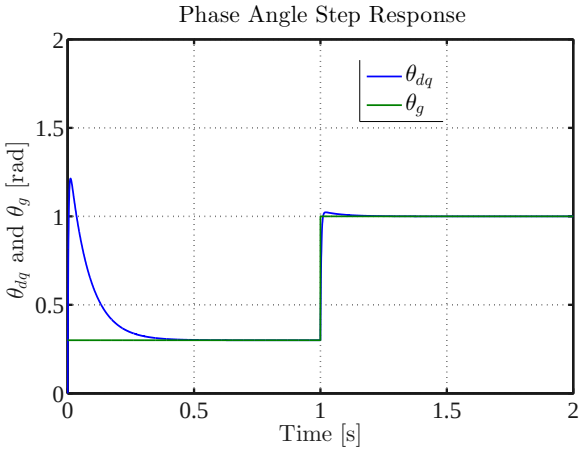

Figure 3.6: Step response of the voltage phase angle and dq0-reference frame phase angle

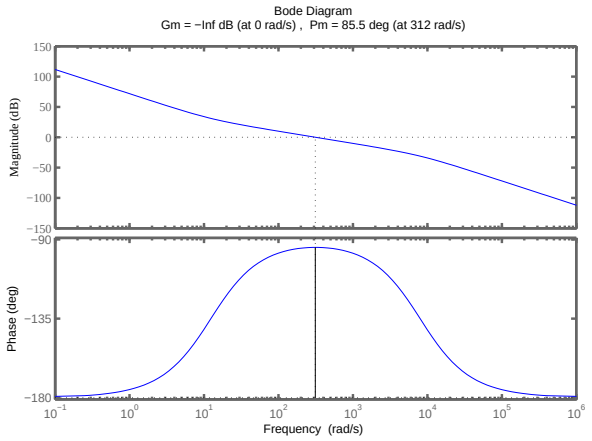

Figure 3.7: Bode plot of the open PLL open loop

$$T_l = \frac{a}{\omega_c} = \frac{15.91}{2\pi 50} = 0.051 \tag{3.16}$$

and

$$K_l = \frac{1}{aV_m T_s} = \frac{5000}{(15.91)(\sqrt{2})(220)} = 1.0067. \tag{3.17}$$

The time response of the PLL control loop (small signal analysis) is illustrated in Figure 3.6. It can be seen despite the high overshoot at the start, there is a good response to disturbance of the PI controller at 1 s. The fact that $\theta_g = \theta_s$ implies that the PLL works properly as shown in Figure 3.6. The cross over frequency and phase margin are displayed in Figure 3.7. It can be seen that the cross-over frequency is near the value expected when using Symmetrical Optimum method. The bandwidth is $\omega_c = 312$ rad/s. It can also be seen that the phase margin of the open loop PLL control loop is symmetrical at about the cross-over frequency.

3.4 Continuous Space Vector Modulation Implementation

In Section 2.7, it is shown that a three-phase two-level VSC offers eight switching states (six active switching states and two non-active). It can be seen from Figure 3.8 that these switching states form a hexagon with six sectors with 60 degree each. The space vector pulse width modulation (SV-PWM) consists of the mapping of the reference voltage space vector onto a hexagonal plan, as shown in Figure 3.8. The adjacent space vectors relate to each switching state of the VSC (active voltage space vectors), as shown in Table 3.5. At each sampling time, the reference voltage space vector is approximated with a combination of adjacent space vectors (active and non-active) applied with specific durations depending on the sector the reference vector is in. Bearing

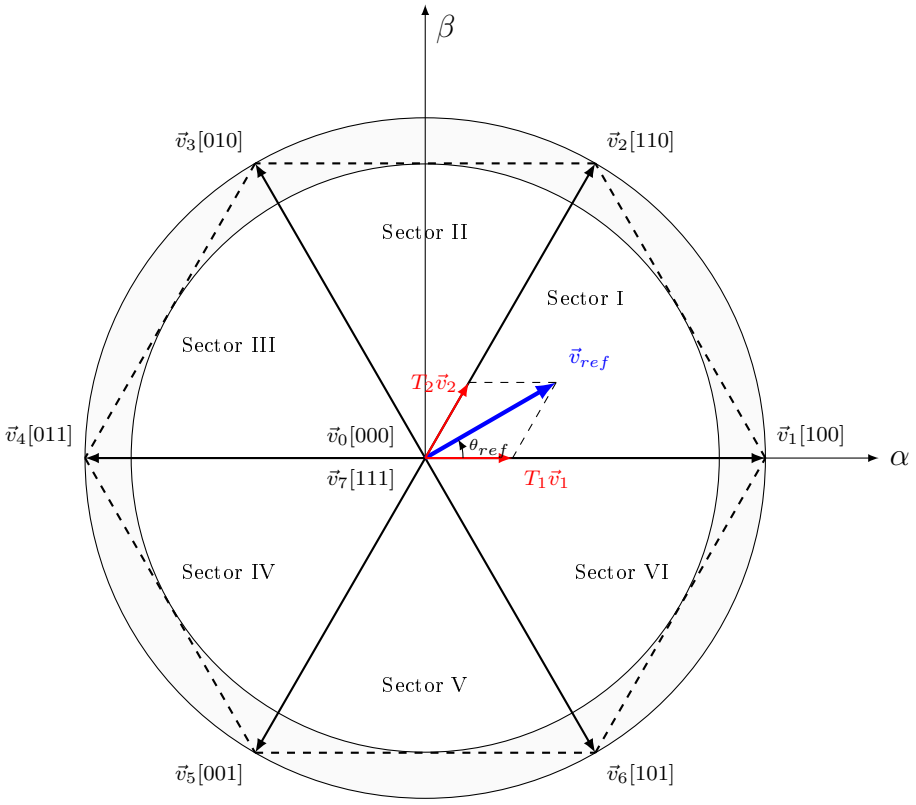

Figure 3.8: Space vector schemes for SVPWM

in mind that the non-active voltage space vectors are placed at the origin, the linear region is located in the circle inside the hexagon, as shown in Figure 3.8. The maximum reference voltage that can be properly approximated should be contained inside that circle, otherwise there will be some missing information. Hence, the radius of the circle inside the hexagon is the maximum magnitude of the reference voltage space vector; it is given by

$$|\vec{v}_{ref}| = \frac{2}{3} V_{dc} \cos\left(\frac{\pi}{3}\right). \tag{3.18}$$

The modulation index is defined as the ratio of the maximum reference voltage over the the fundamental of the voltage square wave. The modulation index is given by

$$m = \frac{\frac{2}{3} V_{dc} \cos(\frac{\pi}{6})}{\frac{2V_{dc}}{\pi}} = 0.904, \tag{3.19}$$

where m is the modulation index. The modulation index determines the operating region of the SV-PWM function. The SV-PWM function in the over-modulation region is not discussed in this thesis. This is why in terms of control it is necessary to limit the output of the inner control to avoid operating in the over-modulation region.

Table 3.5: Swiching segments according to each sector

Sectors	Switching segments						
I	$\vec{v}_0$,[000]	$\vec{v}_1$,[100]	$\vec{v}_2$,[110]	$\vec{v}_7$,[111]	$\vec{v}_2$,[110]	$\vec{v}_1$,[100]	$\vec{v}_0$,[000]
II	$\vec{v}_0$,[000]	$\vec{v}_3$,[010]	$\vec{v}_2$,[110]	$\vec{v}_7$,[111]	$\vec{v}_2$,[110]	$\vec{v}_3$,[010]	$\vec{v}_0$,[000]
III	$\vec{v}_0$,[000]	$\vec{v}_3$,[010]	$\vec{v}_4$,[011]	$\vec{v}_7$,[111]	$\vec{v}_4$,[011]	$\vec{v}_3$,[010]	$\vec{v}_0$,[000]
IV	$\vec{v}_0$,[000]	$\vec{v}_5$,[001]	$\vec{v}_4$,[011]	$\vec{v}_7$,[111]	$\vec{v}_4$,[011]	$\vec{v}_5$,[001]	$\vec{v}_0$,[000]
V	$\vec{v}_0$,[000]	$\vec{v}_5$,[001]	$\vec{v}_6$,[101]	$\vec{v}_7$,[111]	$\vec{v}_6$,[101]	$\vec{v}_5$,[001]	$\vec{v}_0$,[000]
VI	$\vec{v}_0$,[000]	$\vec{v}_1$,[100]	$\vec{v}_6$,[101]	$\vec{v}_7$,[111]	$\vec{v}_6$,[101]	$\vec{v}_1$,[100]	$\vec{v}_0$,[000]

The aim of the SV-PWM function is to provide the switching patterns with regard to the predefined space vectors depending on the sector the reference voltage space vector is in. The binary sequence in Figure 3.8 represents the switching patterns.

Assume that $\vec{v}_{ref}$ is constant during the switching period (T_{sw}). When the reference voltage vector ($\vec{v}_{ref}$) is located in sector I, it can be approximated using the space vectors composing the sector I with a specific duration. In Sector I, the reference voltage space vector can be approximated by applying $\vec{v}_1$ for a time period of T_1, $\vec{v}_2$ for a time period of the T_2 and both $\vec{v}_7 = 0$ and $\vec{v}_0 = 0$ for a time period T_0 as follows;

$$T_1\vec{v}_1 + T_2\vec{v}_2 = T_{sw}\vec{v}_{ref} \tag{3.20}$$

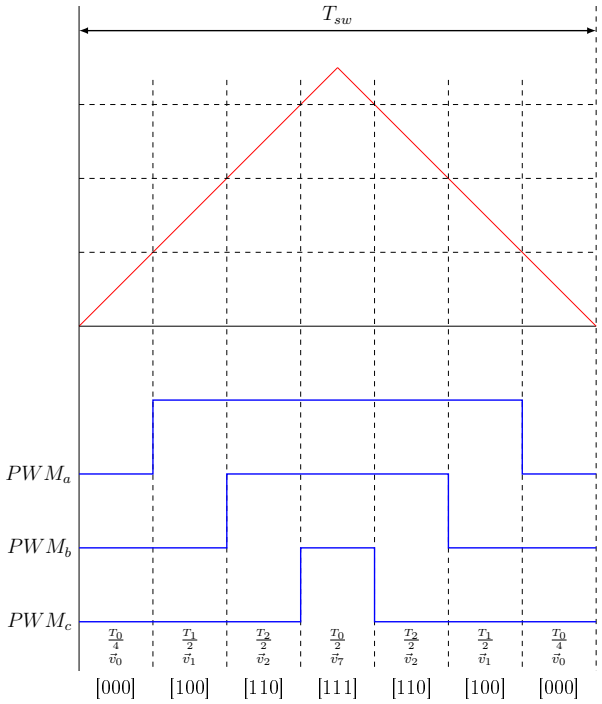

Figure 3.9: Symmetrical SVPWM waveforms

with

$$T_{sw} = T_1 + T_2 + T_0. \tag{3.21}$$

Splitting Equation (3.20) into its real component and its imaginary component yields

$$T_1|\vec{v}_1| + d_2|\vec{v}_2|\cos(\frac{\pi}{3}) = T_{sw}|\vec{v}_{ref}|\cos(\theta_{ref}) \tag{3.22}$$

and

$$T_2|\vec{v}_2|\sin(\frac{\pi}{3}) = T_{sw}|\vec{v}_{ref}|\sin(\theta_{ref}). \tag{3.23}$$

Solving Equation (3.23) and Equation (3.23) means that the time periods in Sector I are given by

$$T_1 = T_{sw}\frac{|\vec{v}_{ref}|}{|\vec{v}_1|}\frac{\sin(\theta_{ref} - \frac{\pi}{3})}{\sin(\frac{\pi}{3})} \tag{3.24}$$

and

$$T_2 = T_{sw}\frac{|\vec{v}_{ref}|}{|\vec{v}_2|}\frac{\sin(\theta_{ref})}{\sin(\frac{\pi}{3})}. \tag{3.25}$$

The same rules apply to Sectors II to VI when it comes to calculating the time periods. The time periods at any sector in a generalised way are given by

$$\begin{bmatrix} T_k \\ T_{k+1} \end{bmatrix} = \frac{\sqrt{3}T_{sw}}{2V_{dc}} \begin{bmatrix} \sin\frac{k\pi}{3} & -\cos\frac{k\pi}{3} \\ -\sin\frac{(k-1)\pi}{3} & \cos\frac{(k-1)\pi}{3} \end{bmatrix} \begin{bmatrix} v_\alpha \\ v_\beta \end{bmatrix}, \tag{3.26}$$

where k=1,2,...,6. The time period for the application of non-active vectors is given by

$$T_0 = T_{sw} - (T_k - T_{k+1}). \tag{3.27}$$

The symmetrical sequence of the SV-PWM signals allows the reduction of the harmonics as discussed in [46]. The symmetrical SVPWM scheme for sector I is displayed in Figure 3.9. It is important to notice that the most significant bit in the binary sequence relates to the phase A converter leg, while the least significant bit relate to the phase C converter leg, as depicted in Figure 3.9. The middle bit relates to the phase B converter leg, as shown in Figure 3.9. The symmetrical sequence of the SV-PWM allows only one leg to change state at a time. The symmetrical sequence consists of starting with a non-active vector, then switching one bit amongst the voltage space vectors with regard to the sector in which the reference voltage space vector is located in. A similar approach can be used for other sectors.

3.5 Control Strategy of the Grid-Side Converter

In this control strategy, an L approximation of the LCL filter ($\vec{i}_g \approx \vec{i}_c$) is assumed [27]. The mathematical models of the LCL filter and the L filter

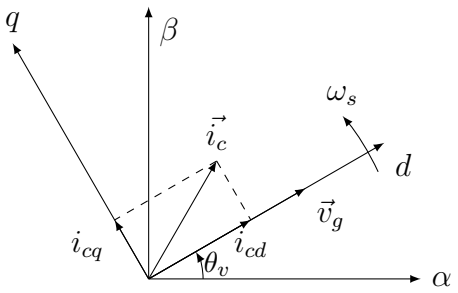

Figure 3.10: VOC scheme

are discussed in Section 2.8.1 and Secton 2.8.2. The aim of the GSC control is to maintain the DC link voltage constant and guarantee the unity power factor regardless of the disturbances in the system. In order to achieve these goals, most researchers use the concept of vector control in the synchronous dq0-reference frame with voltage-oriented control of the LSC [18, 27, 47]. The concept of voltage-oriented (VOC) control as shown in Figure 3.10, allows a decoupled control of the active and reactive power by regulating the d-axis and q-axis converter currents. In this control concept the PI controllers use is usually made. The expression of the PI controller is given by

$$PI = K_p \frac{(1 + pT_i)}{pT_i}, \tag{3.28}$$

where K_p is the proportional gain of the PI controller while T_i is the integral time of the PI controller. Also, the cascaded control structure is adopted where the control system consists of two control loops. These control loops are the inner control loop and outer control loop.

The control algorithm of the GSC is illustrated in Figure 3.11. At first glance, it can be seen from Figure 3.11, that the control system of the GSC requires accurate measurement of the three-phase grid voltage, the three-phase converter current and the DC-link voltage. In case where a power transformer is used to match the voltage level of the grid at the point of common coupling (PCC), the voltage at the secondary side is measured instead [27]. The locations of all the sensors of the needed electrical parameters for the control algorithm are displayed in Figure 3.11. The grid voltage angle is calculated by the phase locked loop. The phase locked loop implementation is discussed in Section 3.3. The measured electrical parameters are then transformed into the synchronous dq0-reference frame. The DC-link set value is compared to the measured DC-link voltage to provide the error to be processed by the PI controller of the outer DC-link voltage loop.

It is important to note that in the GSC the DC-link increases or decreases depending on the power coming from the grid with regards to the load. The

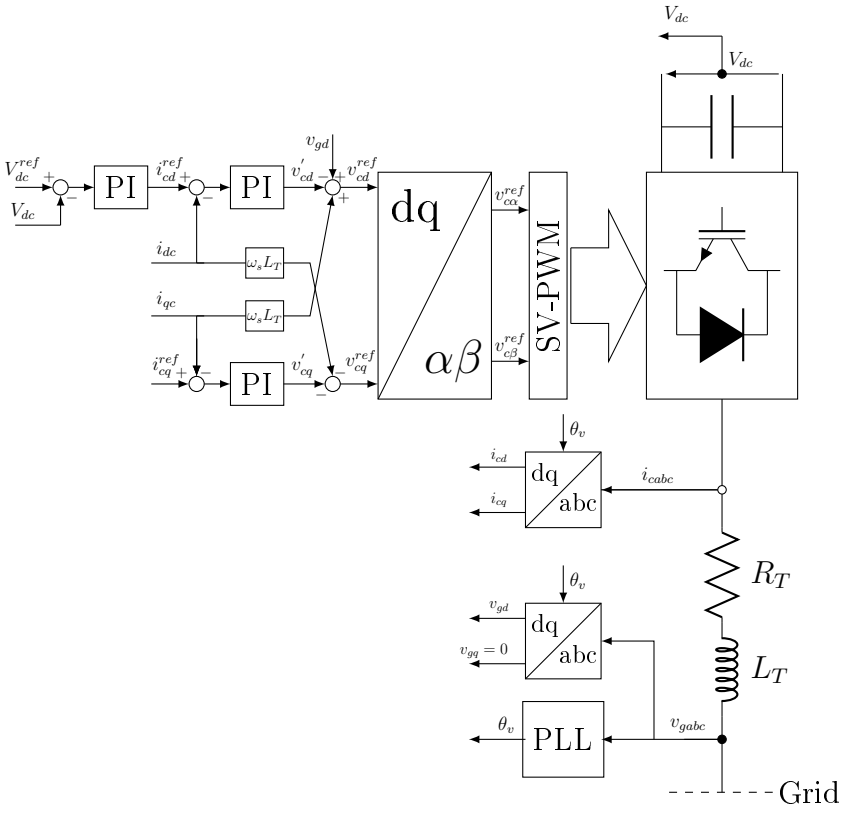

Figure 3.11: Control strategy scheme of the grid-connected VSC

relationship between the active power and the converter current is given by

$$P_g = \frac{3}{2}\Big(v_{gd}i_{gd} + v_{gq}i_{gq}\Big), \tag{3.29}$$

where P_g is the active power from the grid; v_{gd} and v_{gq} are the d-axis and q-axis grid voltages, respectively; and, i_{gd} and i_{gq} are the d-axis and q-axis grid currents. When aligning the synchronous dq0-reference frame along the d-axis grid voltage, the d-axis converter current is directly proportional to the grid active power. From Equation (3.29) it can be seen that if the d-axis grid voltage is constant, then the grid active power depends only on the d-axis grid current since $v_{gq} = 0$. Hence, the power regulation can be done through the d-axis current.

On the other hand, The grid reactive power is given by

$$Q_g = \frac{3}{2}\Big(v_{gq}i_{cd} - v_{gd}i_{cq}\Big), \tag{3.30}$$

where Q_g is the reactive power coming from the grid. From Equation (3.30), it can be seen that setting the reference q-axis current to zero implies that

the reactive power is zero as well since $v_{gq} = 0$. Hence by doing so, the unity power factor is achieved using the inner q-axis grid current loop. The outputs of the PI controllers $v_{cd}^{'}$ and $v_{cq}^{'}$ are subtracted to feed-forward compensation terms in order to guarantee good tracking of the grid currents, as shown in Figure 3.11. The feed-forward compensation terms are displayed in Equation (3.31). Then the command converter voltages (v_{cd}^{ref} and v_{cq}^{ref}) are transformed into $\alpha\beta 0$-reference frame ($v_{c\alpha}^{ref}$ and $v_{c\beta}^{ref}$), as shown in Figure 3.11. These are inputs of the SV-PWM function which provides switching patterns to the grid-side converter. The implementation of the SV-PWM function is discussed in Section 3.4.

3.5.1 Inner Converter Current Control

The dynamic behaviour of the AC side of grid-connected converter into the synchronous dq0-reference frame with the concept of voltage-oriented control is described by

$$\begin{bmatrix} v_{cd} \\ v_{cq} \end{bmatrix} = \underbrace{-R_T \begin{bmatrix} i_{gd} \\ i_{gq} \end{bmatrix} - L_T \frac{d}{dt} \begin{bmatrix} i_{gd} \\ i_{gq} \end{bmatrix}}_{\text{Plant}} + \underbrace{\omega_s L_T \begin{bmatrix} i_{gq} \\ -i_{gd} \end{bmatrix} + \begin{bmatrix} v_{gd} \\ 0 \end{bmatrix}}_{\text{Feed-forward compensation terms}}, \tag{3.31}$$

where $\boldsymbol{v_{cdq}}$ are the d-axis and q-axis converter voltages, respectively; R_T is the total filter resistance; $\boldsymbol{i_{gdq}}$ are d-axis and q-axis grid current, respectively; $L_T = L_g + L_c$ is the total filter inductance; and, ω_s is the synchronous angular speed. A block diagram of the current control loop is displayed in Figure 3.12.

From Equation (3.31), it can be seen that the d-axis and q-axis grid currents hold the same plant. This means that the transfer function of the PI controller in the inner current loop can be expressed by

$$\boldsymbol{v_{cdq}^{'}} = \left(\frac{K_i(1+pT_i)}{pT_i}\right)(\boldsymbol{i_{gdq}^{ref}} - \boldsymbol{i_{gdq}}). \tag{3.32}$$

The design of the PI controller parameters is done using Magnitude Optimum. This tuning method is extensively discussed in [18]. The proportional gain of the PI controller can be expressed by

$$K_i = \frac{T_{RL}}{2T_{ei}K_{PWM}K_{RL}}, \tag{3.33}$$

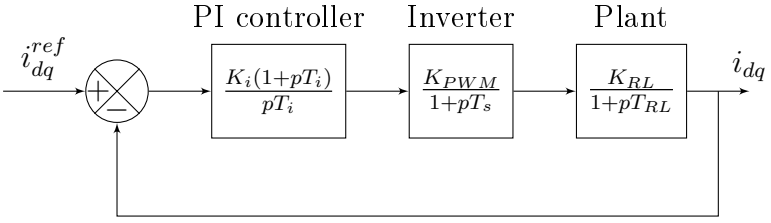

Figure 3.12: Block diagram of the inner current loop

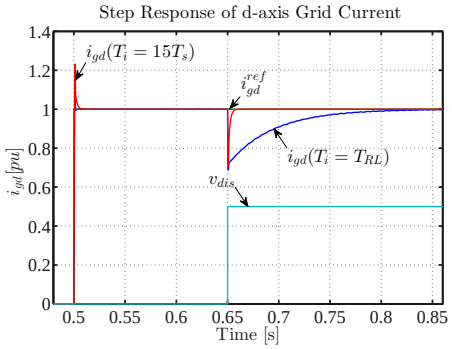

Figure 3.13: Step response of the d-axis grid current

where $T_{RL} = \frac{R_T}{L_T}$ is the time constant of the plant; K_{PWM} is the gain of the SV-PWM function ; K_{RL} is the gain of the plant; and, $T_{ei} = T_s + T_{PWM}$ is the total delay time introduced by the modulation technique (T_{PWM}) and the sampling time (T_s). In order to cancel the dominant pole in the plant, the integral time constant of the PI controller is given by

$$T_i = T_{RL}, \tag{3.34}$$

where T_i is the integral time constant of the PI controllers of the inner controller loop.

However, for better response to disturbance, it has been proposed in [18] that the integral time constant should be as shown below;

$$T_i = 15T_s, \tag{3.35}$$

The information about the dynamic response to disturbance of the inner d-axis and q-axis current are illustrated in Figure 3.13. It can be seen that the dynamic response of the PI controller of the inner current loop that makes use of the integral time constant of T_{RL}, the response time is very large compared to that of $15T_s$ at t=0.65 s. However, there is a high overshoot at roughly 25 % when both integral time constants are used. This is a drawback when the design of the PI controller is done using Magnitude Optimum. Hence, it is necessary to limit the outputs of the PI controller. However, limiting the outputs of the PI controllers alone will lead to larger overshoot therefore to the saturation of the converter. This problem is solved by applying an anti-windup algorithm. The anti-windup algorithm and limitations of the output of the PI controller are discussed in Section A.1. Besisdes, tuning the PI parameters obtained from design method can also reduce the overshoot during disturbances. The design of the PI controller using Magnitude Optimum leads to the cross-over frequency of $f_c \approx \frac{f_{sw}}{20}$ [18].

3.5.2 Outer DC-Link Voltage Control

The dynamic behaviour of the DC side of the grid-side converter in synchronous dq0-reference frame is expressed by

$$C_{dc}\frac{dV_{dc}}{dt} = I_{dc} - I_l, \tag{3.36}$$

where C_{dc} is the DC-link capacitor; V_{dc} is the DC-link voltage ; I_l the DC link load current; and, I_{dc} the current coming out of the converter at the DC side. The subscript dc relates to DC-link parameters.

In order to reduce harmonics in the system it is advised that the active power at the DC side should be equal to the active power at the AC side. this relationship is given by

$$I_{dc} = \frac{3}{2}\frac{v_{cd}i_{cd}}{V_{dc}}. \tag{3.37}$$

Substituting Equation (3.37) into Equation (3.36) yields

$$C_{dc}\frac{dV_{dc}}{dt} = \frac{3}{2}\frac{i_{cd}v_{cd}}{V_{dc}} - I_l. \tag{3.38}$$

In Equation (3.38), it can be seen that this equation is non-linear. In this way, a linearisation around the operating point (around V_{dc}^{ref}) can be considered. The transfer function of the DC side is given by

$$\frac{\Delta V_{dc}}{\Delta i_{cd}} = \frac{3}{2}\frac{v_{cd}}{V_{dc}^{ref}}\frac{1}{pC_{dc}}. \tag{3.39}$$

Rewriting Equation (3.39) as below;

$$\frac{\Delta V_{dc}}{\Delta i_{cd}} = \frac{1}{pT_c}, \tag{3.40}$$

where $T_c = \frac{2}{3}\frac{v_{dc}^{ref}C_{dc}}{v_{cd}}$ is constant. Another way of linearising Equation (3.38) is to use a change of variable by multiplying Equation (3.36) by V_{dc} which yields

$$\frac{1}{2}C_{dc}\frac{dW_{dc}}{dt} = P_{dc} - P_l, \tag{3.41}$$

where W_{dc} is the energy in the DC link; P_{dc} is the active power of the DC link; and, P_l is the active power consumed by the load. The linearisation as shown in Equation (3.40) is the one that is considered in this work. The transfer function of the outer PI controller is given by

$$\boldsymbol{i_{gdq}^{ref}} = \left(\frac{K_v(1+pT_v)}{pT_v}\right)(V_{dc}^{ref} - V_{dc}). \tag{3.42}$$

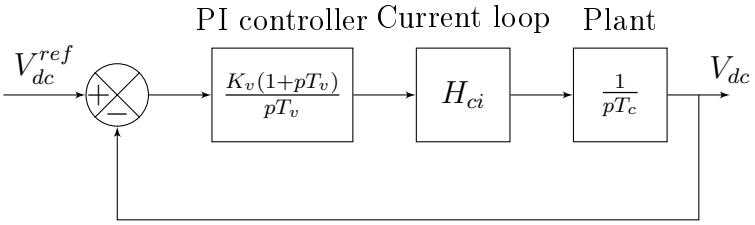

Figure 3.14: Block diagram of the voltage control loop

The tuning of the PI controller parameters of the outer DC-link voltage control loop is conducted using Symmetrical Optimum design method. The Symmetrical Optimum allows good disturbance rejection and the cross-over frequency resulting from that design method. It is a design method in which the amplitude and the phase of the bode plot of the open outer DC-link voltage control loop are symmetrical around the cross-over frequency. The cross-over frequency resulting from the Symmetrical Optimum design is approximate to $f_{co} = \frac{f_{sw}}{60}$ [18]. This is a considerable advantage since in a cascaded control system, the cross-over frequency in the inner loop should be at twice higher than the cross-over frequency of the inner control loop. However, this design method results to higher proportional gain. Hence, a tuning of the PI parameters determined by Symmetrical Optimum method is necessary.

The block diagrams of the outer DC-link voltage closed loop are illustrated in Figure 3.14. The outer DC-link voltage closed loop includes the inner current closed loop as shown in Figure 3.14. The inner current control closed loop can be approximated as a first order transfer function. The inner current control closed loop is given by

$$H_{ci} \approx \frac{1}{1 + pT_{ec}}, \tag{3.43}$$

where T_{ec} is the time constant of the inner current closed loop and H_{ci} is the transfer function of the inner current control closed loop. The integral time constant (T_v) and the proportional gain (K_v) of the PI controller in the outer DC-link voltage control loop are given by

$$T_v = 4a^2 T_{ec} \tag{3.44}$$

and

$$K_v = \frac{T_c}{4aT_{ec}}, \tag{3.45}$$

where a is the normalisation factor, chosen to be $a = 2.4$ [18].

3.5.3 Filter Effectiveness Factors

In order to compare the designed LCL filter and the designed L filter from an effectiveness point of view, the following effectiveness factors are used [27]:

1. The total harmonic distortion (THD) of the grid current and converter current, with
$$THD = \frac{\sqrt{\sum_{h=2}^{50} I^2(h)}}{I(1)}; \tag{3.46}$$
2. The average of the absolute value of the DC voltage error ΔV_{dc0}
3. Power factor $PF = \left(\frac{I(1)}{I}\right)\cos\varphi$;
4. The largest side band current harmonics around the switching frequency $I(h_{sw})$;
5. The overall efficiency $\eta = \frac{P_0}{P_1}$;

where I, $I(h)$ and φ are the total rms value of the current, the rms value of the h current harmonic and the angle between the fundamental current and voltage, respectively; and, P_0 and P_1 are the output and input powers, respectively.

3.6 Analysis of Simulation Results

The overall system using the LCL filter is investigated in MATLAB/SIMULINK with ODE 3, as solver. The GSC parameters are displayed in Table 3.6. The PI parameters used in the GSC are depicted in Table 3.6. The LCL filter parameters are displayed in Table 3.7. The design example of the LCL filter is discussed in Section 3.2.1. The SIMULINK models of the grid-connected VSC using either an L or LCL filters are depicted in Section E.1 and Section E.2, respectively.

Table 3.6: VSC Parameters and PI parameters

(a) VSC parameters

VSC parameters	values
S_b	8.7 kVA
f_{sw}	4 kHz
f_g	50 Hz
v_{ag}	380 V

(b) PI parameters of the control system

Inner current PI controller	values
K_i	1.6283
T_i	0.001875 s

Outer DC link PI controller	values
K_v	3.689
T_v	0.0216 s

Table 3.7: L and LCL filter Parameters

(a) LCL filter parameters

Filter parameter	values
L_c	4 mH
L_g	3 mH
C_f	9.6 μF
R_d	5 Ω
$R_T = R_c + R_g$	0.2 Ω

(b) L filter parameters

Filter parameter	values
L_T	7 mH
R_T	0.2 Ω

3.6.1 Comparative study between an L filter and an LCL filter from the effectiveness point of view

In this section, a comparative study is conducted between the LCL filter designed and the L filter with different load conditions. The comparative study is conducted considering the performance factors discussed in Section 3.5.3.

The information about the THD values of the grid currents in the grid-connected VSC based on the L filter and the LCL filter are given in Table 3.8 and Table 3.9, respectively. It can be seen that the lowest THD is 8.5 % for the grid-connected VSC using the LCL filter at rated conditions for a switching frequency of 4 kHz. This THD of 8.5 % is near the THD limit recommended in the IEEE standard 519-2014 (THD $\leq$ 8 %). In addition, compared to the L filter, the LCL filter performs better from a THD point of view at the different switching frequencies as well as different load conditions, as shown in Table 3.9 and Table 3.8.

On the other hand, one can notice that at switching frequency, the pres-

Table 3.8: Grid current THD with varying load when using an L filter

f_{sw} [Hz]	P_n	$\frac{2}{3}P_n$	$\frac{1}{3}P_n$
2500	14.45%	20.46%	38.25%
3000	12.02%	16.69%	35.26%
3500	10.04%	16.41%	31.32%
4000	9.02%	15.81%	30.27%

Table 3.9: Grid current THD with varying load when using an LCL filter

f_{sw} [Hz]	P_n	$\frac{2}{3}P_n$	$\frac{1}{3}P_n$
2500	14.36%	16.81%	31.32%
3000	10.88%	18.42%	35.43%
3500	10.8%	16.64%	32.9%
4000	8.5%	12.4%	25.35%

Table 3.10: LCL filter versus L filter

Effectiveness factors	LCL Filter	L filter
I_{hw}(A)	0.03	0.11
PF	≈ 1	≈ 1
ΔV_{dc0} [V]	≈ 0.55	≈ 0.63
η	96.8 %	98.77 %

ence of the filter capacitor of the LCL filter reduces the harmonic current by roughly a third compared to the system with the L filter, as displayed in Table 3.10. Further, for both filters, unity power factor is achieved, as depicted in Table 3.10. In addition, it can be seen that for both L and LCL filters, the average absolute DC link voltage errors (ΔV_{dc0}) are inferior to one, as shown in Table 3.10. Moreover, when neglecting the losses in the voltage-source converter, the overall efficiency of the system using the L filter is slightly better than that of the system using the LCL filter due to the presence of the damping resistor, as shown in Table 3.10.

3.6.2 Performance of the system (with LCL filter) under full load conditions

The results in Figure 3.15 and Figure 3.16 were obtained by running the grid-connected VSC under rated load conditions. It can be seen from Figure 3.15(a) and Figure 3.15(b) that the presence of the filter capacitor helps in the mitigation of harmonics in the converter current. In addition, it can be seen from Figure 3.16(a) that the unity power factor is achieved since the phase A current and voltage start at the same point. The pattern of the DC link voltage is shown in Figure 3.16(b).

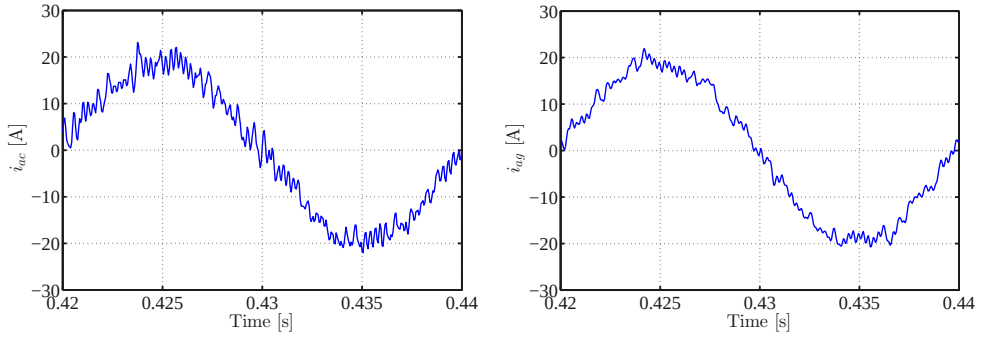

(a) (b)

Figure 3.15: Test of VSC under rated operating conditions: (a) Phase A converter current; (b) phase A grid current.

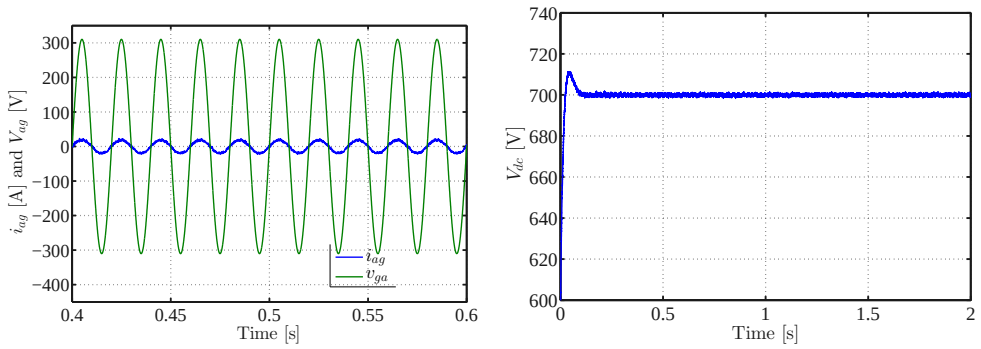

(a) (b)

Figure 3.16: Test of VSC under rated operating conditions: (a) phase A grid current and voltage; and, (b) DC link voltage.

3.6.3 Performance of the system (with LCL filter) under change in grid voltage amplitude

The results in Figure 3.17 and Figure 3.18 were obtained by changing the amplitude of the grid voltage between t=0.5 s and t=1 s (from 1 pu to 0.8 pu), as depicted in Figure 3.17(a) . It is worth noticing that the DC-link voltage increases or decreases depending on the active power drawn from the grid with regard to the load. Therefore, when the grid voltage magnitude decreases at t=0.5 s, the power coming from the grid decreases while the load remains constant. Hence, the DC-link voltage should decrease, as shown in Figure 3.17(b) at t=0.5 s. But, the control algorithm increases the three-phase grid current, instead, as depicted in Figure 3.18, in order to maintain the DC-link voltage by providing the rest of the power needed to maintain the DC-link voltage as the load remains constant. And when the grid voltage magnitude is back to normal at t=1 s, the control algorithm reduces the grid current, as shown in

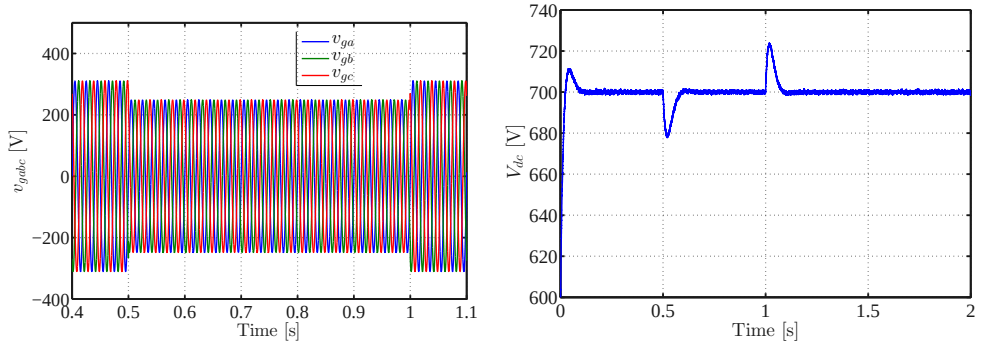

(a) (b)

Figure 3.17: Test of VSC under rated operating conditions: (a) three-phase grid voltage; and, (b) DC link voltage.

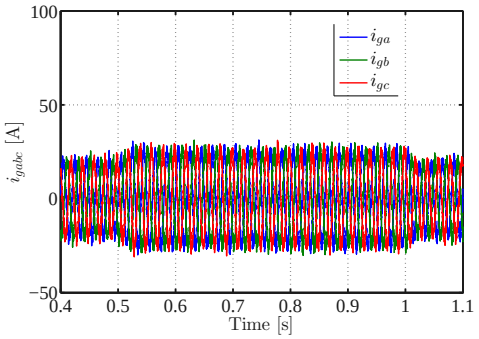

Figure 3.18: Three-phase grid current

Figure 3.18.

3.6.4 Conclusion

The implementation of different modules of the control system of the GSC was presented. Moreover, the design of the control strategy was presented. The conventional design procedure of an LCL filter with a design example were also presented.

Also, the design of the PI parameters was presented. Further, a comparative study between the L filter and LCL filter in the grid-connected VSC was conducted. It was found that the LCL filter perform slightly better than the L filters for switching frequencies less than 5 kHz which is different at high switching frequencies where the LCL filters outperform the L filters. The performance of the overall system was also investigated with the discussed control algorithm. It was shown that the presented control algorithm performs well under dynamic operating conditions.

Chapter 4

Rotor-Side Converter Control System

4.1 Introduction

In this chapter, control strategies of the grid-connected DFIG and the stand-alone DFIG system in WECS is discussed, and the design procedure of the PI controller is discussed. The simulations under dynamic operating conditions of the stand-alone DFIG system and grid-connected DFIG system are conducted to verify the performance of the proposed control strategies.

4.2 Control Strategy of the Rotor-Side Converter in Stand-Alone DFIG Systems

In stand-alone wind energy systems, keeping the voltage magnitude of the point of common coupling (stator voltage magnitude) and frequency constant become major issues since this system is connected directly to the load. Also, the power quality in the stand-alone DFIG system is a major issue. However, the power quality issues are not discussed in this thesis. In this way, the purpose of control strategy in the particular system presented here, is to maintain the voltage magnitude and the frequency constant regardless of the load connected to the standalone system and a change in wind as long as the generated power is higher than the load. In order to achieve these goals, a cascaded structure together with the field-orientation control theory (FOC) are used for this control algorithm. The field-orientation vector diagram and the voltage-orientation control diagram are depicted in Figure 4.1(b) and Figure 4.1(a), respectively.

The control algorithm of the stand-alone DFIG system is depicted in Figure 4.2. It can be seen that first, the three-phase stator voltage, three-phase stator current and the three-phase rotor current are measured. The position-

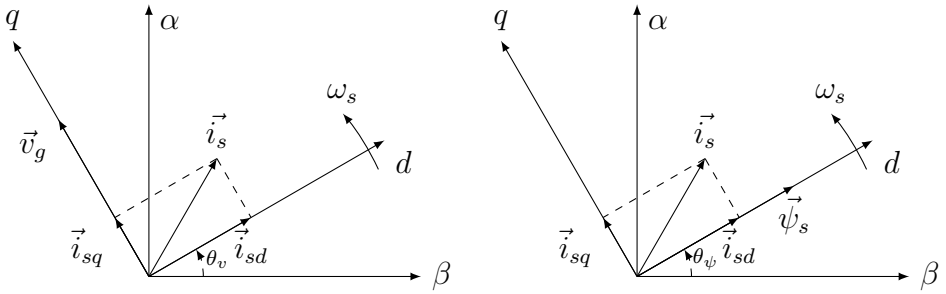

Figure 4.1: Vector diagram: (a) grid voltage-oriented control scheme; and, (b) stator flux-oriented control scheme

ing of each sensor is depicted in Figure 4.2. Since the stand-alone system is not connected to a stiff grid, there is no need of a phase locked loop (when using the VOC theory) or a stator flux angle calculation (when using the FOC theory). Instead, a reference synchronous angular frequency is set by the user depending on the operating frequency. Then, the stator angular angle of the flux is deduced from the integral of the set value of the synchronous angular frequency. Further, an encoder is used in order to measure the mechanical rotor angle which is converted to its electrical equivalent using the number of pair-poles. The three-phase parameters measured are then transformed into a synchronous dq0-reference frame. It is worth noticing that the three-phase rotor current is transformed into a synchronous dq0-reference frame using the slip angular phase $\theta_{slip} = \theta_s - \theta_r$. The control algorithm makes use of the PI controller. The transfer function of the PI used in this chapter is given by

$$PI(p) = \frac{(K_p p + K_i)}{p}, \tag{4.1}$$

where K_p and K_i are the proportional and the integral constant of the PI controller, respectively. Besides, the standard PI controller, the anti-windup algorithm and limitation of the output of the PI controller are also applied as shown in Section A.1 in order to avoid the saturation converter and current flowing in the system beyond the rated electrical parameters.

The set value of the stator voltage magnitude is compared to the measured stator voltage magnitude obtained by the square root of the sum of the square of the d-axis stator voltage and the square of the q-axis stator voltage, as shown in Figure 4.2. The error of the stator voltage magnitude is the input of the outer PI controller. The output of the outer PI controller is the reference d-axis rotor current, as depicted in Figure 4.2. The reference d-axis rotor current is then compared to the d-axis rotor current then inputted to the inner PI controller. The reference d-axis rotor voltage is obtained form the

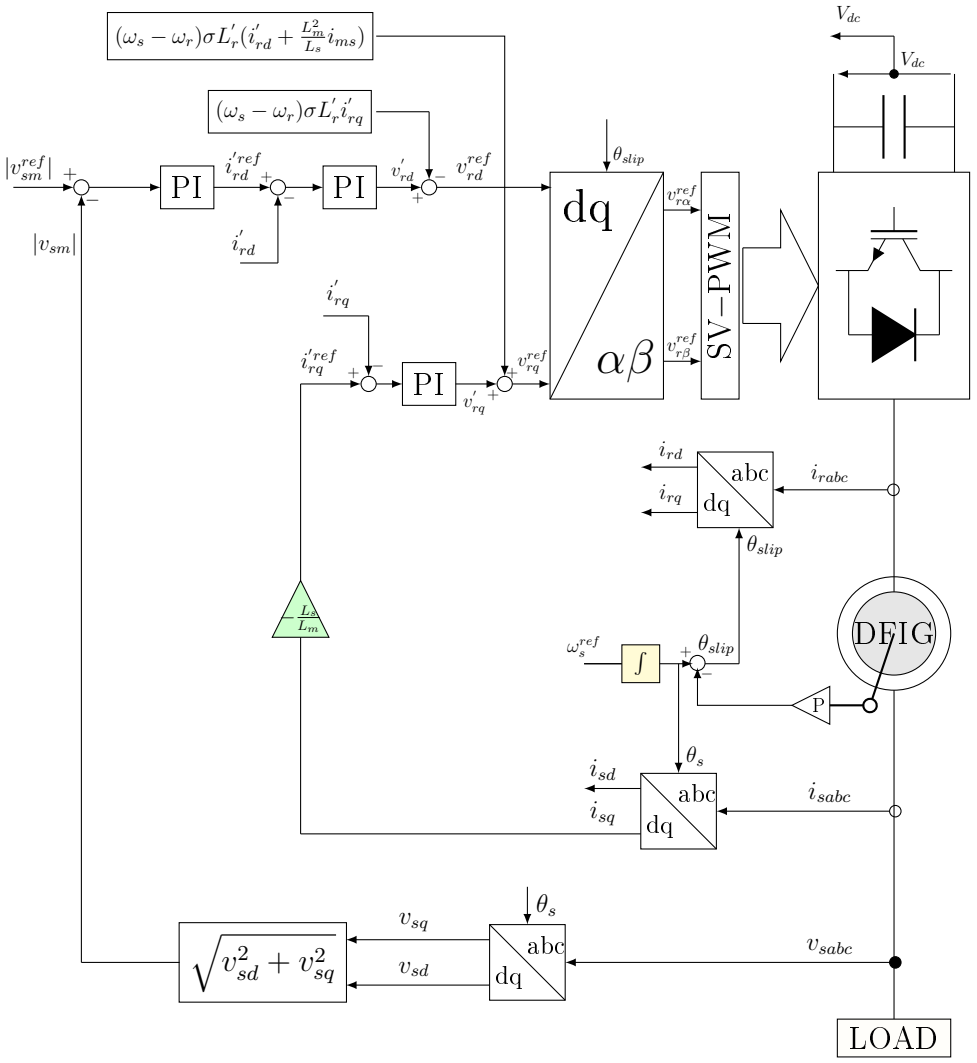

Figure 4.2: Control strategy scheme of the rotor side converter for stand-alone DFIG system

subtraction of the output of the PI controller by the compensation terms, as shown in Figure 4.2.

On the other hand, the reference q-axis current is chosen so as to force the d-axis flux linkage to aligne along the d-axis of the synchronous dq0-reference frame. This choice of q-axis reference current implies that the control algorithm chosen cannot achieve the maximum power point tracking (MPPT). The reference q-axis rotor current is then compared to the measured q-axis then inputted to the inner PI controller. The output of the PI controller is then added to the compensation terms as depicted in Figure 4.2 to obtain the reference q-axis rotor voltage.

Both the reference d-axis and q-axis rotor voltages are then transformed into the $\alpha\beta 0$-reference frame. These reference α-axis and β-axis rotor voltage quantities are inputted to the SV-PWM function in order to obtained the actuating signals. The SV-PWM implementation is discussed in Section 3.4.

4.2.1 Inner Rotor Current Control

The expressions of the three-phase rotor voltage into the synchronous dq0-reference frame are given by

$$v_{rd}^{'} = R_r^{'} i_{rd}^{'} + \frac{d}{dt}\psi_{rd}^{'} - (\omega_s - \omega_r)\psi_{rq}^{'} \tag{4.2}$$

and

$$v_{rq}^{'} = R_r^{'} i_{rq}^{'} + \frac{d}{dt}\psi_{rq}^{'} + (\omega_s - \omega_r)\psi_{rd}^{'} \tag{4.3}$$

The expressions of the rotor flux linkages into the synchronous dq0-reference frame are given by

$$\psi_{rd}^{'} = L_r i_{rd}^{'} + L_m i_{sd} \tag{4.4}$$

and

$$\psi_{rq}^{'} = L_r i_{rq}^{'} + L_m i_{sq}. \tag{4.5}$$

The expression of stator flux linkage space vector into the synchronous dq0-reference frame is given by

$$\psi_{sd} = L_s i_{sd} + L_m i_{rd}^{'} = L_m i_{sm}, \tag{4.6}$$

and

$$\psi_{sq} = L_s i_{sq} + L_m i_{rq}^{'}. \tag{4.7}$$

In Equation (4.6), i_{ms} is the magnetising current. Aligning the d-axis flux linkage ψ_{sd} along the d-axis of the synchronous dq0-reference frame implies that Equation (4.7) becomes

$$\psi_{sq} = 0. \tag{4.8}$$

Rewriting Equation (4.8) in terms of q-axis rotor current yields

$$i_{sq} = -\frac{L_m}{L_r} i_{rq}^{'}. \tag{4.9}$$

Substituting Equation (4.4)-(4.8) into Equation (4.2) and Equation (4.3) together with replacing $\frac{d}{dt}$ with the Laplace operator p yields

$$\begin{bmatrix} v_{rd}^{'} \\ v_{rq}^{'} \end{bmatrix} = \underbrace{R_r^{'} \begin{bmatrix} i_{rd}^{'} \\ i_{rq}^{'} \end{bmatrix} + \sigma L_r^{'} p \begin{bmatrix} i_{rd}^{'} \\ i_{rq}^{'} \end{bmatrix}}_{\text{Plant}} + \underbrace{(\omega_s - \omega_r) \begin{bmatrix} -\sigma L_r^{'} i_{rq}^{'} \\ \sigma L_r^{'} i_{rd}^{'} + \frac{L_m^2}{L_s} i_{ms} \end{bmatrix}}_{\text{Feed-forward compensation terms}}, \tag{4.10}$$

where $\boldsymbol{v'_{rdq}}$ are the d-axis and q-axis rotor voltage; $\boldsymbol{i'_{rdq}}$ is the d-axis and q-axis rotor current; $\sigma = 1 - \frac{L_m^2}{L_s L'_r}$ is a constant; and, ω_r is the electrical rotor angular speed. From Equation (4.10), the plant and the feed-forward compensation terms can be deduced. The transfer function of the inner PI controller is given by

$$\boldsymbol{v'_{rdq}} = \left(\frac{K_{rc}p + K_{rci}}{p}\right)(\boldsymbol{i'^{ref}_{rdq}} - \boldsymbol{i_{rdq}}), \tag{4.11}$$

where K_{rc} and K_{rci} are the proportional and integral constant of the inner PI controller.

4.2.1.1 Design of the Inner Rotor Current PI Parameters

The PI controller transfer function can be rewritten as follows;

$$PI(p) = \frac{K_{rcp}(p + c_i)}{p}, \tag{4.12}$$

where $c = \frac{K_{cri}}{K_{rcp}}$. The closed loop of the inner current controller is depicted in Figure 4.3. The transfer function of the plant is given by

$$H_{pc}(p) = \frac{K}{K_\tau + p}, \tag{4.13}$$

where K and K_τ are the parameters of the plant. By choosing c as shown below

$$c_i = K_\tau, \tag{4.14}$$

the open loop transfer function becomes

$$H_{ol}(p) = \frac{KK_{rcp}}{p}. \tag{4.15}$$

The closed loop transfer function for negative feedback is given by

$$H_{cl}(p) = \frac{H_{ol}(p)}{1 + H_{ol}(p)}. \tag{4.16}$$

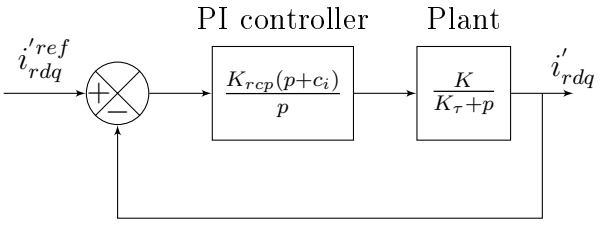

Figure 4.3: Block diagram of the inner rotor current loop

Hence, substituting Equation (4.15) into Equation (4.16) implies that the close loop transfer function is given by

$$H_{ci}(p) = \frac{KK_{rcp}}{KK_{rcp} + p}. \tag{4.17}$$

Since the closed loop transfer function of the inner current controller is a first order transfer function as shown in Equation (4.17), the bandwidth is given by

$$\omega_c = KK_{rcp}, \tag{4.18}$$

where ω_c is the bandwidth of the closed loop transfer function. The relationship between the rising time and the cross over frequency for a first order transfer function is given by

$$\omega_c = \frac{\ln(9)}{t_r}, \tag{4.19}$$

where t_r is the rising time which should be chosen as

$$t_r = 0.01s. \tag{4.20}$$

Substituting Equation (4.18) into Equation (4.19) yields

$$K_{rcp} = \frac{\ln(9)}{t_r K}(1 + \%d), \tag{4.21}$$

where $\%d$ is added so as the required rise time is achieved. Then, knowing the expression of the proportional constant K_{rc} and c_i, the expression of the integral constant of the inner PI controller is given by

$$K_{rci} = K_{rcp}c_i. \tag{4.22}$$

4.2.2 Outer Stator Voltage Amplitude Control

As mentioned above in Section 4.2, the aim of the control strategy is to maintain the stator voltage magnitude and the line frequency. The expression of the stator voltage space vector into the synchronous dq0-reference frame is given by

$$v_{sd} = R_s i_{sd} + \frac{d}{dt}\psi_{sd} - \omega_s \psi_{sq} \tag{4.23}$$

and

$$v_{sq} = R_s i_{sq} + \frac{d}{dt}\psi_{sd} + \omega_s \psi_{sd}. \tag{4.24}$$

In order to force the d-axis flux linkage space vector to be aligned along the d-axis synchronous dq0-reference frame, one can make use of Equation (4.8) by setting the reference q-axis rotor current, as shown below;

$$i'^{ref}_{rq} = -\frac{L_m}{L_s} i_{sq}. \tag{4.25}$$

Again, from Equation (4.25), it can be seen that in the stand-alone DFIG system, the maximum power power point tracking is not achieved since the q-axis rotor current depends essentially on the q-axis stator current, and here it is used to guarantee the field-orientation control theory. Substituting Equation (4.8) into Equation (4.23) and Equation (4.24) and neglecting the stator resistance yields

$$v_{sd} \approx 0 \tag{4.26}$$

and

$$v_{sq} = \omega_s \psi_{sd}. \tag{4.27}$$

Substituting Equation (4.6) into Equation (4.27) yields

$$v_{sq} = \omega_s (L_s i_{sd} + L_m i_{rd}^{'}) = \omega_s L_m i_{sm}. \tag{4.28}$$

By assuming that the magnetisation of the DFIG comes from only the rotor side of the DFIG implies that the magnitude of the rotor voltage is totally dependent on the d-axis rotor current. Using Equation (4.26) and Equation (4.27), the peak magnitude of the stator voltage is given by

$$v_{sm} = \sqrt{v_{sd}^2 + v_{sq}^2} \approx v_{sq}, \tag{4.29}$$

where v_{sm} is the peak magnitude of the stator voltage.

4.2.2.1 Design of the Outer PI Parameters

From Equation (4.29) and Equation (4.28), the transfer function of the outer control loop is deduced. This transfer function is given by

$$H_{pv}(p) = \frac{v_{sm}}{i_{rd}^{'}} = \omega_s L_m. \tag{4.30}$$

Hence, as it is shown in Figure 4.4, the transfer function of the open loop considering the inner current control loop is given by

$$H_{opv}(p) = \frac{K_{rvp}(c_v + p)}{p} \frac{KK_{rcp}}{KK_{rcp} + p} H_{pv}, \tag{4.31}$$

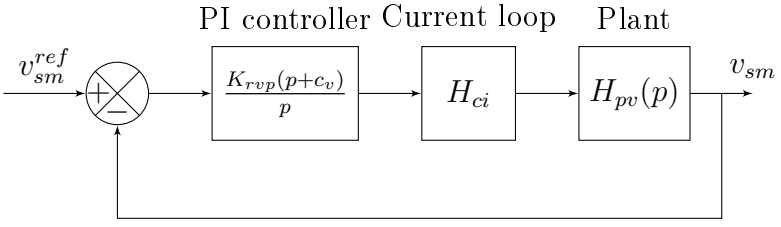

Figure 4.4: Block diagram of the voltage control loop

where K_{rvp} and $c_v = \frac{K_{rvi}}{K_{rvp}}$ are PI parameters. similar approach is used for the design of the PI controller used in Section 4.2.1.1. When choosing $c_v = KK_{rcp}$ yields that the outer open loop power controller is given by

$$K_{rvp} = \frac{\ln(9)}{t_r K K_{rcp} H_{pv}}(1 + \%d), \tag{4.32}$$

and

$$K_{rvi} = K_{rvp} c_v. \tag{4.33}$$

It is important to notice that for the outer PI controller, it is better to choose the rising time given below;

$$t_r = 0.1s. \tag{4.34}$$

Once the design of the outer PI controller parameters is finished, one can use MATLAB for the tuning of the outer PI parameters.

4.3 Control Strategy of the Rotor-Side Converter in Grid-connected DFIG Systems

Since the inner current control loop for both stand-alone and grid-connected DFIG systems are similar, the inner current control is not discussed in this section. The control strategy for the grid-connected DFIG system is depicted in Figure 4.6. The cascaded control structure with PI controller is chosen with the inner current controller and outer control loop with the regulation of stator active and reactive power.

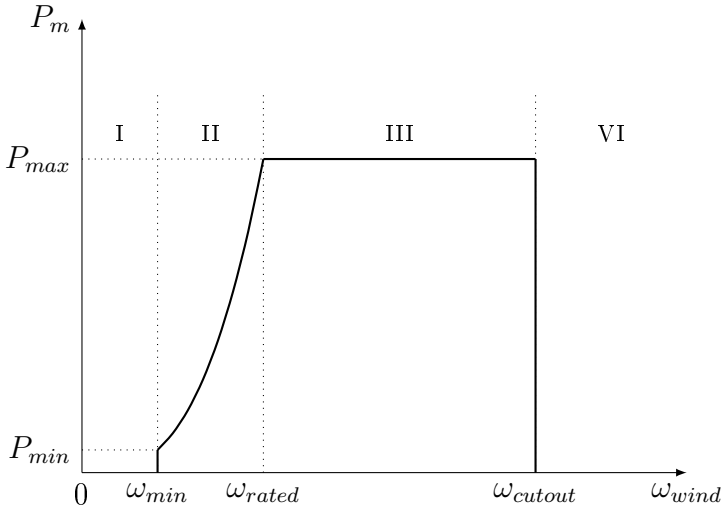

Figure 4.5: Mechanical power versus wind speed

The chosen control structure is similar to that chosen in Section 4.2. It can be seen that the three-phase stator voltage, the three-phase rotor current, three-phase stator current are measured, as shown in Figure 4.6. The rotor parameters(the three-phase rotor current is then referred into stator quantity using the turn-ratio n). There are two popular way of orienting the synchronous dq0-reference frame. These are the FOC and the VOC. In the FOC, the three-phase stator voltage and current are transformed into the $\alpha\beta 0$-reference frame in order to calculate the stator flux linkage angle. The stator flux linkage space vector transformed into the $\alpha\beta 0$-reference frame is given by

$$\psi_{s\alpha} = \int (v_{s\alpha} - R_s i_{s\alpha}) \tag{4.35}$$

and

$$\psi_{s\beta} = \int (v_{s\beta} - R_s i_{s\beta}), \tag{4.36}$$

where $\psi_{s\alpha}$ and $\psi_{s\beta}$ are the α-axis and the β-axis stator flux linkage; $v_{s\alpha}$ and $v_{s\alpha}$ are the α-axis and β-axis stator voltages; $i_{s\alpha}$ and $i_{s\beta}$ are the the α-axis and the β-axis stator currents; and, R_s is the stator resistance. The flux linkage angle is calculated using Equation (4.35) and Equation (4.36). The flux angle is given by

$$\theta_\psi = \arctan\left(\frac{\psi_{s\beta}}{\psi_{s\alpha}}\right), \tag{4.37}$$

where θ_ψ is the stator flux linkage angle. However, the FOC is not used in this thesis.

However, in this thesis, the voltage-oriented control along the q-axis of the dq0-reference frame is used. Hence, the use of the phase locked loop is necessary. The implementation of the phase locked loop is discussed in Section 3.3. The only difference is that the grid vector angle is to be used. The grid voltage angle is given by

$$\theta_s = \theta_v + \frac{\pi}{2}, \tag{4.38}$$

where θ_s is the angle when aligning the stator voltage space vector along the q-axis of the synchronous reference frame. Since the VOC is used, the stator active power is proportional to the q-axis rotor voltage and the stator reactive power depends on the q-axis rotor voltage, as will be seen below.

The reference generation of the stator active power is done following the MPPT algorithm. In this control strategy only region II as shown in Figure 4.5 is considered. So, no pitch control is activated. Hence the reference active power is deduced from the rotor speed (wind speed). The reference stator active power is given by

$$P_s^{ref} = k_{opt}\omega_r^3, \tag{4.39}$$

where k_{opt} depends on the characteristics of the wind turbine. The reference stator reactive power is deduced using the chosen stator power factor. Hence the reference reactive power is given by

$$Q_s^{ref} = \frac{\sqrt{1-\cos^2\phi}}{\cos\phi} P_s^{ref}, \tag{4.40}$$

where $\cos\phi$ is the stator power factor. As mentioned above the control strategy make use of two loops (inner and outer), with the outer loop regulating the power and the inner loop regulating the current as shown in Figure 4.6. Depending on the operating condition (stator power factor and wind speed), the references of the active and reactive powers are calculated and compared to the measured stator active and reactive powers. The stator active and reactive powers can also be approximated using Equation (4.43) and Equation (4.44). Then the outputs of outer PI controllers are the reference q-axis rotor current and the reference d-axis rotor current, respectively. The inner rotor current control of the RSC in grid-connected DFIG systems is similar to that discussed in Section 4.2.1.

4.3.1 Outer Power Control

The orientation of the q-axis synchronous reference frame along the stator voltage space vector is similar to the alignment of the synchronous d-axis reference frame along the flux linkage space vector since aligning the stator voltage along the synchronous q-axis reference frame means that $v_{sd} \approx 0$ and $\psi_{sq} \approx 0$. Using Equation (4.8) implies that the q-axis stator current can be written as an expression of the q-axis rotor current as shown below;

$$i_{sq} = -\frac{L_m}{L_s} i_{rq}^{'}. \tag{4.41}$$

The expression of the stator active power is given by

$$P_s = \frac{3}{2}(v_{sd} i_{sd} + v_{sd} i_{sd}). \tag{4.42}$$

Substituting Equation (4.29), Equation (4.41) and Equation (4.26) into Equation (4.42) yields

$$P_s = -\frac{3}{2}\frac{L_m}{L_s}(v_{sq} i_{rq}^{'}) \approx -\frac{3}{2}\frac{L_m}{L_s}(v_{sm} i_{rq}^{'}). \tag{4.43}$$

It can be seen from Equation (4.43) that the stator active power is directly proportional to the q-axis rotor current. On the other hand the stator reactive power is given by

$$Q_s = \frac{3}{2}(v_{sq} i_{sd} - v_{sd} i_{sq}). \tag{4.44}$$

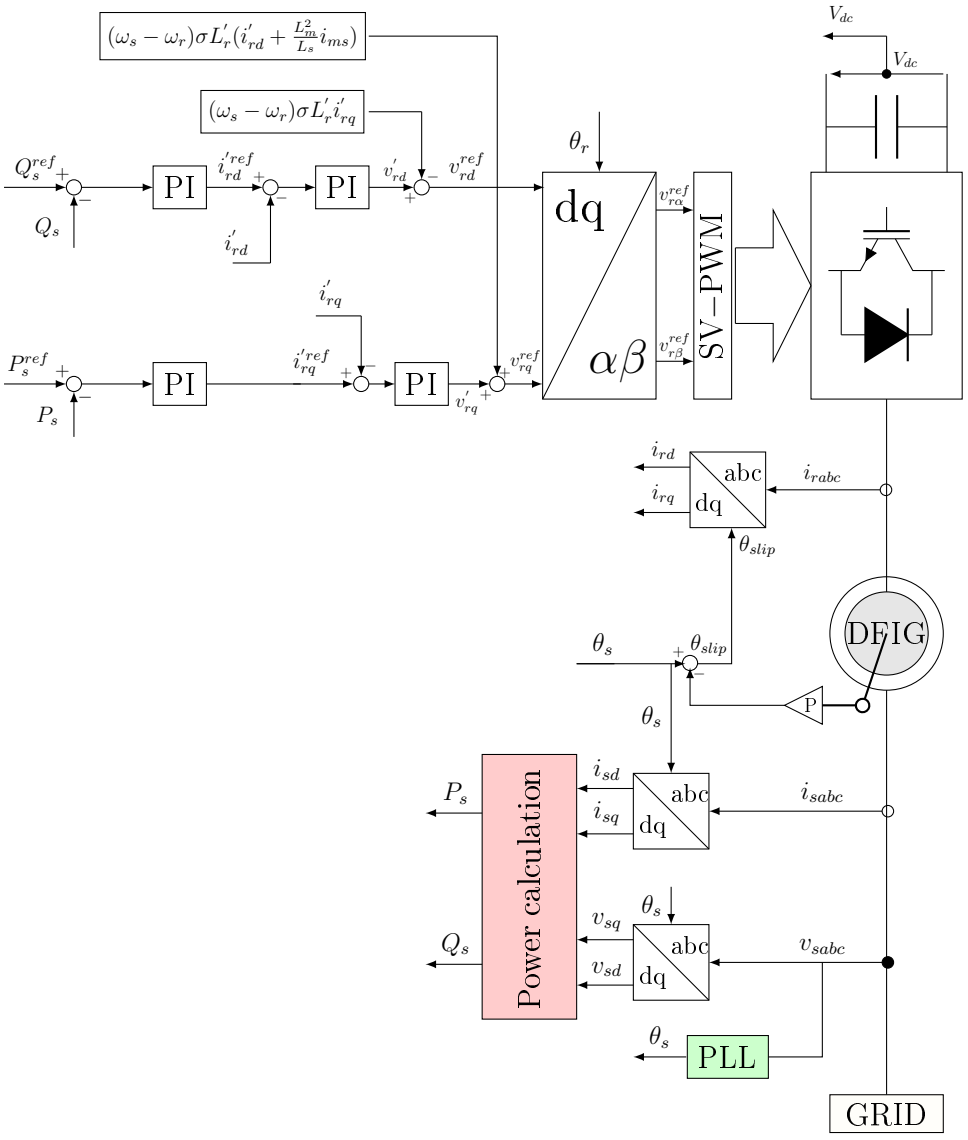

Figure 4.6: Control strategy scheme of the rotor side converter of the grid-connected DFIG system

Rewriting Equation (4.6) in order to have an expression in terms of the d-axis stator current yields

$$i_{sd} = \frac{1}{L_s}(\psi_{sd} - L_m i_{rd}'). \tag{4.45}$$

Substituting Equation (4.26) and Equation (4.45) into Equation (4.44) yields

$$Q_s = \frac{3L_m}{2L_s} v_{sq}\left(\frac{\psi_{sd}}{L_m} - i_{rd}'\right) \approx \frac{3L_m}{2L_s} v_{sm}\left(\frac{\psi_{sd}}{L_m} - i_{rd}'\right). \tag{4.46}$$

Assuming that the d-axis stator flux linkage is constant, it can be seen from Equation (4.46), that the stator reactive power depends on the d-axis rotor

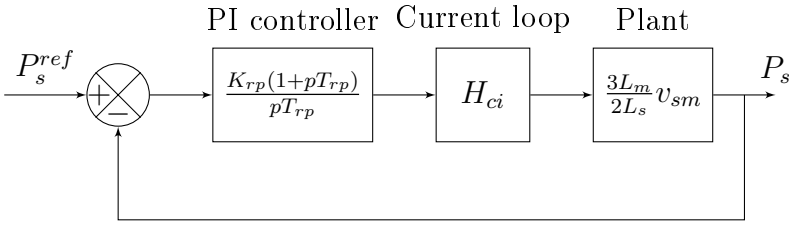

Figure 4.7: Block diagram of the voltage control loop

current.

From Equation (4.42) and Equation (4.46), it can be seen that both the active and reactive powers hold the same transfer function. The transfer function of the outer power control is given by

$$H_{pp}(p) = \frac{3L_m}{2L_s} v_{sq}. \tag{4.47}$$

The outer power control loop is displayed in Figure 4.7. The design of the parameters of the PI controllers is done in similar manner as in Section 4.2.2.1 by just replacing $H_{pv}(p)$ with $H_{pp}(p)$.

4.4 Analysis and Simulation of a Stand-alone DFIG System in WECS

The simulation in stand-alone DFIG system is conducted in MATLAB/SIMULINK. The start-up of the DFIG system in stand-alone system is not considered in this thesis. The machine parameters are displayed in Table B.4. The parameters of the PI controllers are depicted in Table 4.1. The SIMULINK model of the stand-alone RSC is displayed Section E.3.

Table 4.1: PI parameters

Inner rotor current PI controller	values
K_{rcp}	0.87
K_{rci}	464
Outer stator voltage amplitude PI controller	values
K_{rvp}	0.0062
K_{rvi}	109

4.4.1 Super-Synchronous Operating Mode

Figure 4.8, Figure 4.9, Figure 4.10 and Figure 4.11 were obtained by applying a constant speed of 1576 rpm, as shown in Figure 4.8(a). The stand-alone DFIG system was connected to a balanced resistive load of 13 kW.

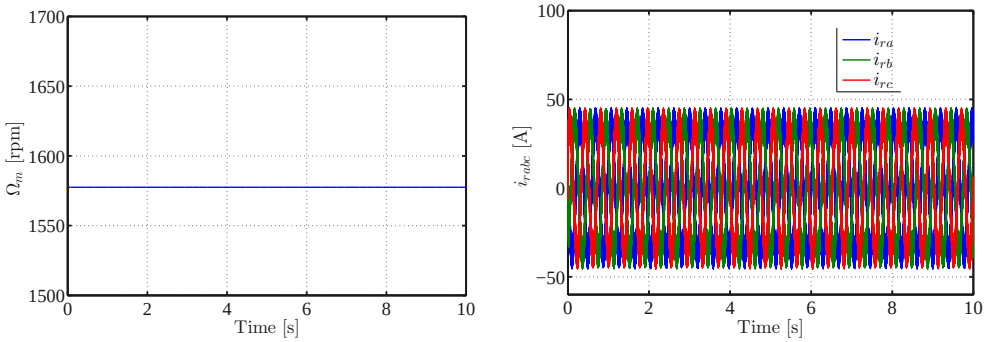

(a) (b)

Figure 4.8: Testing of a stand-alone DFIG system at super-synchronous speed: (a) measured mechanical shaft speed; and, (b) measured three-phase rotor current.

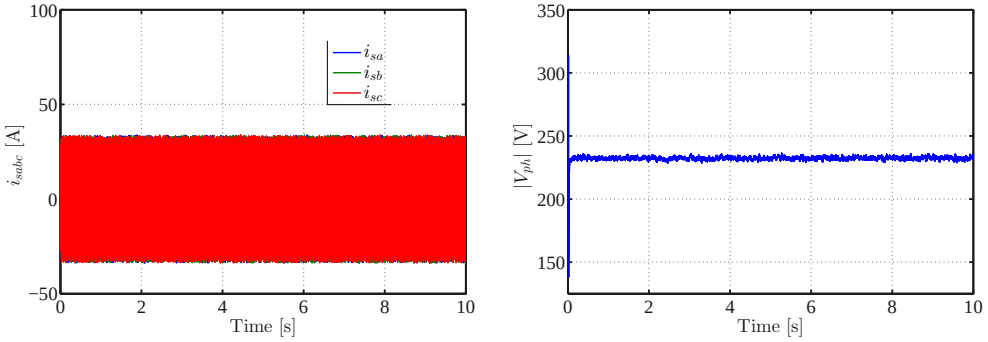

(a) (b)

Figure 4.9: Testing of a stand-alone DFIG system at super-synchronous speed: (a) measured three-phase stator current; and, (b) measured stator voltage magnitude.

The rotor current is pulsating at slip frequency $f_r = 2.52$ Hz and the stator current is pulsating at $f_s = 50$ Hz as depicted in Figure 4.8(b) and Figure 4.9(a), respectively. One of the aims of the control algorithm in stand–alone system is to maintain the frequency constant since the stand-alone system is not connected to a stiff grid. Furthermore the stator voltage magnitude is kept at a voltage amplitude of roughly $V_{sph} = 230$ V, as shown in Figure 4.9(b). According to the IEEE standard 519-2014 where the voltage magnitude should be at the range of more or less 5 % of the rated voltage magnitude. The three-stator voltage pattern is illustrated in Figure 4.10(a) where it can be seen that the envelope of the three-phase stator voltage remains constant, and as expected since the stator magnitude voltage is constant as depicted in Figure 4.9(b). Also, from Figure 4.10(b) obtained by zooming in the three-phase stator voltage, it can be noted that the three-phase stator voltage is pulsating at $f_s = 50$ Hz. Since the stand-alone system is connected to a resistive load it can be seen from Figure 4.11 that the stator current and voltage start at the

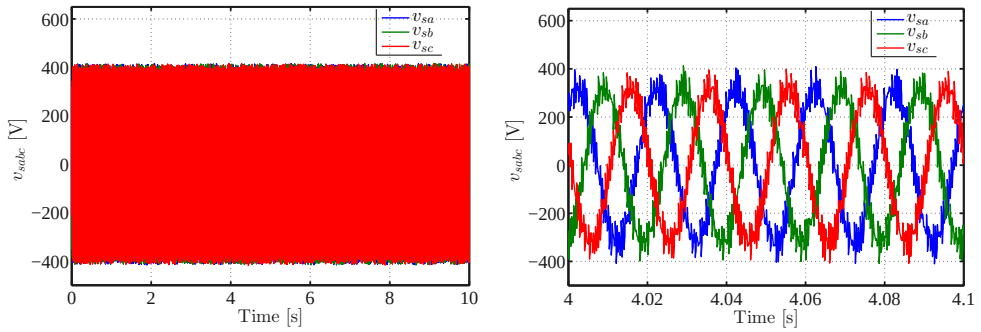

Figure 4.10: Test of a stand-alone DFIG system at super-synchronous speed : (a) Measured three-phase stator voltage ; (b)Measured three-phase stator voltage.

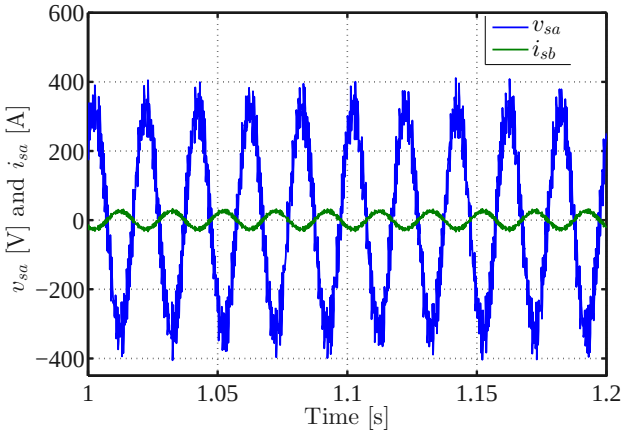

Figure 4.11: Three-phase stator current

same point which means that the unity power factor is achieved.

4.4.2 Sub-Synchronous Operating Mode

In sub-synchronous mode as can be seen in Figure 4.12(a), the DFIG runs at $\Omega_m = 1200$ rpm. The envelope of the three phase rotor current and that of the current voltage remains constant since there is no change in load, as depicted in Figure 4.12(b) and Figure 4.12(c). In addition, the stator voltage frequency is kept at 50 Hz as shown in Figure 4.12(c). The stator voltage magnitude remains constant as set by the control algorithm, as shown in Figure 4.12(d).

As can be seen in Figure 4.12(d), the three phase voltage envelop is kept constant in Figure 4.13(a). Figure 4.13(b) was obtained by zooming in the three-phase stator voltage in order to see its frequency which is at $f_s = 50$ Hz.

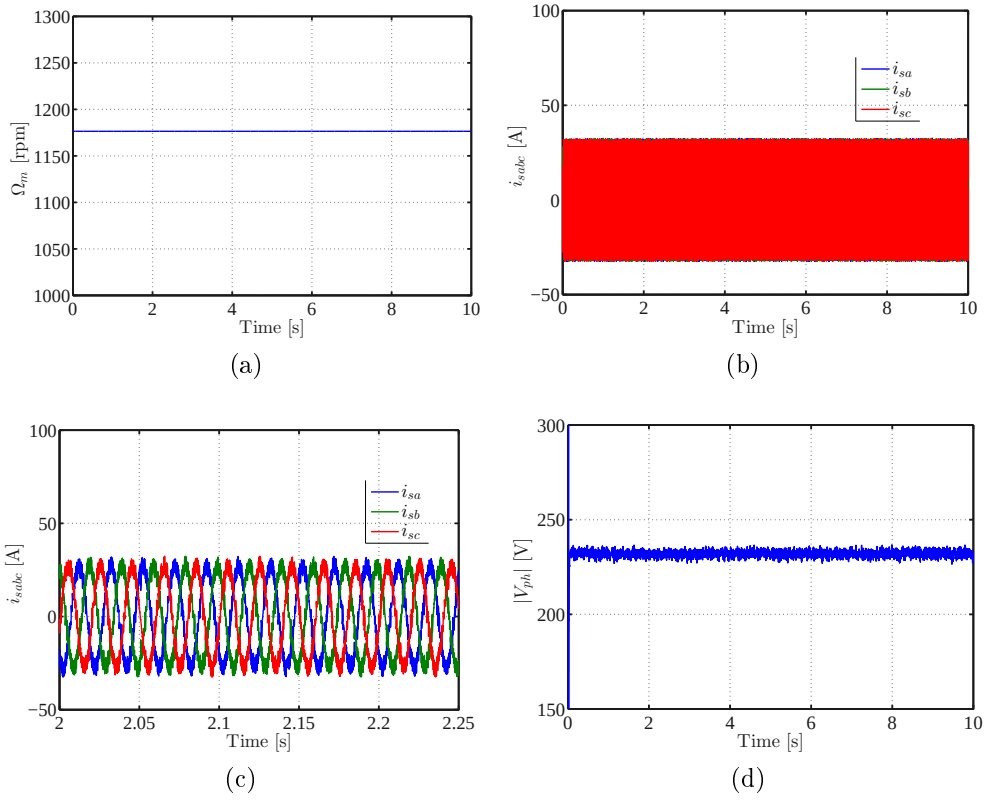

Figure 4.12: Testing of stand-alone DFIG system at sub-synchronous speed: (a) measured mechanical shaft speed; (b) measured three-phase rotor current; (c) measured zoomed three-phase rotor current; and, (d) measured stator voltage magnitude.

Again, since the load is resistive, the stator voltage and the stator current should start at the same point, as is shown in Figure 4.14(a). The three-

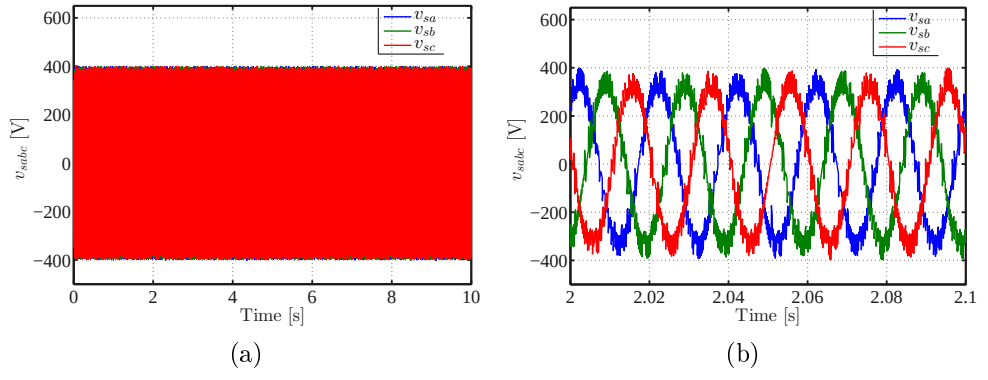

Figure 4.13: Testing of stand-alone DFIG system at sub-synchronous speed : (a) measured three-phase stator voltage ; (b) measured zoomed three-phase stator voltage.

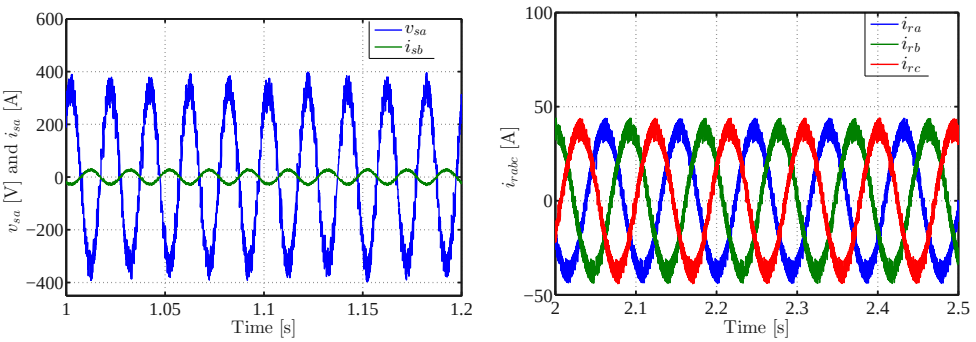

(a) (b)

Figure 4.14: Testing of a stand-alone DFIG system at sub-synchronous speed: (a) measured stator phase A voltage and current; (b) measured zoomed three-phase rotor current.

phase rotor current is pulsating at slip frequency of $f_r = 8.5$ Hz as shown in Figure 4.14(b).

4.4.3 Steady Change in Rotor Shaft Speed

Figure 4.15 was obtained by steadily varying the mechanical shaft speed from 1715 rpm to 1257 rpm, as shown in Figure 4.15(a). It can be seen that the magnitude voltage remains constant regardless of the change in speed, as depicted in Figure 4.15(b). Concerning the three-phase rotor current, it can be seen in Figure 4.16(a), that it slows down near the synchronous speed as its frequency results from the difference of the stator frequency and the electrical mechanical frequency. The three-phase stator current envelop remains constant even if the speed changes from super-synchronous speed to sub-synchronous speed, as illustrated in Figure 4.16(b).

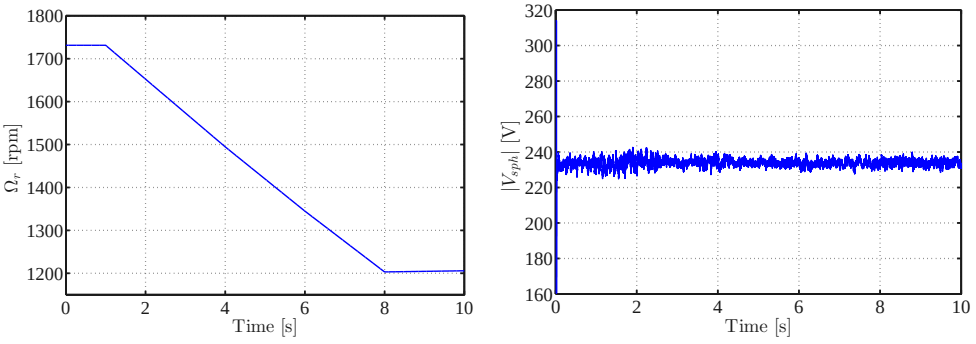

(a) (b)

Figure 4.15: Testing of a stand-alone DFIG system at sub-synchronous speed: (a)measured mechanical shaft speed; and, (b) measured stator voltage magnitude.

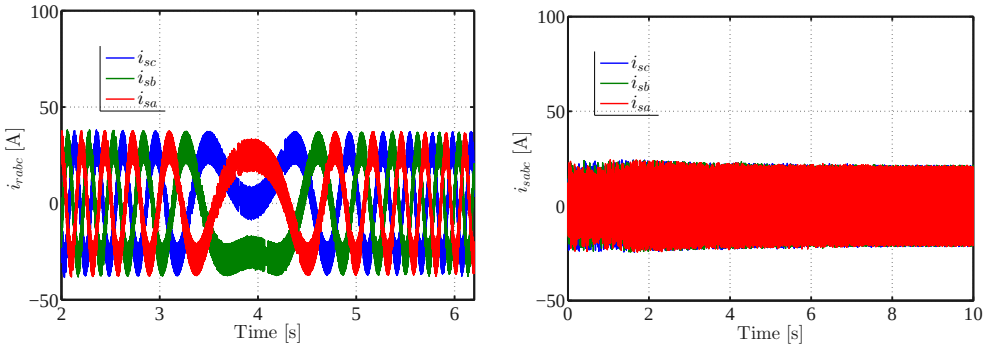

(a) (b)

Figure 4.16: Testing of a stand-alone DFIG system during steady change in speed: (a) measured three-phase rotor current; and, (b) measured three-phase stator current.

4.5 Simulation of a Grid-Connected DFIG Systems in WECS

The simulation in grid-connected DFIG system is conducted in MATLAB/SIMULINK. The machine parameters are displayed in Table B.6. The parameters of the PI controllers is are depicted in Table 4.2. The SIMULINK model of the grid-connected RSC is displayed Section E.4.

Table 4.2: PI parameters

Inner rotor current PI controller	values
K_{rcp}	0.89
K_{rci}	3.04534
Outer stator voltage amplitude PI controller	values
K_{rpp}	0.0727
K_{rpi}	17.54

4.5.1 Performance of the WECS under Steady Wind Speed Change

The performance of the WECS under constant power factor ($\cos\phi = 0.8$ lagging) together with the steady wind speed change is depicted in Figure 4.17 and Figure 4.18. The WECS starts with a wind speed of 7.6 m/s and it operates under constant stator power factor, as shown in Figure 4.17(a) and Figure 4.17(b). The corresponding MPPT mechanical shaft speed set point of the generator is at 860 rpm, as shown in Figure 4.18(a).

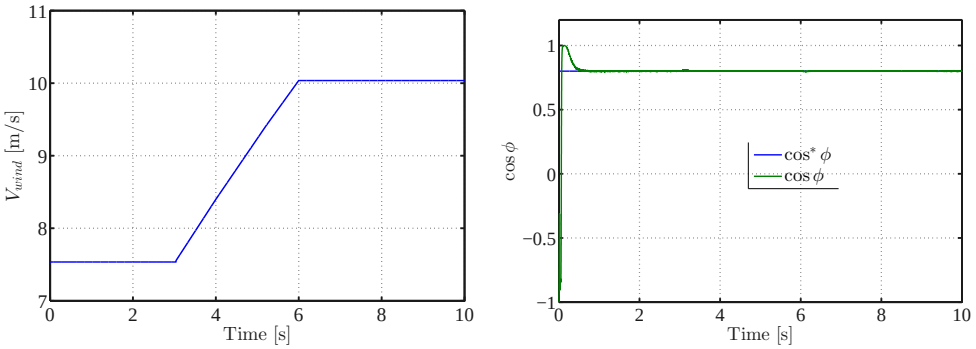

Figure 4.17: Test of WECS under steady wind speed change: (a) wind speed; and, (b) stator power factor.

The DFIG operates under sub-synchronous operating conditions. At this speed (Ω_m =875 rpm), when the DFIG starts, there is a short transient period before the stator and rotor powers settle to the steady-state values corresponding to the MPPT, as shown in Figures 4.18(b)-(d) and Figure 4.19(a) . These

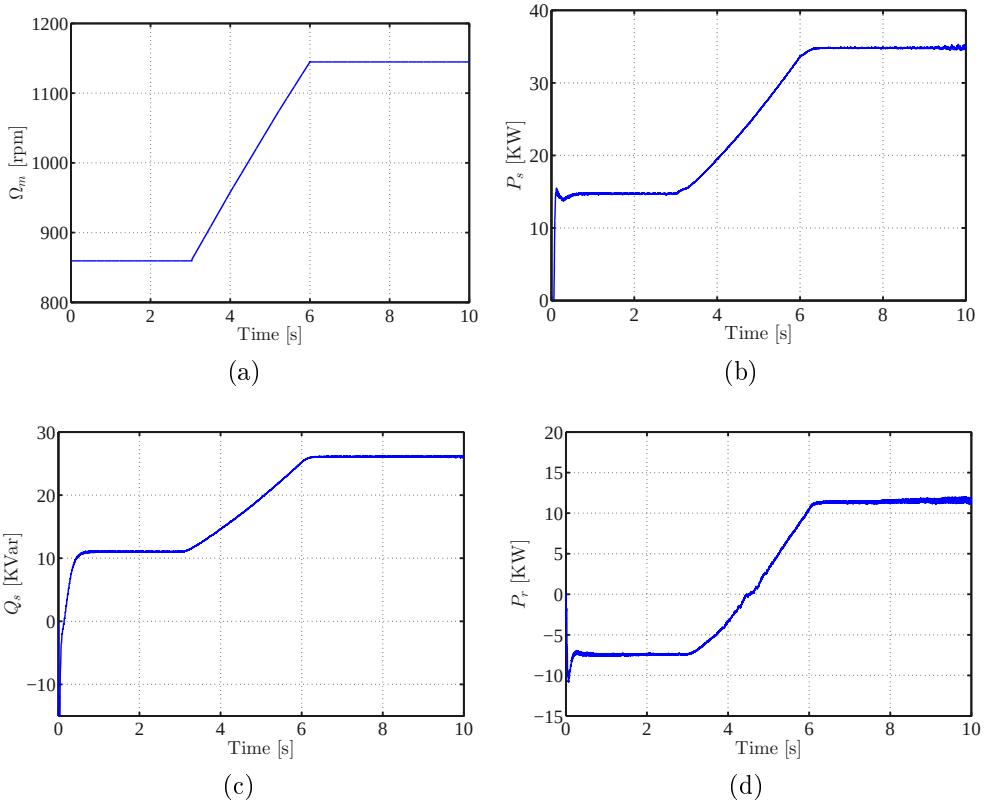

Figure 4.18: Test of WECS under steady wind speed change: (a) Mechanical shaft speed; (b) stator active power; (c) stator reactive power; and, (d) rotor active power.

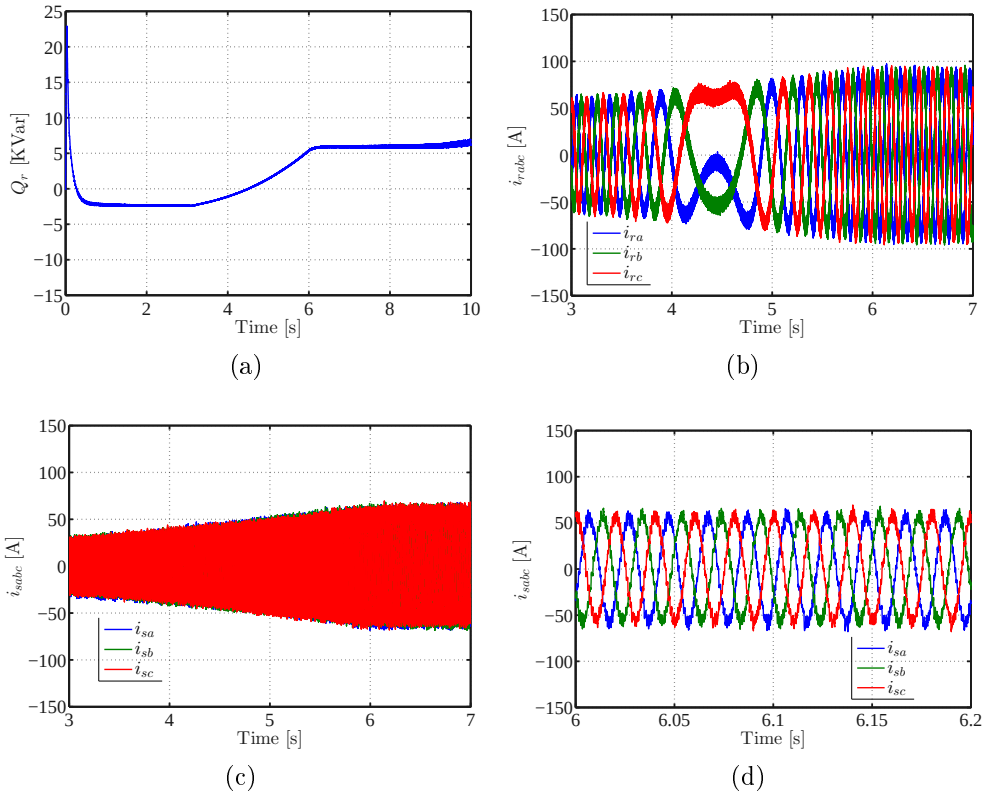

Figure 4.19: Testing of the WECS under steady wind speed change: (a) reactive rotor power; (b) three-phase rotor current; (c) three-phase stator current; and, (d) three-phase stator current.

transient patterns of the generated stator active and reactive powers lead to a surge of the stator power factor before it settles at a steady-state value of $\cos\phi = 0.8$ (lagging), as shown in Figure 4.17(b). After the transient period, the generated active power and reactive powers are 15.5 kW and 11.6 KVar, respectively. On the rotor side, the active and reactive powers consumed by the DFIG are -7.5 KW and -2.5 KW. Between $t = 3$ s and $t = 6$ s, the wind speed varies from 7.6 m/s to 10.2 m/s. The WECS operates from sub-synchronous to super-synchronous operating conditions. During that period, the stator active and reactive powers increase since they are directly proportional to the wind speed as depicted in Figure 4.18(b) and Figure 4.18(c). Similar patterns are observed from Figure 4.18(d) and Figure 4.19(a) as the rotor active and reactive powers are portions of the stator active and reactive powers, respectively. In addition, one can see from Figure 4.19(b) that the rotor current frequency slows down around the synchronous speed as the slip eventually becomes zero and picks up again after the synchronous speed ($\Omega_m = 1000$ rpm). In addition, both three-phase rotor and stator current envelops increase since the power generated by the DFIG increases due to the rise in wind speed, as shown in Figure 4.19(b) and Figure 4.19(c). The zoom on the three-phase sta-

tor current is displayed in Figure 4.19(d) where it can be seen that it pulsates at 50 Hz.

At a wind speed of 10.2 m/s, the DFIG operates under super-synchronous operating conditions. The corresponding mechanical shaft speed of the generator is at 1150 rpm. At this speed (Ω_m =1150 rpm), the DFIG generates powers at the stator and rotor sides as can be seen from Figures 4.18(b)-(d) and Figure 4.19(a). In addition, the stator active and reactive power generated by the DFIG are 35 KW and 26.2 KVar, respectively. On the other hand, the rotor active and reactive powers generated by the DFIG are 10.2 KW and 6 KVar, respectively.

4.5.2 Performance of the WECS based on DFIG under Change in Stator Power Factor

The performance of the WECS under change in stator power factor with steady wind speed is depicted in Figure 4.20. Between $t = 0$ s and $t = 5$ s, the

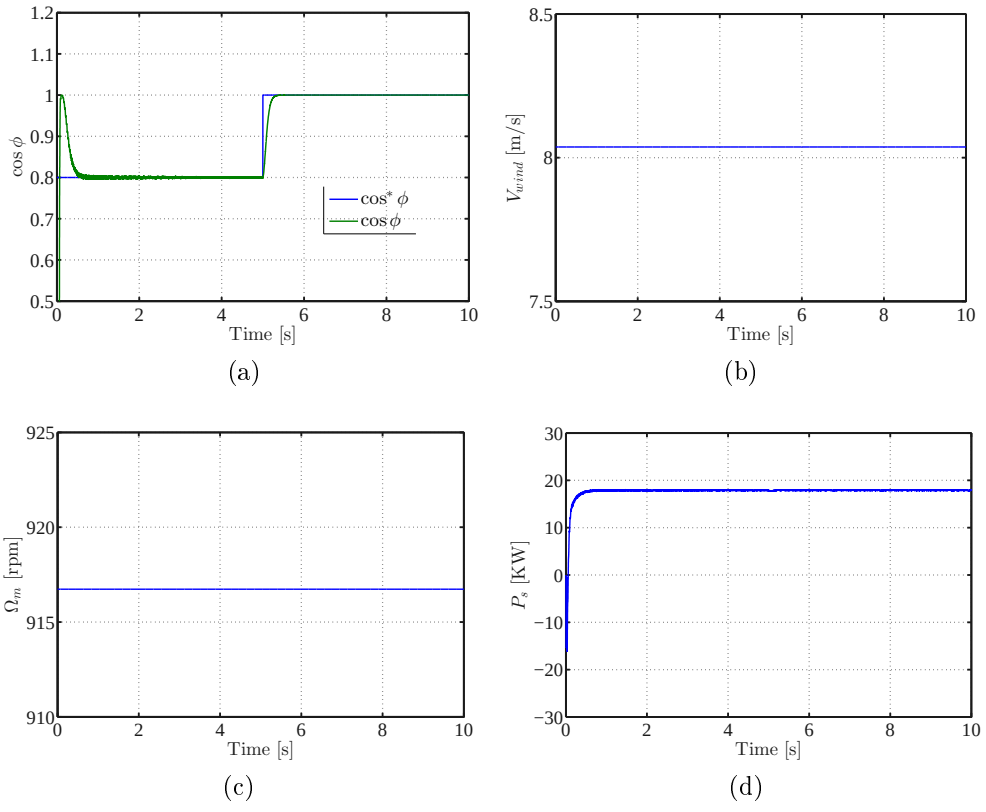

Figure 4.20: Test of the WECS under steady wind speed change: (a) mechanical shaft speed; (b) stator active power; (c) stator reactive power; and, (d) rotor active power.

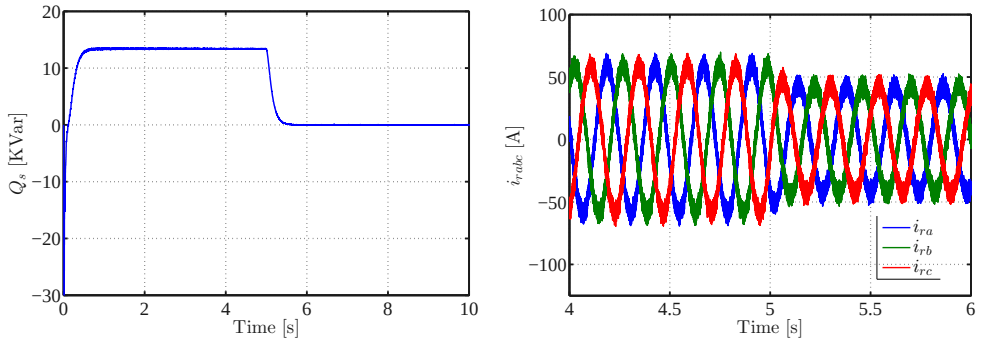

(a) (b)

Figure 4.21: Test of WECS under steady wind speed change: (a) Reactive power; and, (b) three-phase rotor current.

DFIG operates with a reference power factor of 0.8 (lagging), as shown in Figure 4.20(a). After a few cycles, the measured stator power factor settles to the reference stator power factor value, as shown in Figure 4.20(a). During the test, the WECS operates with a wind speed of 8.2 m/s, as shown in Figure 4.20(b). At this speed, the stator active and reactive powers are 18 KW and 13.5 KVar, as depicted in Figure 4.20(d) and Figure 4.21(a) while the DFIG consumes power from the rotor side as depicted in Figure 4.22. The three-phase rotor current pulsates at a constant slip frequency of 4.15 Hz since the mechanical shaft speed of the DFIG is constant, as displayed in Figure 4.21(b).

At $t = 5$ s, there is a step change in reference stator power factor (from $\cos^* \phi = 0.8$ to $\cos^* \phi = 1$). The measured stator power factor settles to the reference stator power factor after a few cycles, as displayed in Fig. 4.20(a). The generated stator power remains constant, since it depends exclusively on the wind speed. The generated stator reactive power settles to zero after a few

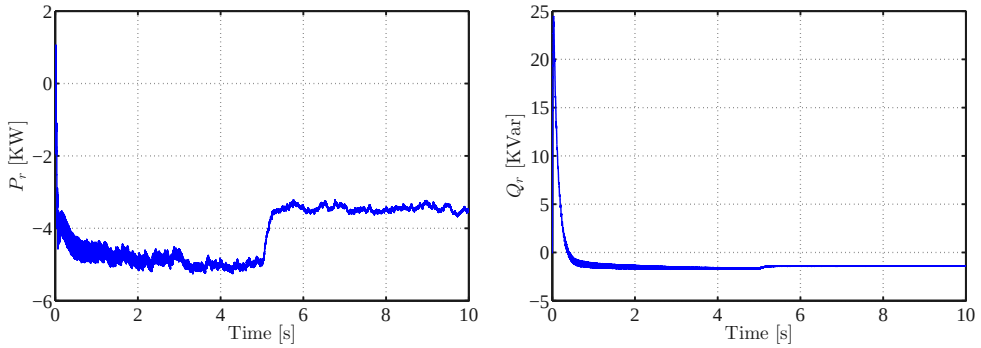

(a) (b)

Figure 4.22: Test of WECS under steady wind speed change: (a) reactive power; and, (b) three-phase rotor current.

cycles since the DFIG operates under unity power factor. As a consequence the three-phase current drops slightly at $t = 5$ s, as shown in Fig. 4.21(b). Further, the rotor active and reactive power reduces since the d-axis current is set to zero in order to achieve a unity power factor, as displayed in Figure 4.22(a) and Figure 4.22(b)

4.6 Conclusion

The control strategies of stand-alone and grid-connected WECS based on the DFIG were designed and implemented in MALAB/SIMULINK. It is shown that the performance of those control strategies under various operating conditions are satisfactory. In grid-connected mode, the power regulation and that of the unity power factor were satisfactory. In stand-alone mode, the voltage and frequency stability was guaranteed under various operating conditions.

Chapter 5

Laboratory Experiments of the Grid-Connected RSC

5.1 Introduction

In this chapter, the DFIG test bench is described. Further, the inner controller of the control strategy discussed in Section 4.3 is implemented. It is worth noticing that all modules of the control system discussed in Section 4.3, have been coded from scratch in LabVIEW. Furthermore, the performance of the inner current control under various operating conditions is investigated.

5.2 DFIG Test Bench Description

The DFIG test bench is composed of the 18.5 KW DFIG directly coupled to a 22 KW induction machine as depicted in Figure 5.1. The 22 KW induction machine helps in emulating the wind turbine. An encoder is fixed on the shaft of the 22KW induction machine. A torque sensor is mounted on the 22 KW induction machine, as depicted in Figure 5.1. The test bench is also composed of two VSCs connected in back-to-back configuration as shown in Figure 5.2. Also, these are the rotor-side converter and the grid-side converter, as shown in Figure 5.2. Each VSC includes IGBT power switches and their associated protections, the current sensors, the DC-link voltage sensor and a three-phase diode rectifier. The AC side of the rotor-side converter is directly connected to the rotor windings of the DFIG whilst the stator windings of the DFIG is connected to the point of common coupling. The AC side of the grid-side converter is connected to the grid through an L filter in order to mitigate the harmonics generated by the switching elements of the grid-side converter. The design of the physical L filter is discussed in Appendix C.

The basis of the DFIG test bench is the National Instrument (NI) PXIe-8115 embedded real-time controller. Two FPGA expansion modules are used

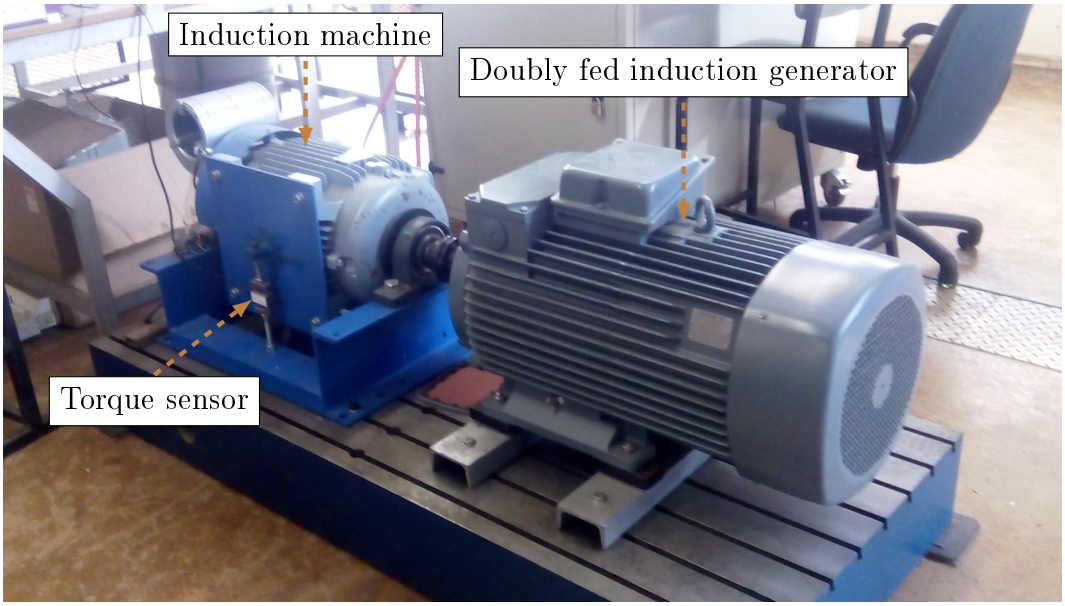

Figure 5.1: Picture of test bench with the Induction machine and DFIG

to input and output signals into or from the real time controller. These signals are the measurements (encoder measurement, torque sensor, current sensors, DC-link voltage sensors and grid voltage sensors) and the PWM signals. The host PC monitor is used for the development of the virtual instruments (VIs) that are executed on the PXIe-8115 embedded real-time controller. A picture of the host PC monitor is displayed in Figure 5.2. The user codes for the control purposes are written and compiled using LabVIEW. LabVIEW is a platform

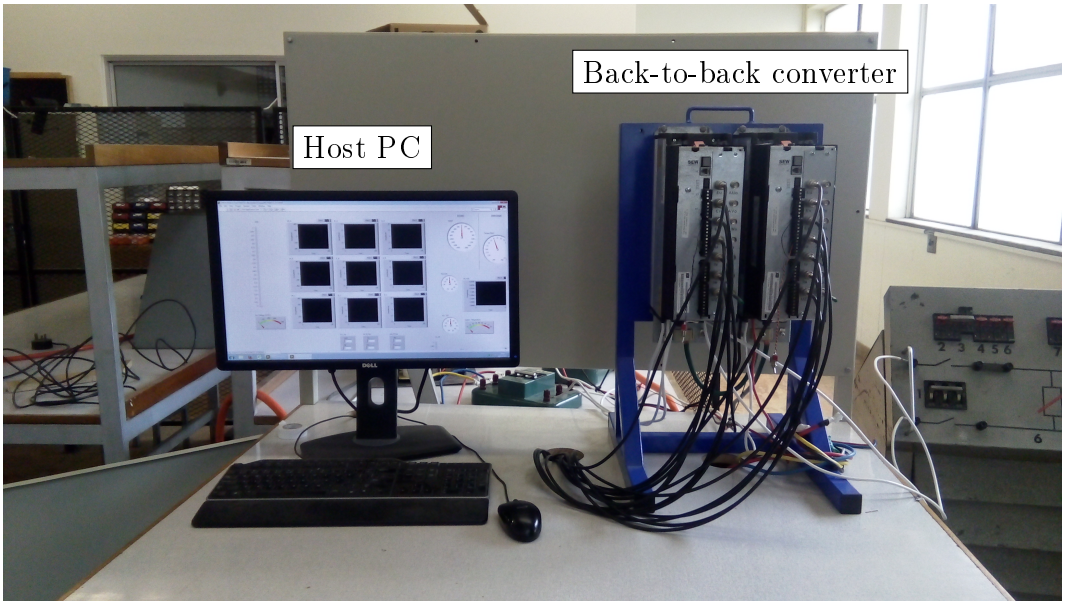

Figure 5.2: Picture of test bench

for the development of the software for the (NI) PXIe-8115 controller. The user codes are added to the main VI as subVIs. LabVIEW figures showing the control strategy are given in Appendix D.

5.3 Experimental Test of the RSC

The test set-up of the conducted experimental test is depicted in Figure 5.3. It can be seen that the grid is directly connected to a three-phase diode rectifier. The presence of the three-phase diode rectifier implies a unidirectional power flow from the grid to the rotor side of the DFIG. Therefore, in this experiment only the sub-synchronous mode and the synchronous operating conditions are described. The DC side of the three-phase diode rectifier is connected to the VSC through the DC-link capacitor of 500 μF.

On the other hand, the induction machine is connected to a variable frequency AC drive, as depicted in Figure 5.3. The speed of the induction machine is regulated through the AC drive. The stator of the DFIG is connected to a three-phase variable-source through a switch, as depicted in Figure 5.3. By default this switch is open. It is closed only when the synchronisation conditions are fulfilled.

The needed measurements for the control algorithm are the three-phase

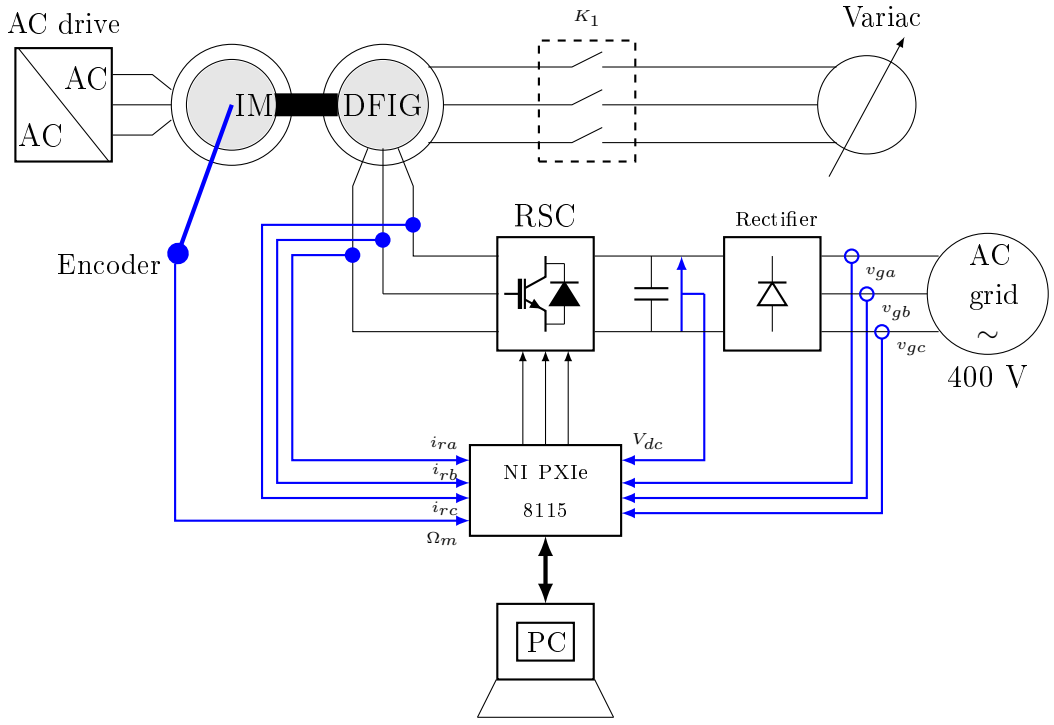

Figure 5.3: Schematic of the RSC set-up

grid voltage measurement; the three-phase rotor current measurement, the mechanical shaft speed measurement and the DC-link voltage measurement. The locations of these sensors are depicted in Figure 5.3. All the measurements are inputted to the PXIe-8115 controller, as depicted in Figure 5.3.

5.3.1 Measured Rotor, Grid and Slip Angles

In vector control, the angle of the synchronous reference frame is of all importance. The PLL is used in the calculation of the grid voltage angle. The three-phase diode rectifier is connected directly to the grid. The implementation of the PLL is discussed in Section 3.3 and its implementation in LabVIEW is depicted in Appendix D. The measured line-to-line three-phase grid voltage is shown in Figure 5.4(a). It can be seen that this line-to-line three-phase grid voltage pulsates at 50 Hz. The line-to-neutral voltage angle (θ_v) is determined by

$$\theta_v = \theta_{ll} - \frac{\pi}{6} \tag{5.1}$$

where θ_{ll} is the line-to-line voltage angle. The line-to-line grid voltage angle and the line-to-neutral grid voltage angles are shown in Figure 5.4(b). From Figure 5.4(b), it can be seen that the line-to-line grid voltage angle is lagging compared to the line-to-neutral grid voltage angle. Also, one can see that those two angles are pulsating at a frequency of about 50 Hz. In the control strategy proposed in Section 4.3, the q-axis of the synchronous dq0-reference frame is aligned along the grid voltage grid space vector. The line-to-neutral grid voltage angle calculated by the PLL assumes the alignment along the d-axis dq0-reference frame along the grid voltage space vector. Hence, the synchronous angle (θ_s) is given by

$$\theta_s = \theta_v + \frac{\pi}{2} \tag{5.2}$$

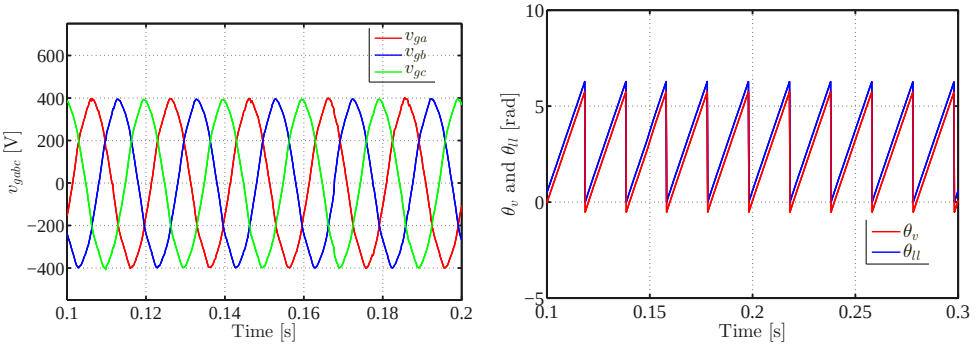

(a) (b)

Figure 5.4: Performances of the implemented PLL: (a) three-phase grid voltage; and, (b) line-to-line voltage and line-to-phase voltage angles.

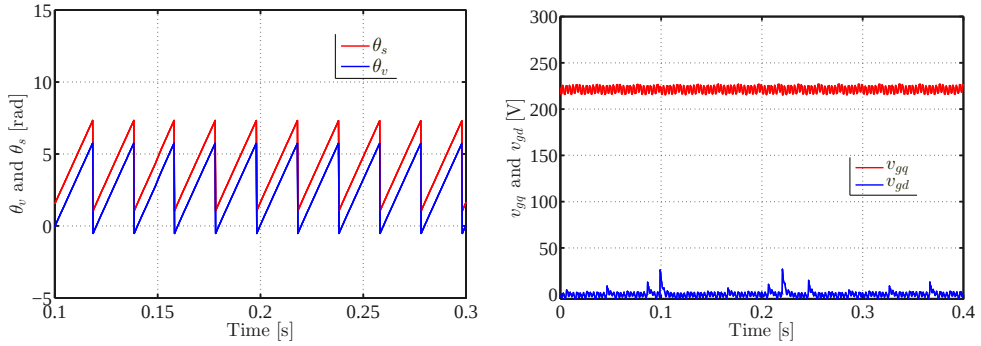

(a) (b)

Figure 5.5: Performances of the implemented PLL: (a) Line-to-phase voltage and synchronous angles; and, (b) d-axis and q-axis grid voltages.

The synchronous angle and the line-to-neutral voltage are shown in Figure 5.5(a). The d-axis and q-axis grid voltages are presented in Figure 5.5(b). It can be seen that the q-axis grid voltage is about 220 V and the d-axis grid voltage is zero. This shows that the implemented PLL works perfectly.

On the other hand, when the DFIG is run at synchronous speed the measured mechanical shaft speed is presented in Figure 5.6(a). It can be seen from Figure 5.6(a) that the measured mechanical shaft speed is not properly measured by the encoder. Hence, there is a need of filtering the measured mechanical shaft speed. The measured DC-link voltage is shown in Figure 5.6(b).

Consider the transfer function of a first order filter as given below;

$$\frac{y(p)}{u(p)} = \frac{1}{1 + pT_f}, \tag{5.3}$$

where $y(p)$ and $u(p)$ are the output and input of the filter; T_f is the filter time

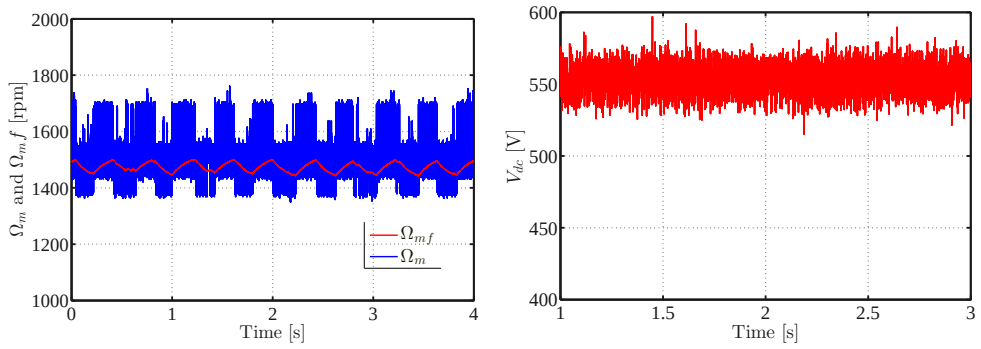

(a) (b)

Figure 5.6: Measurement from the test bench: (a) Mechanical shaft speed and filtered mechanical shaft speed; and, (b) measured DC-link voltage.

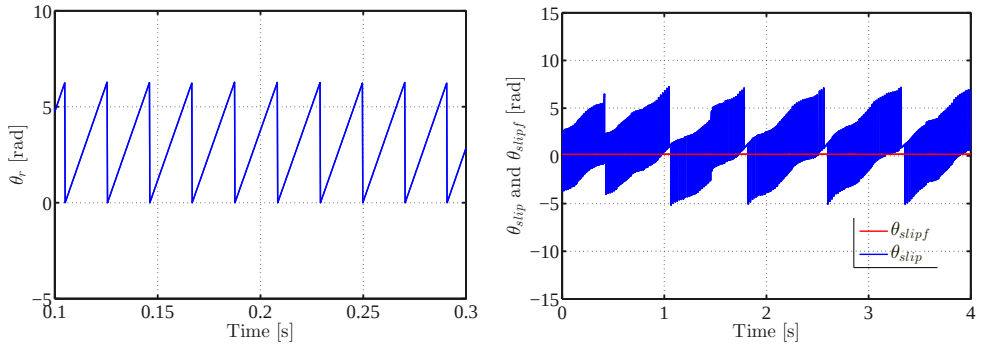

(a) (b)

Figure 5.7: Performances of the slip angle and rotor angle modules: (a) rotor angle; and, (b) slip angle and filtered slip angle.

constant. Rewriting Equation (5.3) in terms of time and using the backward Euler theorem yields

$$y_k = ay_{k-1} + bu_k, \tag{5.4}$$

where y_k and u_k are the input and output of the filter at time t_k; y_{k-1} is the output of the filter at t_{k-1}; and,$a = \frac{T_f}{T_f+T_s}$ and $b = \frac{1}{T_f+T_s}$. The implementation of the filter in LabVIEW is straightforward by using a shift register in a while loop. The time constant is determined by choosing the cut-off frequency. The filtered mechanical shaft speed is shown in Figure 5.6(a). It can be seen that even the filtered mechanical shaft speed still fluctuates. Hence, during synchronous operating conditions it is necessary to filter the slip angle due to the fact that the slip angle depends on both the synchronous angle and the electrical rotor angle which in turn depends on the mechanical shaft speed.

The expression of the electrical rotor angle is given by

$$\theta_r = \int_0^t \omega_r dt, \tag{5.5}$$

By discretising the expression in Equation (5.5) using the backward Euler theorem yields

$$\theta_{rk} = \theta_{rk-1} + T_s\omega_r, \tag{5.6}$$

where θ_{rk} and θ_{rk-1} are the electrical rotor angle at time t_k and t_{k-1}, respectively. Again, in LabVIEW, the implementation of such an expression is done using a shift register in a while loop.

The expressions of the rotor angle and that of slip angle presented in Figure 5.7(a) and Figure 5.7(b) were calculated when the DFIG was running at nearly synchronous speed. It can be seen that the electrical rotor angle pulsates at about 50 Hz, as depicted in Figure 5.7(a).

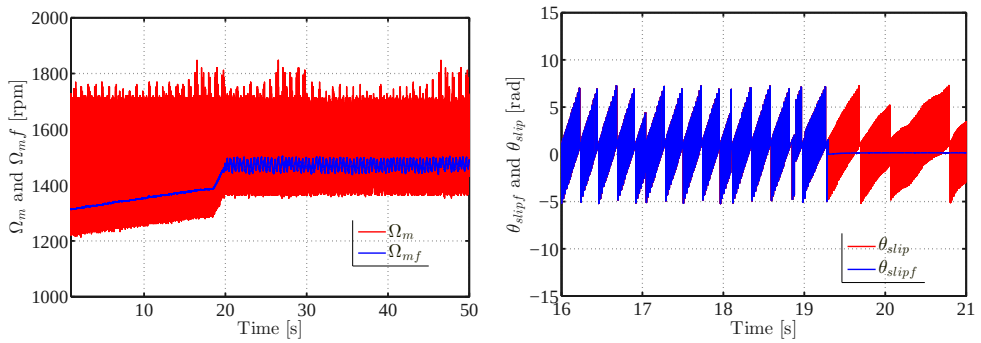

(a) (b)

Figure 5.8: Transient Performances of the filter modules: (a) filtered and measured mechanical shaft speeds; and, (b) slip angle and filtered slip angle.

The performance of the implemented filters (for the mechanical shaft speed and that of the slip angle) during change in mechanical shaft speed are shown in Figure 5.8(a) and Figure 5.8(b). Both figures were obtained by varying the mechanical shaft speed from 1350 rpm to 1500 rpm. From Figure 5.8(a), It can be seen that the measured mechanical shaft speed fluctuates more at a speed of 1500 rpm leading to the fluctuation of the filtered mechanical shaft. On the other hand, the filter of the slip angle was designed to be activated only when the DFIG is about to operate under synchronous operating conditions. At about t=19.5 s, This special feature of the filter of the slip angle is shown in Figure 5.8(b).

5.3.2 Testing of the inner rotor current control during synchronous operating conditions

The DFIG parameters were determined in order to design the PI parameters of the control system. The determination of the DFIG parameters is discussed in Appendix B. The implementation of the PI in LabVIEW is discussed in Appendix A. The PI parameters of the inner controller are displayed in Table 5.1. The testing of the set-up displayed in Figure 5.3 is conducted when the DFIG system is not connected to the grid.

Table 5.1: Inner PI parameters

Inner rotor current PI controller	values
K_{rcp}	7.49
K_{rci}	399.6

Figure 5.9 and Figure 5.10 were obtained by running the DFIG at synchronous speed and adjusting the reference d-axis and q-axis rotor currents,

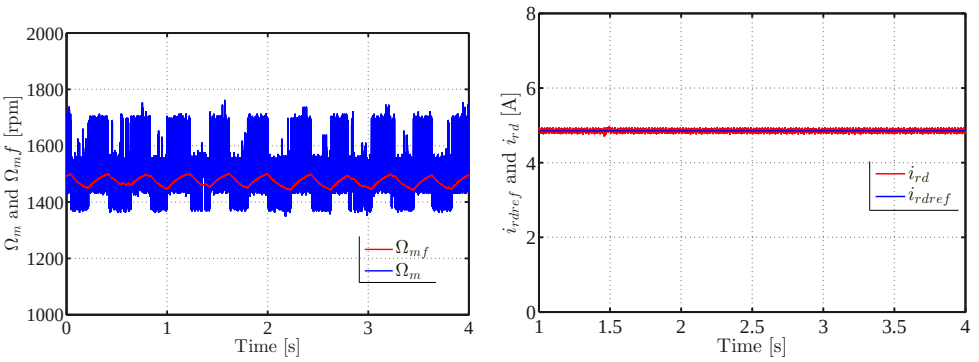

(a) (b)

Figure 5.9: Testing under synchronous operating conditions: (a) filtered and measured mechanical shaft speeds; and, (b) reference and measured d-axis rotor currents.

as presented in Figure 5.9(b) and Figure 5.10(a). The mechanical shaft speed used in the control system is the filtered mechanical shaft speed, as presented in Figure 5.9(a). The d-axis and q-axis rotor currents were adjusted to 4.8 A and 0 A respectively, as can be seen in Figure 5.9(b) and Figure 5.10(a). The adjustment aims at reaching a line-to-line stator voltage of 150 V. The three-phase rotor current is presented in Figure 5.10(b). It can be seen that the three-phase rotor current pulsates at a slip frequency of 0 Hz. This confirms the theory concerning the three-phase rotor current of the DFIG under synchronous operating conditions. Exciting the rotor windings with the d-axis and q-axis rotor currents presented in Figure 5.9(b) and Figure 5.10(a) induces a three-phase stator voltage, as shown in Figure 5.11.

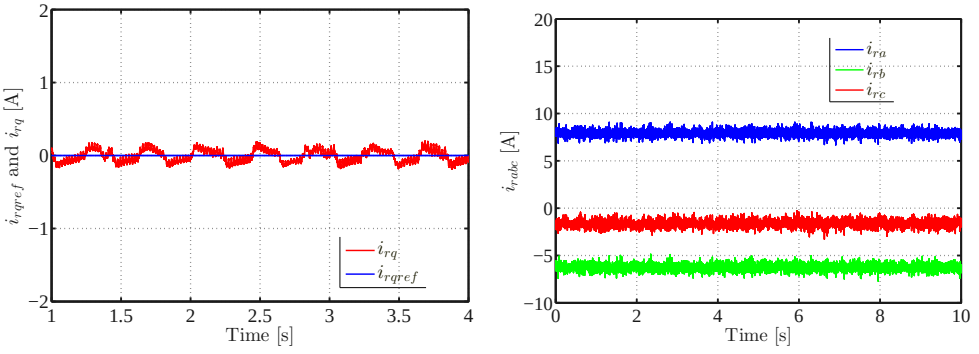

(a) (b)

Figure 5.10: Testing under synchronous operating conditions: (a) reference and measured q-axis rotor currents; and, (b) three-phase rotor current.

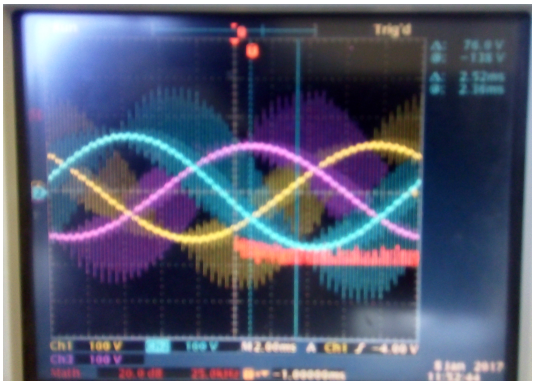

Figure 5.11: Three-phase stator voltage

5.3.3 Testing of the inner current control during sub-synchronous operating conditions

Figure 5.12 and Figure 5.13 were obtained by running the DFIG at about 1350 rpm, as depicted in Figure 5.12(b); and by setting the d-axis current and q-axis current to 4.8 A and 0 A, as shown in Figure 5.12(a). In addition, one can see from Figure 5.12(b) and Figure 5.13(a) that the control system shows good performances when it comes to tracking the d-axis and q-axis rotor currents. Further, a closer look at Figure 5.13(b), one can see that the frequency of the three-phase rotor current correspond to that of the slip frequency ($f_{slip} = 5\,\text{Hz}$). The three-phase rotor current pulsates at a slip frequency of 5 Hz. This confirms the theory about the rotor current that suggests that the three-phase rotor current in a DFIG should pulsate at slip frequency.

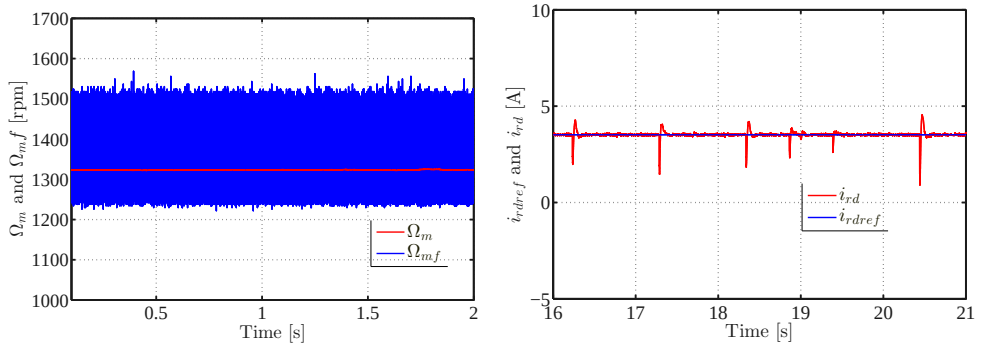

(a) (b)

Figure 5.12: Testing under sub-synchronous operating conditions: (a) filtered and measured mechanical shaft speeds; and, (b) reference and measured d-axis rotor currents.

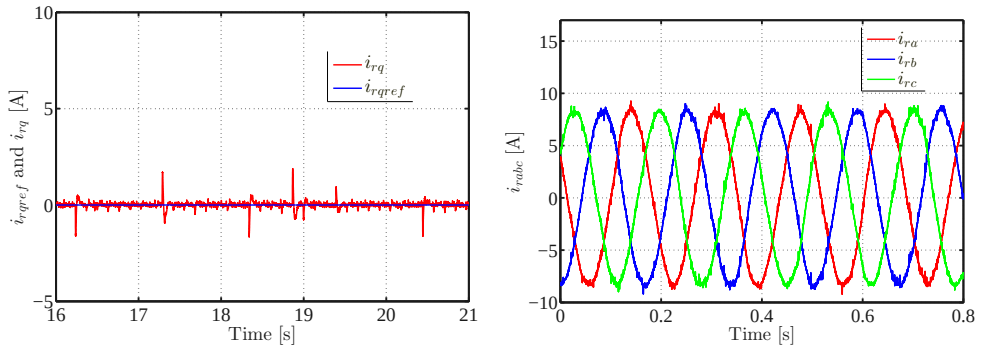

(a) (b)

Figure 5.13: Testing under sub-synchronous operating conditions: (a) reference and measured q-axis rotor currents ; and, (b) three-phase rotor current.

5.3.4 Testing of the inner current control during change in mechanical wind speed

Figure 5.14 and Figure 5.15 were obtained by steadily varying the mechanical shaft speed from 1350 rpm to 1500 rpm together with the d-axis and q-axis rotor currents set at 2.4 A and 0 A, as presented in Figure 5.14(a) and Figure 5.15(b). From Figure 5.14(a), it can be seen that the DFIG reached the synchronous speed at about 19.5 s. It can be seen from Figure 5.14(a) and Figure 5.15(b) that the inner rotor current control helps in tracking the reference d-axis and q-axis rotor currents set by the user.

On the other hand, the three-phase rotor current is shown in Figure 5.15(b). It can be seen from Figure 5.15(b) that as the mechanical shaft speed approaches the synchronous speed, the three-phase rotor current slows down. Furthermore, at about t=19.4 s, the DFIG runs at about the synchronous

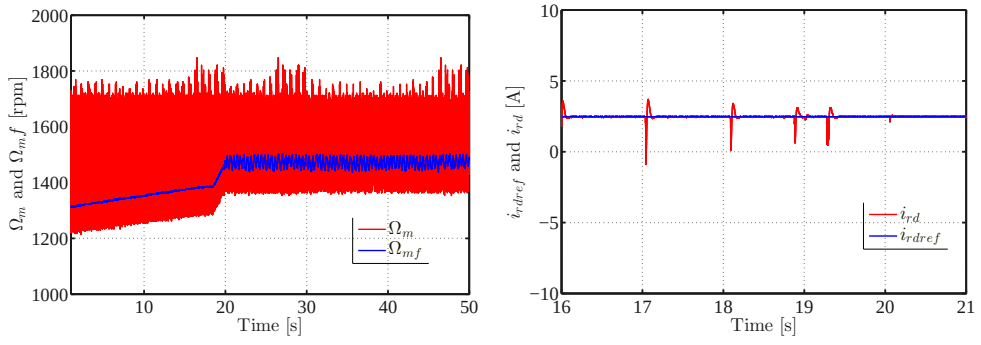

(a) (b)

Figure 5.14: Performances of the inner rotor controller modules: (a) filtered and measured mechanical shaft speeds; and, (a) reference and measured d-axis rotor currents.

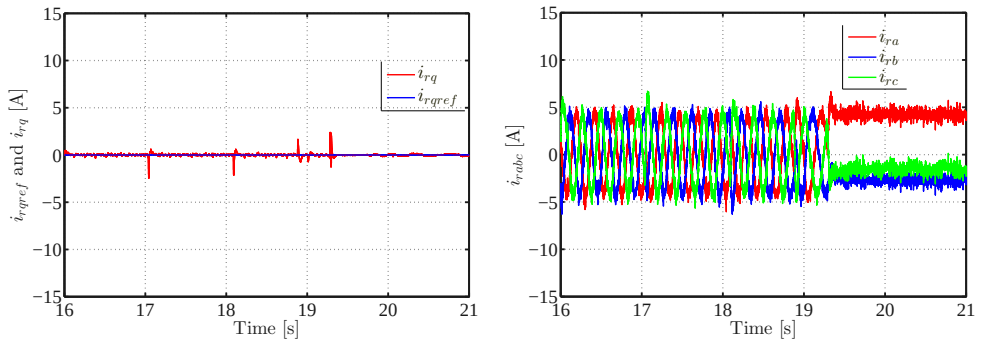

(a) (b)

Figure 5.15: Transient Performances of inner rotor controller modules: (a) Reference and measured q-axis rotor currents; and, (b) three-phase rotor current.

speed which means that the slip frequency is nearly zero. This also means that the three-phase rotor current is a DC signal, as shown in Figure 5.15(b).

5.4 Conclusion

A brief overview on the test bench was given in this chapter. In addition, the performance of the inner rotor current despite that the measurement of the encoder needed filtering was investigated. The implemented inner rotor controller shows satisfactory performance. It is shown that the d-axis and q-axis rotor currents are DC signals which means that there is a correct tracking of the rotor angle. The inner current control helps for a soft connection to the grid by the adjustment of the d-axis and q-axis rotor current as seen in this chapter.

Chapter 6

Conclusion and Future Recommendations

6.1 Conclusion

Based on the findings in this thesis, the following conclusions can be drawn;

- The modelling of the the whole wind energy conversion system based on the DFIG (DFIG, back-to-back converter, filter, wind turbine) was presented. It was found that the DFIG model built in MATLAB/SIMULINK showed satisfactory performances during free acceleration.
- The design of the LCL filter for switching frequencies lower than 5000 Hz was conducted. Further, a comparative study of the LCL filter and L filter in grid-connected VSC was also conducted based on some effectiveness factors. It was shown that even for switching frequencies lower than 5000 Hz, the LCL filter outperformed the L filer. And, the grid-connected VSC complied with the required THD of 8 %.
- A control strategy of the grid-side converter based on the L approximation of the LCL filter was developed, then implemented in MATLAB/SIMULINK. The performances of the proposed control strategy were verified under various operating conditions. It was found that the control algorithm showed satisfactory performances during change in grid voltage amplitude and during full load operating conditions.
- A control strategy of the stand-alone DFIG system in wind turbine applications aiming at the voltage and frequency stability was developed then implemented in MATLAB/SIMULINK. The performances of the proposed control strategy in stand-alone WECS based on the DFIG was verified through simulations under various operating conditions. It was shown that the developed control strategy showed good performances.

- A control strategy of the grid-connected WECS based on the DFIG system was developed. The aims of this control strategy are the stator power regulation and that of stator power factor. Further, the stator power regulation is done without measuring the three-phase stator current. The performances of the developed control strategy were investigated under change in speed and change in stator power factor. It was shown that the developed control strategy showed good performances.
- The inner current controller of the proposed control strategy on grid-connected WECS based on the DFIG was implemented in the laboratory using LabVIEW. Through various operating conditions, it was shown that the implemented inner current controller showed good performances.

6.2 Future Recommendations

There are many aspects of the control of WECS based on the DFIG that can be further investigated. However, a few recommendations are as follows;

- The design of a physical LCL filter would improve the power quality of the voltage and current generated by the DFIG.
- An encoder-less vector control can be investigated since the signal measured by the encoder needs to be filtered. This has the advantage consisting to avoid the dependency of the control system on the measured mechanical shaft speed or the measured rotor angle.
- The design of the sensors for the three-phase stator voltage and the three-phase stator current would provide many options in terms of the control methods to be investigated on the test bench.

References

[1] R. Swisher, C. R. De Azua, and J. Clendenin, "Strong winds on the horizon: Wind power comes of age," *Proceedings of the IEEE*, vol. 89, no. 12, pp. 1757–1764, 2001.

[2] "Market forecast for 2016-2020," 2016 (accessed November 7, 2016). [Online]. Available: http://www.gwec.net/publications/global-wind-energy-outlook/global-wind-energy-outlook-2016/

[3] "South african energy sector," 2014 (accessed December 31, 2016). [Online]. Available: https://www.usea.org/sites/default/files/event-file/497/South_Africa_Country_Presentation.pdf

[4] "Global wind energy outlook," 2014 (accessed November 3, 2016). [Online]. Available: http://gwec.net/wp-content/uploads/2014/10/GWEO2014.pdf/

[5] H. Polinder, J. A. Ferreira, B. B. Jensen, A. B. Abrahamsen, K. Atallah, and R. A. McMahon, "Trends in wind turbine generator systems," *IEEE Journal of Emerging and Selected Topics in Power Electronics*, vol. 1, no. 3, pp. 174–185, 2013.

[6] M. Tazil, V. Kumar, R. Bansal, S. Kong, Z. Dong, and W. Freitas, "Three-phase doubly fed induction generators: an overview," *IET Electric Power Applications*, vol. 4, no. 2, p. 75, 2010.

[7] R. Cardenas, R. Pena, S. Alepuz, and G. Asher, "Overview of Control Systems for the Operation of DFIGs in Wind Energy Applications," *IEEE Transactions on Industrial Electronics*, vol. 60, no. 7, pp. 2776–2798, 2013.

[8] R. S. Pena, G. M. Ahser, J. C. Clare, and R. Cardenas, "A constant frequency constant voltage variable speed stand alone wound rotor induction generator," in *International Conference on Opportunities and Advances in International Power Generation*, vol. 1996, no. 419, 1996, pp. 111–114.

[9] M. Sleiman, B. Kedjar, A. Hamadi, K. Al-Haddad, and H. Y. Kanaan, "Modeling, control and simulation of DFIG for maximum power point tracking," *2013 9th Asian Control Conference (ASCC)*, vol. 8, no. 3, pp. 1–6, 2013.

[10] A. Khambadkone, R. D. R. Datta, and V. Ranganathan, "Modeling and rotor current control of doubly-fed induction machine with complex signal flow graphs," *1998 International Conference on Power Electronic Drives and Energy Systems for Industrial Growth, 1998. Proceedings.*, vol. 2, no. 3, pp. 972–977, 1998.

[11] Y. Lei, A. Mullane, G. Lightbody, and R. Yacamini, "Modeling of the wind turbine with a doubly fed induction generator for grid integration studies," *IEEE Transactions on Energy Conversion*, vol. 21, no. 1, pp. 257–264, 2006.

[12] S. Chondrogiannis and M. Barnes, "Stability of doubly-fed induction generator under stator voltage oriented vector control," *IET Renewale Power Generation*, vol. 2, no. 1, pp. 170–180, 2008.

[13] B. Shen, B. Mwinyiwiwa, Y. Zhang, and B. T. Ooi, "Sensorless maximum power point tracking of wind by DFIG using rotor position phase lock loop (PLL)," *IEEE Transactions on Power Electronics*, vol. 24, no. 4, pp. 942–951, 2009.

[14] N. K. Swami Naidu and B. Singh, "Sensorless control of single voltage source converter-based doubly fed induction generator for variable speed wind energy conversion system," *IET Power Electronics*, vol. 7, no. 12, pp. 2996–3006, 2014.

[15] J. Hu, J. Zhu, D. G. Dorrell, Q. Ma, Y. Zhang, and W. Xu, "Control strategies of variable-speed wind system under new grid code requirement-A survey," in *IECON Proceedings (Industrial Electronics Conference)*, vol. 2, 2010, pp. 3061–3066.

[16] C. D. Cho, S. R. Nam, S. H. Kang, and S. J. Ahn, "Modeling of DFIG wind turbines considering fault-ride-through grid code," in *APAP 2011 - Proceedings: 2011 International Conference on Advanced Power System Automation and Protection*, vol. 2, 2011, pp. 1024–1028.

[17] A. Tapia, G. Tapia, J. Ostolaza, and J. Saenz, "Modeling and control of a wind turbine driven doubly fed induction generator," *IEEE Transactions on Energy Conversion*, vol. 18, no. 2, pp. 194–204, 2003.

[18] V. Blasko and V. Kaura, "A new mathematical model and control of a three-phase AC-DC voltage source converter," *IEEE Transactions on Power Electronics*, vol. 12, no. 1, pp. 116–123, 1997.

[19] L. Shuhui and T. A. Haskew, "Analysis of decoupled d-q vector control in DFIG back-to-back PWM converter," in *2007 IEEE Power Engineering Society General Meeting, PES*, 2007, pp. 1–7.

[20] R. Pena, J. Clare, and G. Asher, "A doubly fed induction generator using back-to-back PWM converters supplying an isolated load from a variable speed wind turbine," *IEE Proceedings - Electric Power Applications*, vol. 143, no. 5, pp. 380–387, 1996.

[21] M. Noroozi and S. Farhangi, "Voltage and frequency stability for control of stand-alone DFIG-based wind turbine using direct voltage control method," in *2014 14th International Conference on Environment and Electrical Engineering*, 2014, pp. 85–90.

[22] M. Aktarujjaman, M. A. Kashem, M. Negnevitsky, and G. Ledwich, "Control stabilisation of an islanded system with DFIG wind turbine," in *First International Power and Energy Conference, (PECon 2006) Proceedings*, no. PECon, 2006, pp. 312–317.

[23] Y. Zhang and B. T. Ooi, "Stand-Alone doubly-fed induction generators (DFIGs) with autonomous frequency control," *IEEE Transactions on Power Delivery*, vol. 28, no. 2, pp. 752–760, 2013.

[24] G. Iwanski and W. Koczara, "Extended direct voltage control of the stand-alone double fed induction generator," in *POWERENG 2007 - International Conference on Power Engineering - Energy and Electrical Drives Proceedings*, 2007, pp. 754–759.

[25] A. K. Jain and V. T. Ranganathan, "Wound rotor induction generator with sensorless control and integrated active filter for feeding nonlinear loads in a stand-alone grid," *IEEE Transactions on Industrial Electronics*, vol. 55, no. 1, pp. 218–228, 2008.

[26] N. K. S. Naidu and B. Singh, "Experimental Implementation of Doubly Fed Induction Generator Based Standalone Wind Energy Conversion System," *IEEE Transactions on Industry Applications*, vol. 52, no. 4, pp. 3332–3339, 2014.

[27] M. Liserre, F. Blaabjerg, and S. Hansen, "Design and control of an LCL-filter-based three-phase active rectifier," *IEEE Transactions on Industry Applications*, vol. 41, no. 5, pp. 1281–1291, 2005.

[28] S. Piasecki, R. Szmurlo, and M. Jasinski, "Design of AC-DC Grid Connected Converter using Multi-Objective Optimization," *Electrical, Control and Communication Engineering*, vol. 5, no. 1, pp. 11–19, 2014.

[29] S. Sen, K. Yenduri, and P. Sensarma, "Step-by-step design and control of LCL filter based three phase grid-connected inverter," *2014 IEEE International Conference on Industrial Technology, ICIT 2014*, pp. 503–508, 2014.

[30] K. Jalili and S. Bernet, "Design of LCL filters of active-front-end two-level voltage-source converters," *IEEE Transactions on Industrial Electronics*, vol. 56, no. 5, pp. 1674–1689, 2009.

[31] Z. Guohong, T. W. Rasmussen, and R. Teodorescu, "A novel optimized LCL-filter designing method for grid connected converter," in *2nd International Symposium on Power Electronics for Distributed Generation Systems, PEDG 2010*, vol. 2, no. c, 2010, pp. 802–805.

[32] F. Li, X. Zhang, H. Zhu, H. Li, and C. Yu, "An LCL-LC filter for grid-connected converter: Topology, parameter, and analysis," *IEEE Transactions on Power Electronics*, vol. 30, no. 9, pp. 5067–5077, 2015.

[33] M. Huang, F. Blaabjerg, Y. Yang, and W. Wu, "Step by step design of a high order power filter for three-phase three-wire grid-connected inverter in renewable energy system," in *2013 4th IEEE International Symposium on Power Electronics for Distributed Generation Systems, PEDG 2013 - Conference Proceedings*, 2013.

[34] R. Beres, X. Wang, M. Liserre, F. Blaabjerg, and C. L. Bak, "A Review of Passive Power Filters for Three-Phase Grid-Connected Voltage-Source Converters," *IEEE Journal of Emerging and Selected Topics in Power Electronics*, vol. 4, no. 1, pp. 54–69, 2016.

[35] Krause,C., Paul, O. Wasynczuk, and Sudhoff, D.,Scott, *Analysis of electric machinery*, ieee press ed., New York, 1995.

[36] G. Abad, *Doubly fed induction machine: modelling and control for wind energy generator applications*, ieee press ed., Hoboken,NJ, 2011.

[37] H. S. Kim and D. D.-C. Lu, "Review on wind turbine generators and power electronic converters with the grid-connection issues," *Australasian Universities Power Engineering Conference*, pp. 1–6, 2010.

[38] D. Yao and R. G. Harley, "Present and future trends in wind turbine generator designs," *Power Electronics and Machines in Wind Applications, IEEE. PEMWA 2009. Lincoln,NE,USA.*, no. 11, pp. 1–6, 2009.

[39] M. Liserre, R. Cárdenas, M. Molinas, and J. Rodríguez, "Overview of multi-MW wind turbines and wind parks," *IEEE Transactions on Industrial Electronics*, vol. 58, no. 4, pp. 1081–1095, 2011.

[40] H. Polinder, F. F. A. Van Der Pijl, G. J. De Vilder, and P. J. Tavner, "Comparison of direct-drive and geared generator concepts for wind turbines," *IEEE Transactions on Energy Conversion*, vol. 21, no. 3, pp. 725–733, 2005.

[41] J. Slootweg, S. de Haan, H. Polinder, and W. Kling, "General model for representing variable speed wind turbines in power system dynamics simulations," *IEEE Transactions on Power Systems*, vol. 18, no. 1, pp. 144–151, 2003.

[42] M. Liserre, A. D. Aquila, and P. Bari, "Step-by-Step Design Procedure for a Grid-Connected Three-Phase PWM Voltage Source Converter '," *International Journal of Electronics*, vol. 91, no. 8, pp. 445–460, 2004.

[43] R. Erikson and D. Masksimovic, *Fundamentals of Power Electronics*. Boston, MA, USA: Springer, 2001.

[44] F. Khatounian, E. Monmasson, F. Berthereau, and J. Louis, "Design of an output LC filter for a doubly fed induction generator supplying non-linear loads for aircraft applications," in *2004 IEEE International Symposium on Industrial Electronics*, vol. 2, no. l, 2004, pp. 1093–1098.

[45] V. Kaura and V. Blasko, "Operation of a phase locked loop system under distorted utility conditions," *IEEE Transactions on Industry Applications*, vol. 33, no. 1, pp. 58–63, 1997.

[46] H. C. Skudelny and G. V. Stanke, "Analysis and Realization of a Pulsewidth Modulator Based on Voltage Space Vectors," *IEEE Transactions on Industry Applications*, vol. 24, no. 1, pp. 142–150, 1988.

[47] V. Blasko and V. Kaura, "A novel control to actively damp resonance in input LC filter of a three-phase voltage source converter," *IEEE Transactions on Industry Applications*, vol. 33, no. 2, pp. 542–550, 1997.

Appendices

Appendix A

Lab Implementation of PI Controller

The PI current controller can be expressed by

$$PI(p) = \frac{1}{p}\begin{bmatrix} K_p p + K_i & 0 \\ 0 & K_p p + K_i \end{bmatrix}, \tag{A.1}$$

where K_p and K_i are the proportional and integral constants of the PI controller. The mathematical expression of the PI controller using state vector is given by

$$\dot{x}_c(t) = \begin{bmatrix} K_i & 0 \\ 0 & K_i \end{bmatrix} e(t), \tag{A.2}$$

where $e(t)$ is the error signal which is the difference between the output of the PI controller and the set value. Using Equation (A.2), the output of the PI controller is given by

$$u(t) = x_c(t) + \underbrace{\begin{bmatrix} K_p & 0 \\ 0 & K_p \end{bmatrix}}_{\boldsymbol{K_p}} e(t) + Wy(t), \tag{A.3}$$

where $u(t) = \begin{bmatrix} u_d(t) \\ u_q(t) \end{bmatrix}$ is the output of the PI controller; $x_c(t)$ is the state vector of the controller; $e(t) = r(t) - y(t)$ is the error signal of the PI controller; and, $Wy(t)$ is the compensation terms of the inner controller. Discretising Equation (A.3) and Equation (A.2) using the backward Euler theorem yields

$$x_{c,k} = x_{c,k-1} + T_s \underbrace{\begin{bmatrix} K_i & 0 \\ 0 & K_i \end{bmatrix}}_{\boldsymbol{K_i}} e_k \tag{A.4}$$

and

$$u_k = x_{c,k} + \underbrace{\begin{bmatrix} K_p & 0 \\ 0 & K_p \end{bmatrix}}_{\boldsymbol{K_p}} e_k + Wy_k, \tag{A.5}$$

where subscript k indicates the time instant and T_s is the sampling time at instant $t = kT_s$.

A.1 Anti Wind-up and Limitations

Since any system to be controlled has physical limitations such as the maximum current allowed, it is important to limit this current in the system. In order to avoid saturation when using PI controllers for the control of VSC, the outputs of the PI controller can be limited as expressed below;

$$\bar{u} = f(u) = \begin{cases} u, & |u| \leq |u|_{max} \\ u\frac{|u|_{max}}{|u|}, & |u| > |u|_{max} \end{cases}, \tag{A.6}$$

where $\bar{u}$ is the limited output of the PI controller. In Equation (A.6), only the magnitude of the output of the PI controller is limited while its angle can still vary.

However, limiting only the output of the PI controller leads to high overshoot when a disturbance occurs. This fact is called the wind-up phenomenon which has to be dealt with. The controller output limitation can be considered as expressed below;

$$\tilde{u} = \bar{u} - u, \tag{A.7}$$

where $\tilde{u}$ is the disturbance entering between the PI controller and the plant.

The above problems can be solved by using back-calculation method in the following way:

1. At a sampling instant k, compute the ideal output of the PI controller,

$$u_k = x_{c,k-1} + (T_s\boldsymbol{K_i} + \boldsymbol{K_p})e_k + Wy_k. \tag{A.8}$$

   and limit the output of the PI controller using $\bar{u} = f(u)$.

2. In order to avoid the above-mentioned problems, the limit of the output of the PI controller is moved to the controller input, it yields

$$\bar{e}_k = (T_s\boldsymbol{K_i} + \boldsymbol{K_p})^{-1}[\bar{u}_k - x_{c,k-1} - Wy_k], \tag{A.9}$$

   where $\bar{e}_k$ is the limited error. Then, $\bar{e}_k$ to update the controller state vector as shown below;

$$x_{c,k} = x_{c,k-1} + T_s\boldsymbol{K_i}(T_s\boldsymbol{K_i} + \boldsymbol{K_p})^{-1}[\bar{u}_k - x_{c,k-1} - Wy_k]. \tag{A.10}$$

Appendix B

System Parameters

B.1 Determination of DFIG Parameters

In order to determine the parameters of the three-phase, 400 V, 4 poles 18.5 kW DFIG to be used in the test bench, some tests were conducted. Those tests include the DC test, the No-load test and the locked rotor test. It is worth noticing that the rotor of the DFIG was short-circuited for all these tests. The simplified equivalent circuit of the DFIG is depicted in Figure B.1. The above-mentioned tests are discussed in the following sections.

B.1.1 DC Test

The DC test is performed so as to determine the DC resistance value of stator resistance. The DC test consists of connecting two terminals of the stator to a DC source. Adjust the DC source voltage until the current flowing into the stator windings of the DFIG reaches its nominal value. Then, the value of the DC resistance is deduced from those measurements. Depending on the connection of the stator windings, the value of the per-phase stator resistance R_s is deduced, as shown in Table B.4. The measured parameters of the DFIG during the DC test is depicted in Table B.1; The subscript *dc* indicates the parameter values recorded during the DC test.

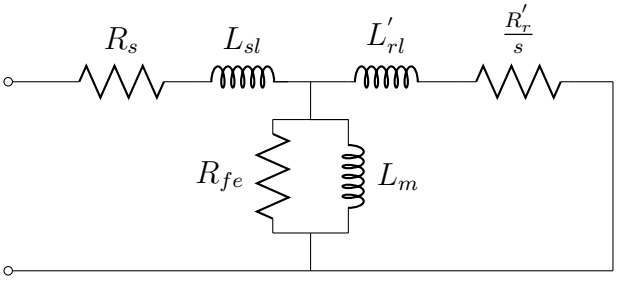

Figure B.1: Equivalent Circuit of the Induction Generator

Table B.1: DC Test Measurement

Measured parameters	values
V_{dc}	13.5 V
I_{dc}	35 A
R_{dc}	0.3857 Ω

B.1.2 Blocked Rotor Test

The simplified equivalent circuit of the DFIG during the locked rotor test is shown in Figure B.2. The locked rotor test helps in determining the stator leakage inductance (L_{sl}), rotor leakage inductance (L_{rl}) and the rotor resistance (R_r'). All these machine parameters are referred to the stator side. When the rotor is blocked, the slip is one. Since the vertical impedance of the simplified equivalent circuit of the DFIG is far higher than that of the horizontal impedance, the vertical impedance of the simplified equivalent circuit is neglected. The short-circuited DFIG is connected to a three-phase variable-voltage source. The voltage is adjusted until the rated current is reached. The measurement from the blocked rotor test are displayed in Table B.2. The expressions below allow the calculation of the above-mentioned parameters

$$R_s + R_r' = R_{br} = \frac{P_{br}}{3I_{br}^2}, \tag{B.1}$$

$$Z_{br} = \frac{V_{br}}{I_{br}} \tag{B.2}$$

and

$$X_{br} = \sqrt{Z_{br}^2 - R_{br}^2}. \tag{B.3}$$

In the above equations, Z_{br} is the equivalent impedance of the equivalent circuit of the DFIG during the blocked rotor test; X_{br} is the imaginary part of Z_{br}; and, R_{br} is the real part of Z_{br}. In case the machine is a wound induction machine the expression below is suggested;

$$L_{rl}' = L_{sl} = \frac{X_{br}}{2\omega} \tag{B.4}$$

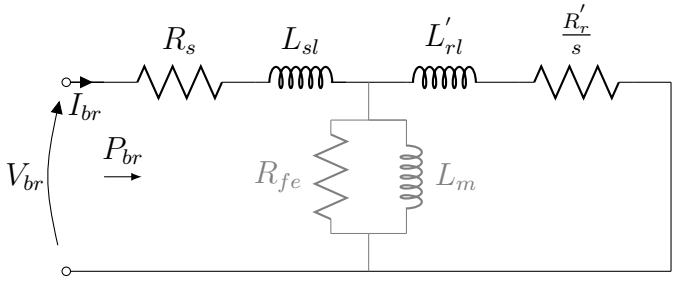

Figure B.2: Equivalent Circuit of the Induction Generator during Blocked Rotor Test

Table B.2: Blocked Rotor Measurement

Measured parameters	values
V_{br}	36.982 V
I_{br}	36.49 A
P_{br}	1285.48 W

where ω is suggested to be 25% of the line frequency. It is worth noticing that in this thesis, only the line frequency has been used in that test due to logistic problem.

B.1.3 No-Load Test

The simplified equivalent circuit of the DFIG during the no-load test is displayed in Figure B.3. The stator of the DFIG is connected to the variable three-phase supply. The supply voltage is adjusted to its rated value causing the machine to rotate at about the synchronous frequency. Hence, the slip is zero. The rotor circuit at the equivalent circuit is open. Assuming that the current flowing through the core resistor R_{fe} is very small, the value of the magnetising inductance will be found using the expressions below, similar to those of Section B.1.2.

$$S_{nl} = 3V_{nl}I_{nl}, \tag{B.5}$$

$$Q_{nl} = \sqrt{S_{nl}^2 - P_{nl}^2}, \tag{B.6}$$

$$X_{nl} = \frac{Q_{nl}}{3I_{nl}^2} = X_{sl} + X_m \tag{B.7}$$

and

$$L_m = \frac{X_m}{\omega_s}. \tag{B.8}$$

where S_{nl} is the apparent power; and Q_{nl} is the reactive power during the test; The subscript nl denotes parameters recorded during the no-load test. Table B.3 displays the measured parameters during the no-load test.

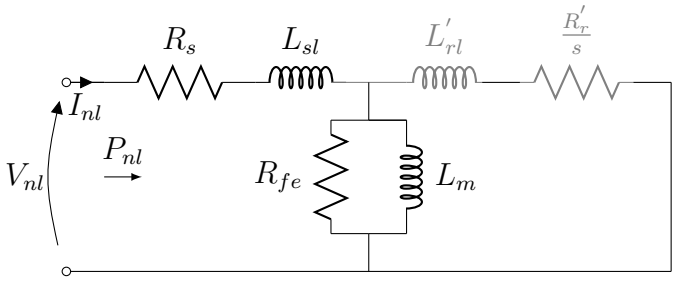

Figure B.3: Equivalent circuit of the induction generator during no-load test

Table B.3: No-Load Test Measurement

Measured parameters	values
V_{nl}	230.07 V
I_{nl}	17.21 A
P_{nl}	1165.4 W

B.1.4 DFIG Parameters In The Lab

The parameters of the DFIG resulting from the tests mentioned in Section B.1.1, Section B.1.2 and Section B.1.3 are displayed in Table B.4 .

Table B.4: Parameters of the DFIG to be used in the laboratory

Measured parameters	values
R_s	0.19285 Ω
L_m	0.04138 H
$L_{sl} = L_{rl}^{'}$	0.00145 H
$R_r^{'}$	0.147595 Ω
stator-rotor windings turns ration	1.7264

B.2 Simulated System Data

Table B.5: IM Parameters

P	3 hp
Measured parameters	values
rated voltage	220 V
shaft speed	1710 rpm
Torque	11.9 Nm
I_b	5.8 A
R_s	0.435 Ω
X_m	26.13 Ω
$X_{sl} = X_{rl}^{'}$	0.754 Ω
$R_r^{'}$	0.816 Ω
J	0.089 Kg m^2

Table B.6: DFIG Parameters

Name-plate:	
Numbers of poles	6
Power	37300 W
Line to line voltage	415 V
speed	1015 rpm
Base values:	
Current	73.386 A
Frequency	50 Hz
voltage	338.846 V
Impedance	4.617 Ω
inductance	0014697 H
Machine paramters:	
L_m	0.03039 H
$L_{sl} = L_{rl}$	0.000867 H
R_s	0.09961 Ω
R_r	0.05837 Ω
Turbine paramters:	
power	55000 W
Wind speed range	6.1-11.35 $\mathrm{m\,s^{-1}}$
Inertia	13.5 $\mathrm{Kg\,m^2}$
r	6.862 m
m	14.48
$C_{p_{opt}}$	0.4412
λ_{opt}	5.66

Appendix C

Design of the AC RL filter

C.1 Design procedure L Filter

It is necessary to point out that the design procedure followed in this section is slightly different from that of the Area product method. The difference lies on the fact that in the Area Product method, after determining the area product value, one can go and found the dimensions of the mechanical E core in the tables. However in this special case where the maximum current is 18.5 A no predefined dimension in the tables are able to satisfy the mechanical constraint. Hence in terms of determining the dimension of the E core, a trial and error method has been used to satisfy the mechanical constraints (when choosing the dimensions of the E cores) as it will be seen in the following sections.

C.1.1 Electrical Analysis

Assume the voltage across the inductor shown in Figure C.1 and current flowing through it, are sinusoidal waveform pulsating at line frequency ω. The maximum voltage across the inductor is given by

$$V_m = \omega \Phi_m N, \tag{C.1}$$

where V_m, ω and Φ_m are the maximum voltage amplitude, the line frequency and the maximum magnetic flux in the core of the inductance, respectively.

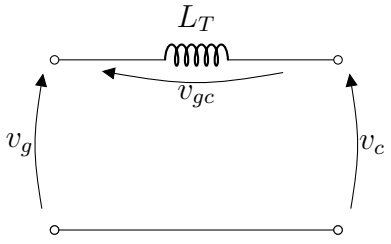

Figure C.1: Per-phase L filter scheme

The magnitude of the flux is given by

$$\Phi_m = A_c B_m, \tag{C.2}$$

where A_c is the cross-sectional area of the magnetic core; B_m is the magnetic flux density. Substituting Equation (C.2) into Equation (C.1) then rearranging it in terms of the cross-sectional area of the magnetic core yields

$$A_c = \frac{LI_m}{NB_m}, \tag{C.3}$$

where I_m is the maximum current through the conductor.

C.1.2 Mechanical Analysis

For the EE core configuration, not only all the N conductors should fit into the windows area but also, the bobbin, the air area, etc. Therefore, the factor of utilisation of the window area should be less than one. This leads to the expression below;

$$NA_w \leq K_u W_a, \tag{C.4}$$

where A_w is the cross sectional area of the conductor; $0.3 \leq K_u \leq 0.7$ is the utilisation factor; W_a is the window area.

By multiplying the Equation (C.4) and Equation (C.3), it yields that the area product is given by

$$A_p = W_a A_c = \frac{LI_m A_w}{B_m K_u}, \tag{C.5}$$

where A_p is the area product. In Equation (C.5), one can found that the area product includes mechanical and electrical constraints.

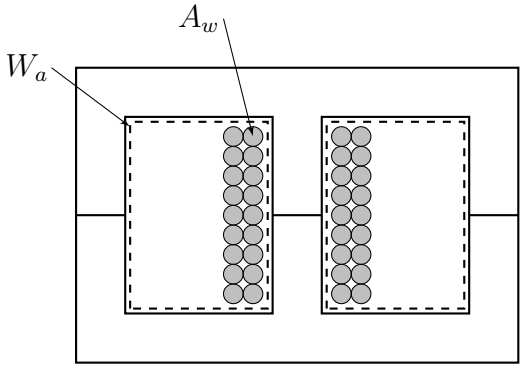

Figure C.2: EE core frontal scheme

C.1.3 Magnetic Analysis

Whenever a core is excited the fringing flux appears around the air gap since the line flux bulge outward when passing through non-magnetic materials. The fringing flux effect is displayed in Figure C.3(a). The magnetic equivalent circuit of the EE core is displayed in Figure C.3(b). The magnetic analysis takes the fringing flux effect into consideration. Using the continuity of the flux inside the core yields

$$\phi_c = \phi_g + \phi_f, \tag{C.6}$$

where ϕ_c is the flux in the core; ϕ_g is the flux in the air-gap; ϕ_f is the fringing flux. The permeance of the core is given by

$$\mathcal{P}_c = \frac{1}{\mathcal{R}_c} = \frac{\mu_r \mu_0 A_c}{l_c}, \tag{C.7}$$

where $\mathcal{P}_c$ is the permeance of the core; $\mathcal{R}_c$ is the reluctance of the core; μ_r is the relative permeability; μ_0 is the free-space permeability; l_c is the flux path length in the core.

The permeance of the the air-gap is given by

$$\mathcal{P}_g = \frac{1}{\mathcal{R}_g} = \frac{\mu_0 A_c}{l_g}, \tag{C.8}$$

where $\mathcal{P}_g$ is the permeance of the air gap; $\mathcal{R}_g$ is the reluctance of the air-gap; l_g is the air-gap length. The permeance of Fringing area is given by

$$\mathcal{P}_f = \frac{1}{\mathcal{R}_f} = \frac{\mu_0 A_f}{l_f}, \tag{C.9}$$

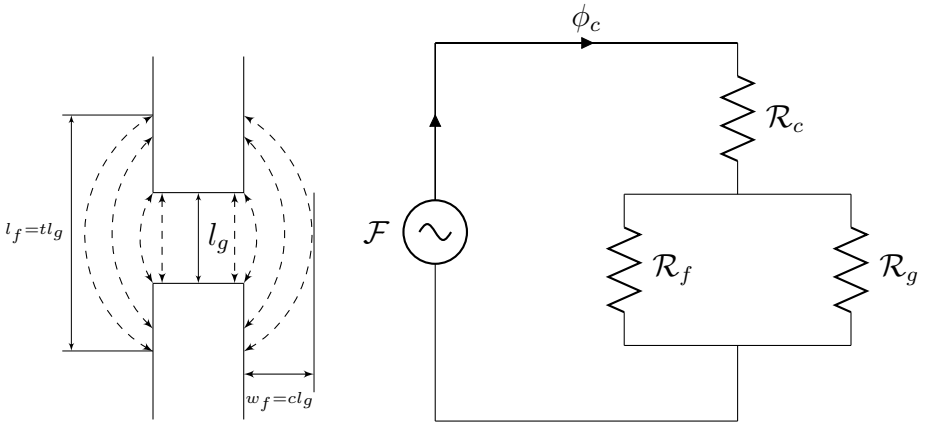

Figure C.3: Fringing flux effect: (a) Fringing flux illustration ; (b) Magnetic equivalent circuit

where $\mathcal{P}_f$ is the permeance of the fringing area; $\mathcal{R}_f$ is the reluctance of the fringing area; l_f is the effective path length of the fringing flux; A_f is the fringing flux area. The total permeance at the air-gap is given by

$$\mathcal{P}_{gf} = \mathcal{P}_g \underbrace{\left(1 + \frac{\mathcal{P}_f}{\mathcal{P}_g}\right)}_{F_f}. \tag{C.10}$$

A closer look at Figure C.3(a), shows that the air-gap length is proportional to the mean width of the fringing as well as to the effective path length of the fringing flux. From Equation (C.10), The fringing flux factor (F_f) is deduced as shown below;

$$F_f = 1 + \frac{A_f}{A_c t}, \tag{C.11}$$

where t is the ratio of the effective length of the fringing area (l_f) and the air gap length. The total reluctance of the EE core is given by

$$\mathcal{R}_T = \mathcal{R}_c + \mathcal{R}_g \parallel \mathcal{R}_f = 1 + \frac{1}{\mathcal{P}_{gf}}. \tag{C.12}$$

Substituting the Equation (C.10) into Equation (C.12) yields

$$\mathcal{R}_T = \frac{l_g}{\mu_0 A_c}\left(\frac{l_c}{\mu_r l_g} + \frac{1}{F_f}\right). \tag{C.13}$$

The inductance value including the fringing flux effect is given by

$$L = \frac{N^2}{\mathcal{R}_T}. \tag{C.14}$$

The cross-sectional area of the core is given by

$$A_c = ED, \tag{C.15}$$

where E and D are the mechanical dimensions of the E core displayed in Figure **??**. The cross-sectional area of the fringing area is given by

$$A_f = (E + 2cl_g)(D + 2cl_g) - ED \tag{C.16}$$

where C,F are he mechanical dimensions of the E core displayed in Figure C.4; c is the ratio of the mean width of the fringing area (ω_f) and the air-gap length. Substituting Equation (C.13) into Equation (C.14) without considering the fringing flux effect then rearranging it in terms of the air-gap length, it yields

$$l_g = \frac{\mu_o A_c N^2}{L} - \frac{l_c}{\mu_r}. \tag{C.17}$$

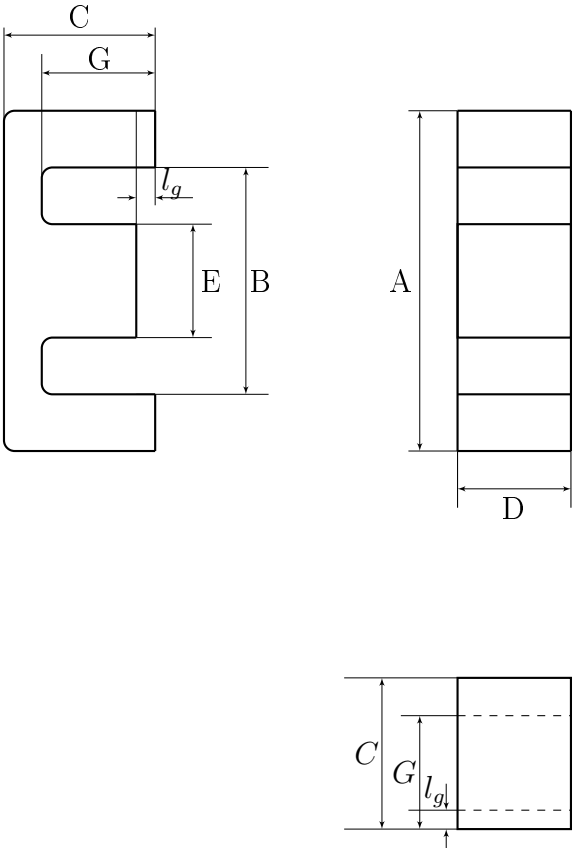

Figure C.4: E core mechanical scheme

On the other hand, when considering the fringing flux effect, the air-gap length is given by

$$l_g = \frac{\mu_o A_c F_f}{L}(N^2 - \frac{l_c L}{\mu_r \mu_0 A_c}). \tag{C.18}$$

Substituting Equation (C.15) and Equation (C.16) into Equation (C.11), the fringing factor is given by

$$F_f = 1 + \frac{2cl_g(D + E2cl_g)}{tED}. \tag{C.19}$$

C.2 AC Filter Design Procedure

The design procedure is as follows;

1. For a fixed I_m, N, B_m, L the cross sectional area A_c is deduced using Equation (C.3);

2. The window area W_a is deduced using Equation (C.4) with the choice of the conductor, then the dimensions of the E core are deduced;

3. Determination of the air gap length without considering the fringing flux effect using Equation (C.17);

4. An iterative calculation between Equation (C.19) and Equation (C.18) is conducted until the air-gap length and the fringing flux converge.

C.3 Design Results

The filter has been designed to meet the following specifications: $L_i = 8.75$ mH, $I_m = 18.5$ A, $f = 50$ Hz. The E core is made from M 400-50A material type. The E core dimensions are given in Table C.1. It can be seen from Table C.2 that the measured inductance (L_m =8.8 mH) is approximately similar to that of the design specifications. The picture of the built filter is depicted in Figure C.5.

Table C.1: E core dimensions

E core dimensions	Values
A	12.11 cm
B	9.42 cm
C	5.055 cm
G	3.695 cm
$E = D$	2.69 cm
l_g	0.105 cm

Table C.2: Inductance values

Inductance values	Values
L_i	8.75 mH
L_m	8.8 mH

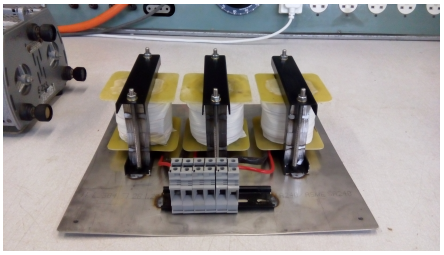

Figure C.5: Built Filter

Appendix D

Software of the Proposed Control Strategy

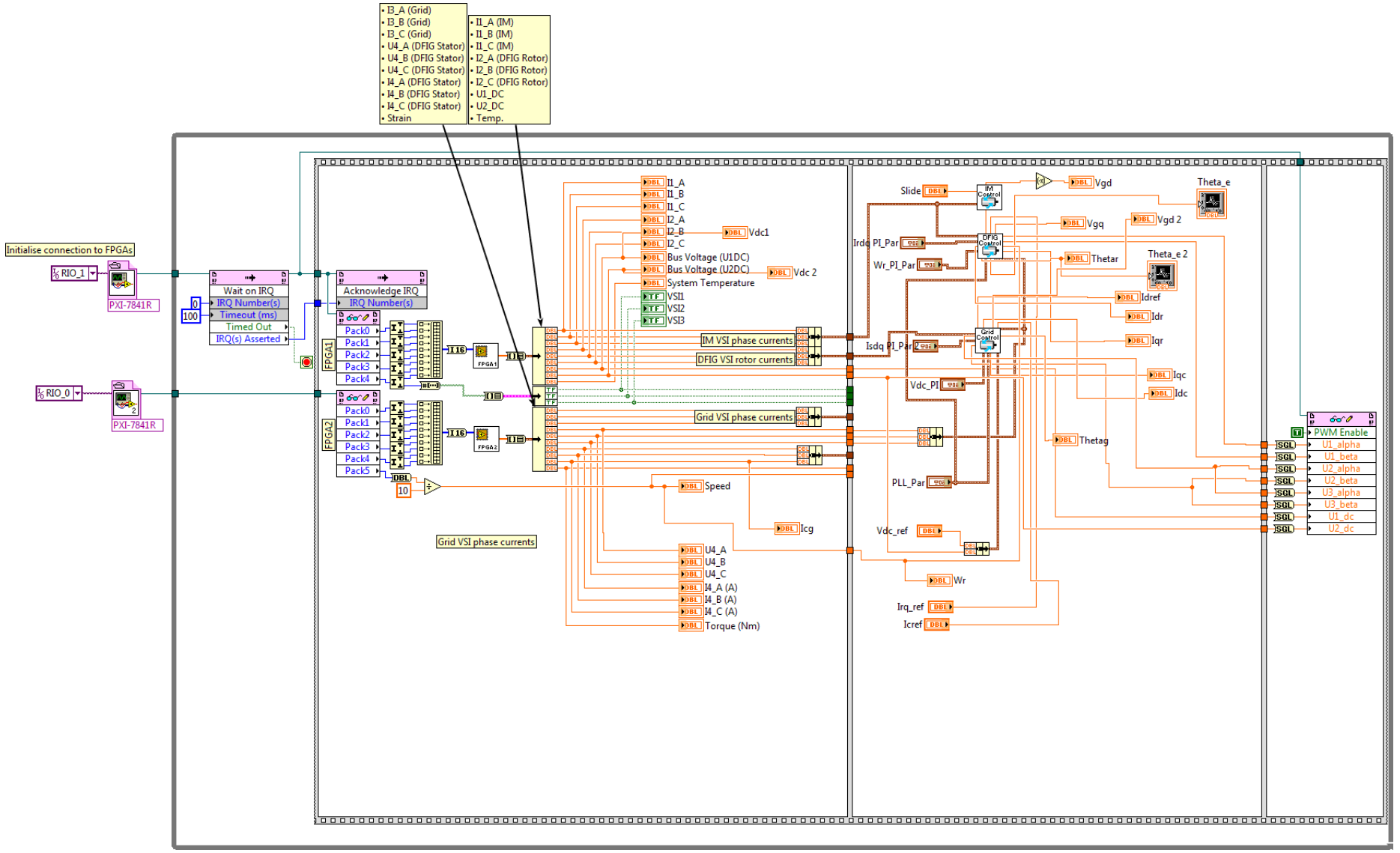

Figure D.1: Inner PI controller software in LabVIEW

D.1 Grid-Side Controller Software in LAbVIEW

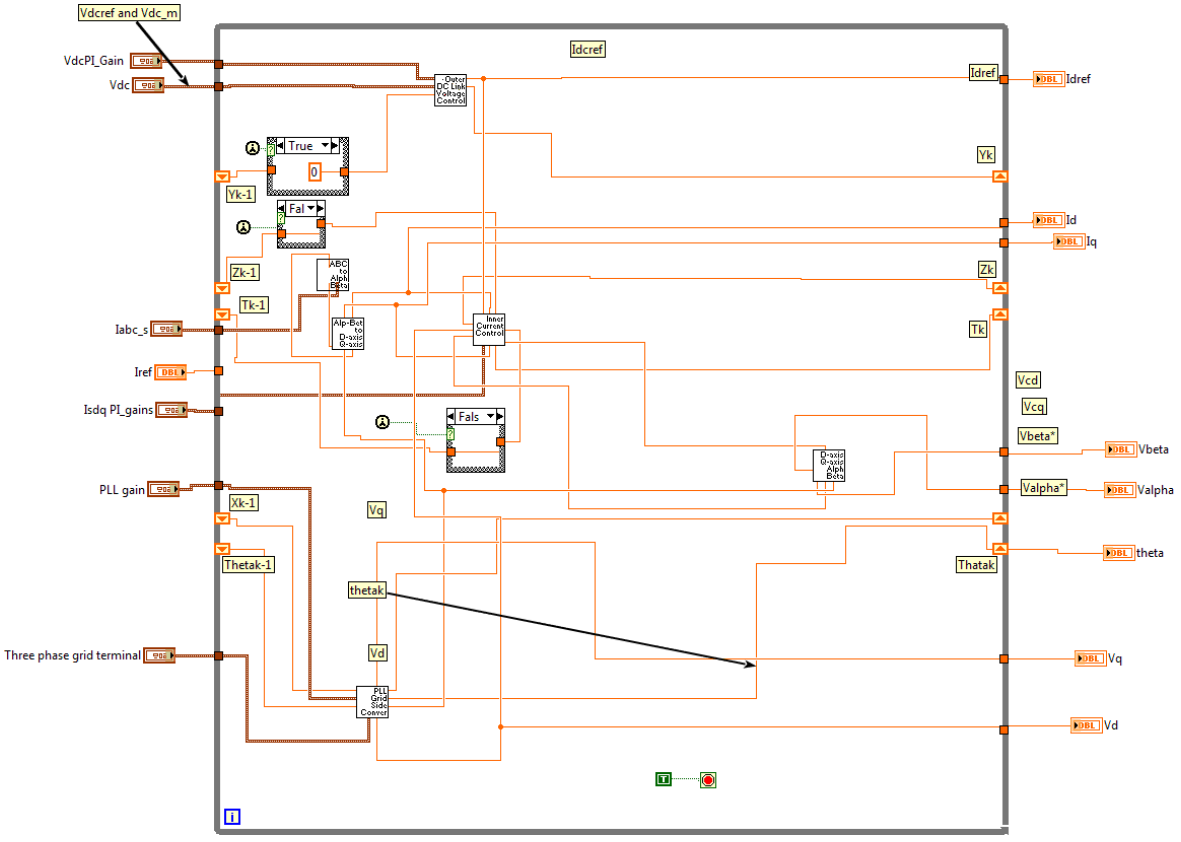

Figure D.2: Grid-side controller software in LabVIEW

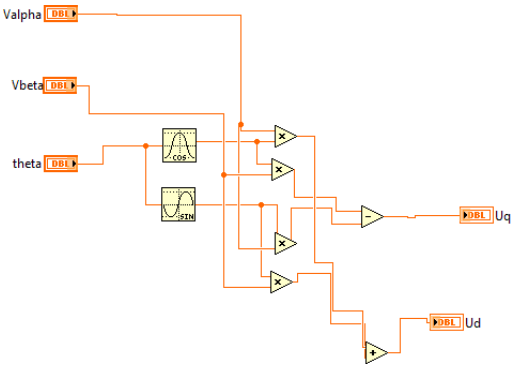

Figure D.3: ABC to $\alpha\beta$ components software in LabVIEW

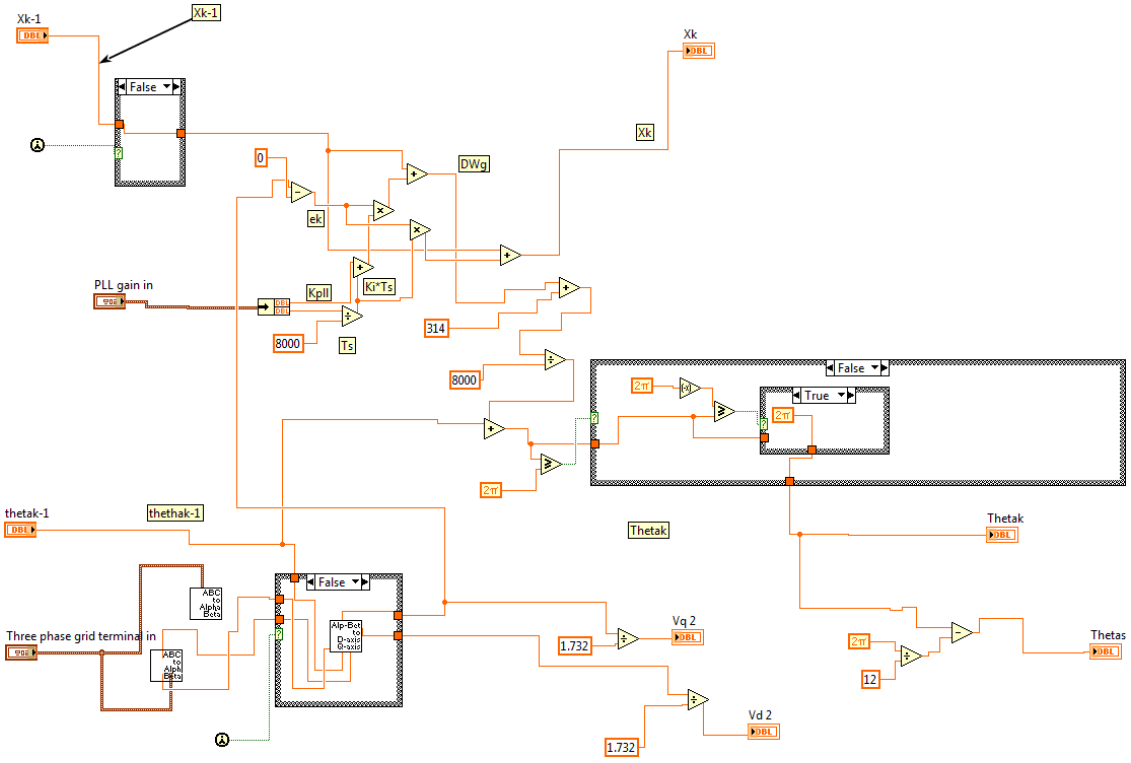

Figure D.4: Phase locked loop VI in LabVIEW

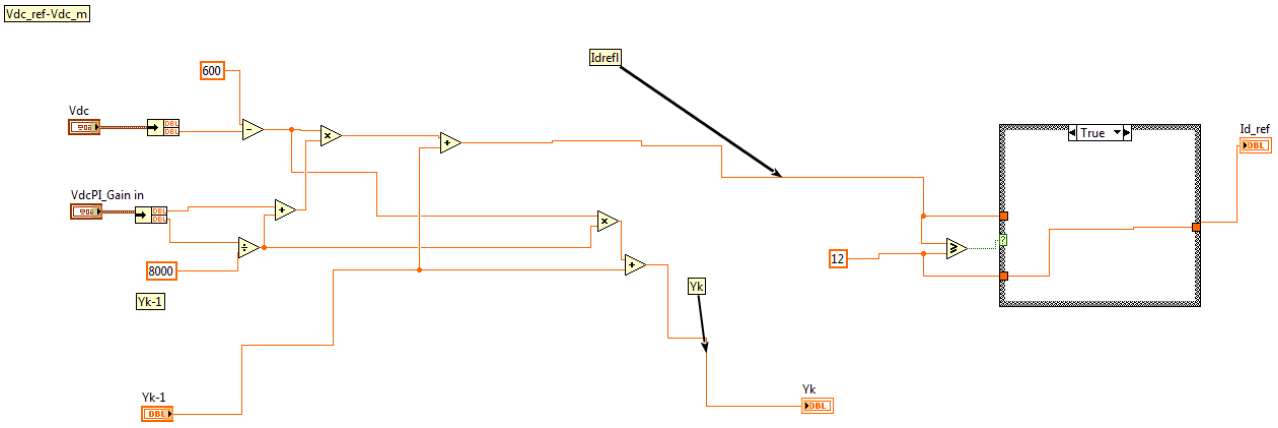

Figure D.5: Outer PI controller VI in LabVIEW

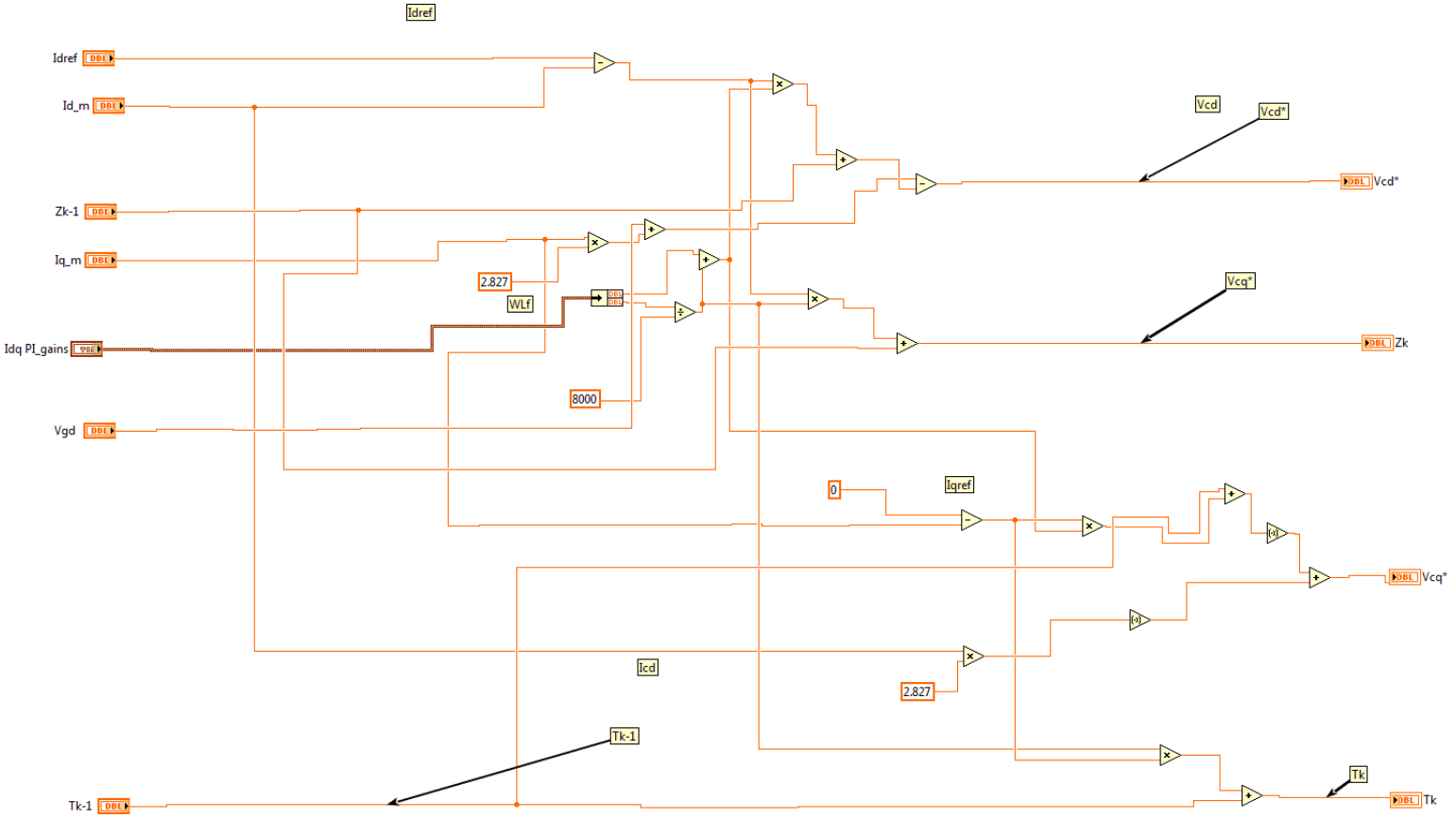

Figure D.6: Inner PI controller VI in LabVIEW

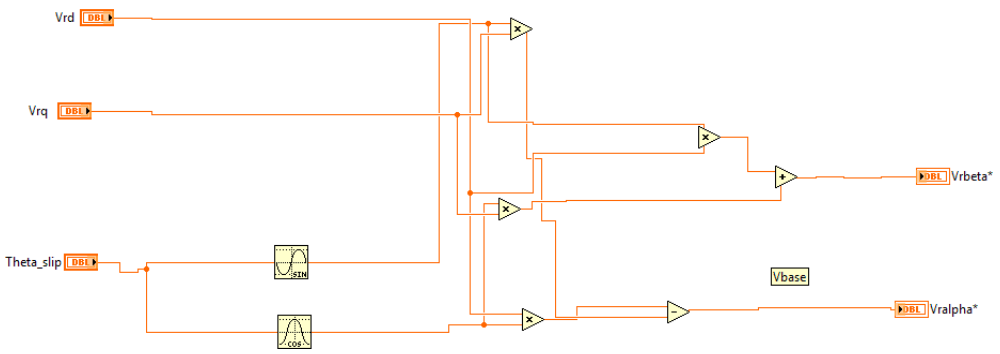

Figure D.7: ABC to $\alpha\beta$ components VI in LabVIEW

D.2 Rotor-side controller software in LabVIEW

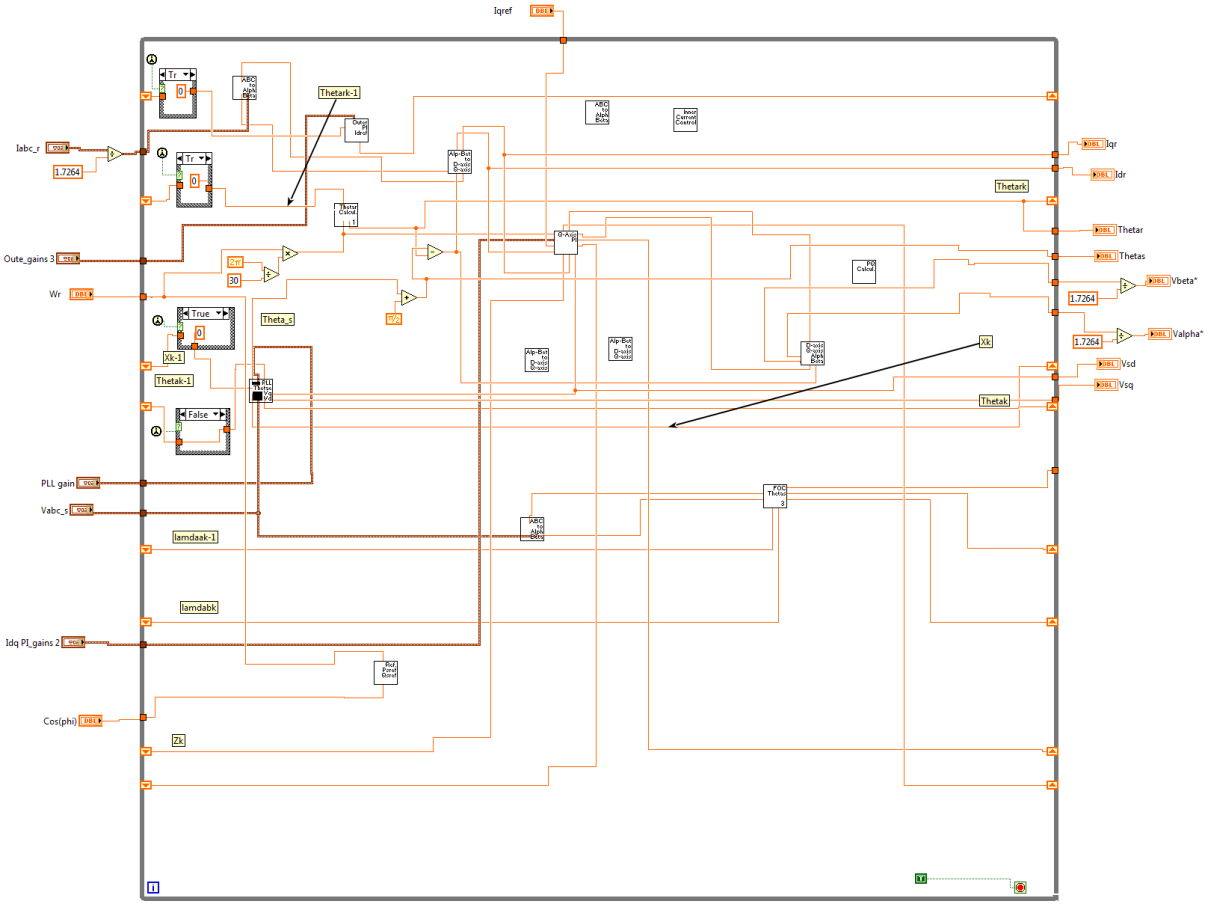

Figure D.8: Rotor-side controller VI in LabVIEW

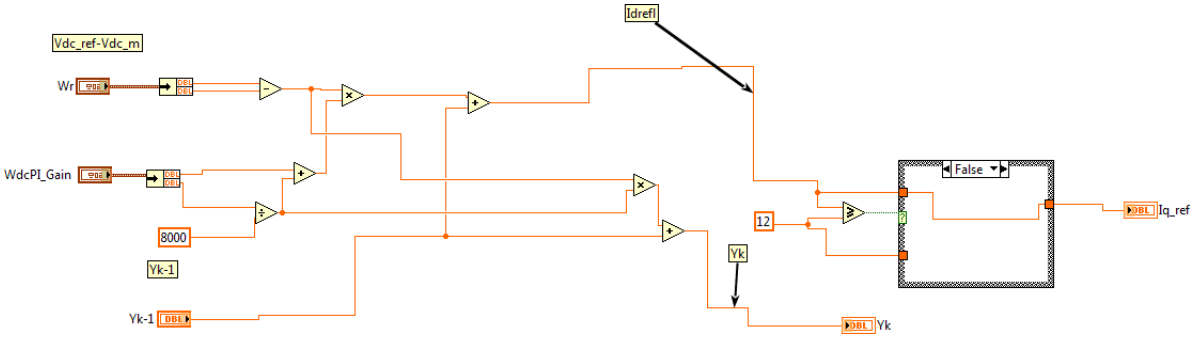

Figure D.9: Clark transformation VI in LabVIEW

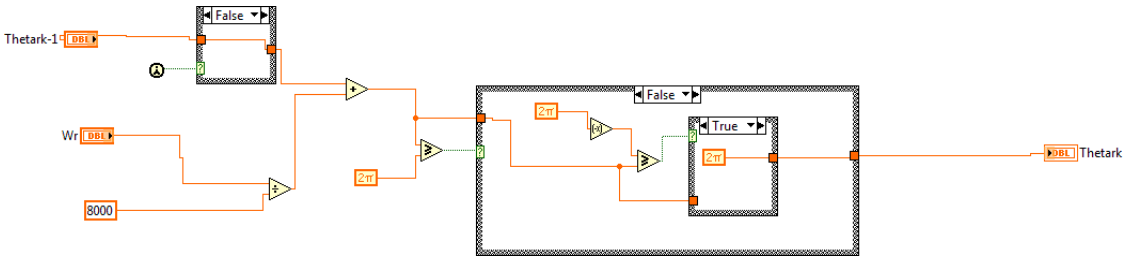

Figure D.10: Rotor angle calculation VI in LabVIEW

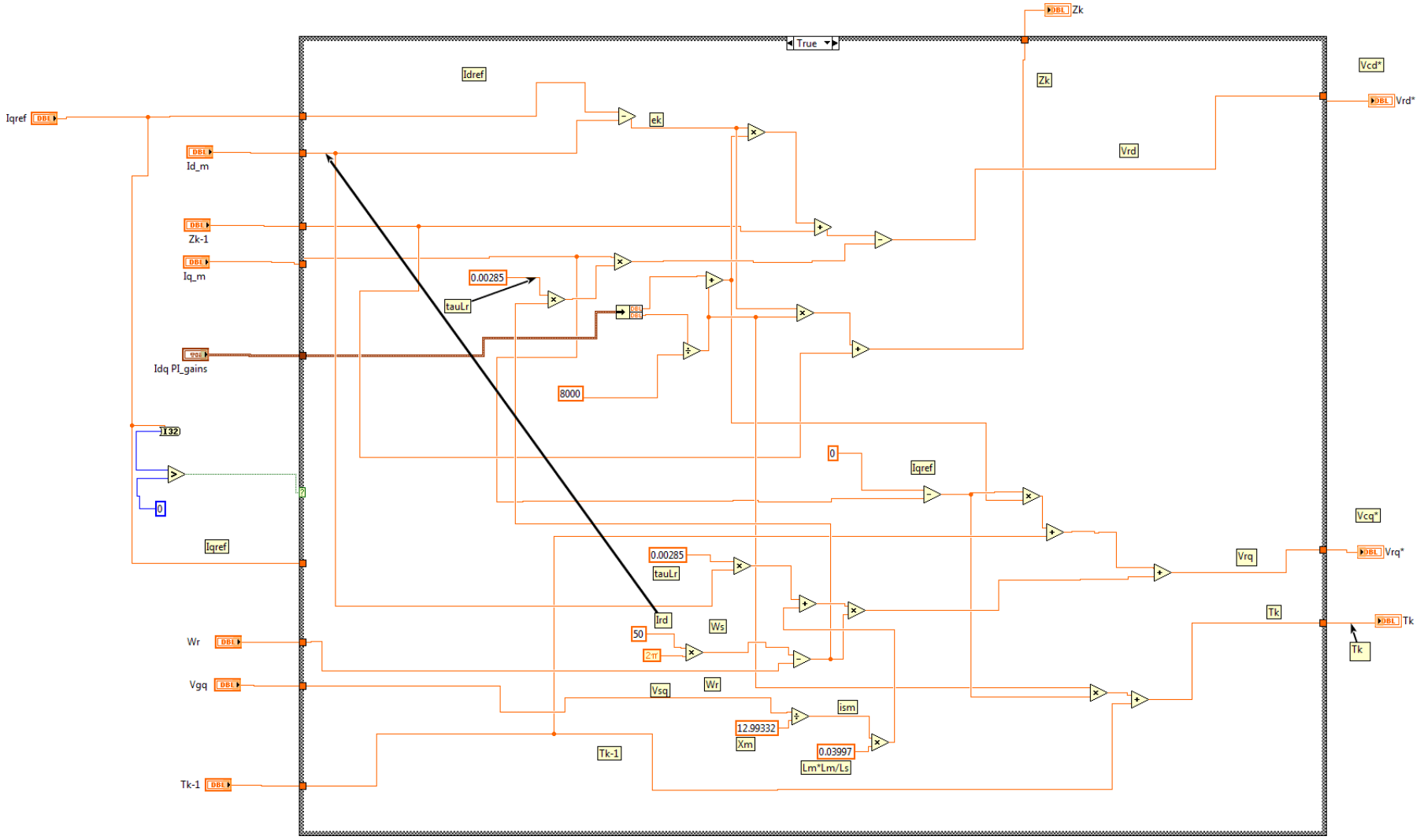

Figure D.11: Inner PI controller VI in LabVIEW

Appendix E

The SIMULINK Models

E.1 GSC with LCL Filter

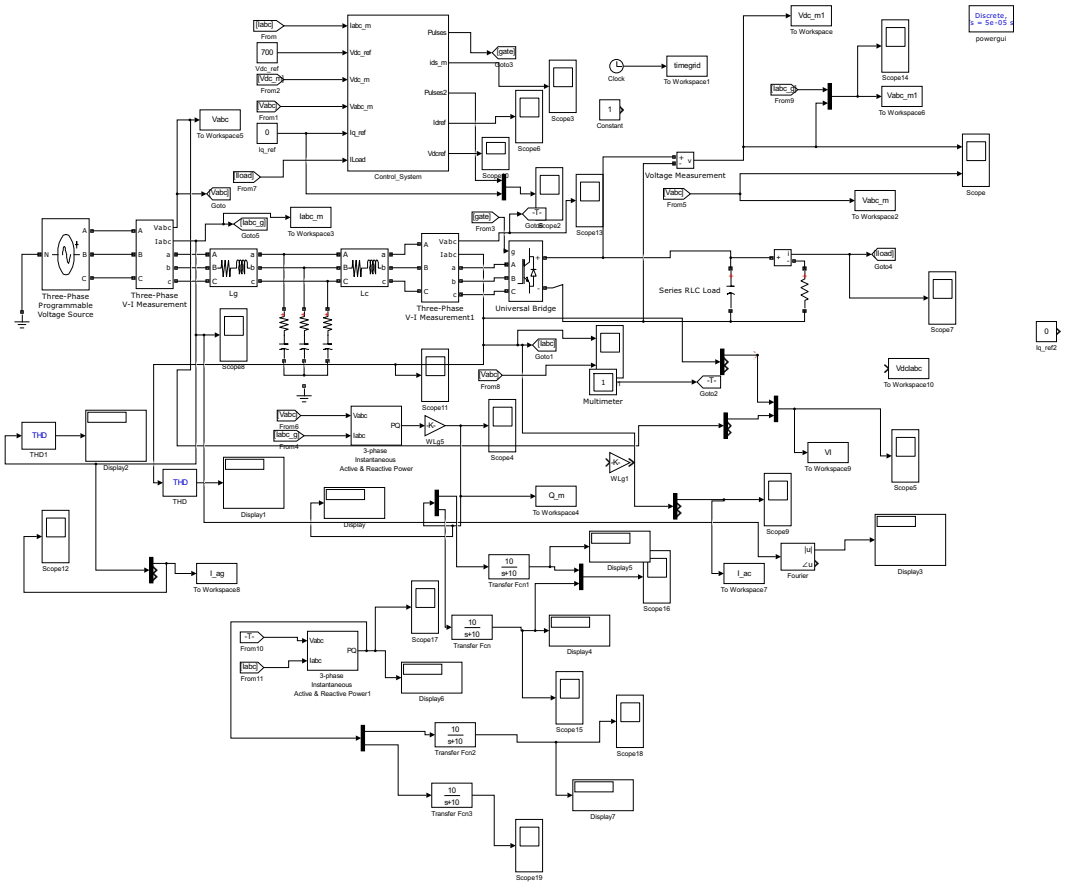

Figure E.1: Grid-connected VSC

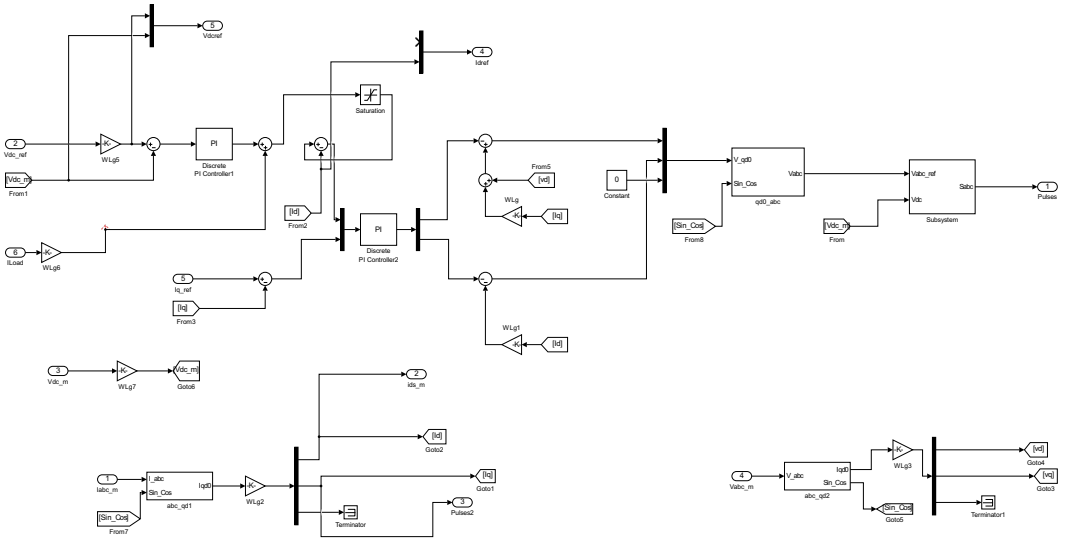

Figure E.2: Control system

E.2 GSC with L Filter

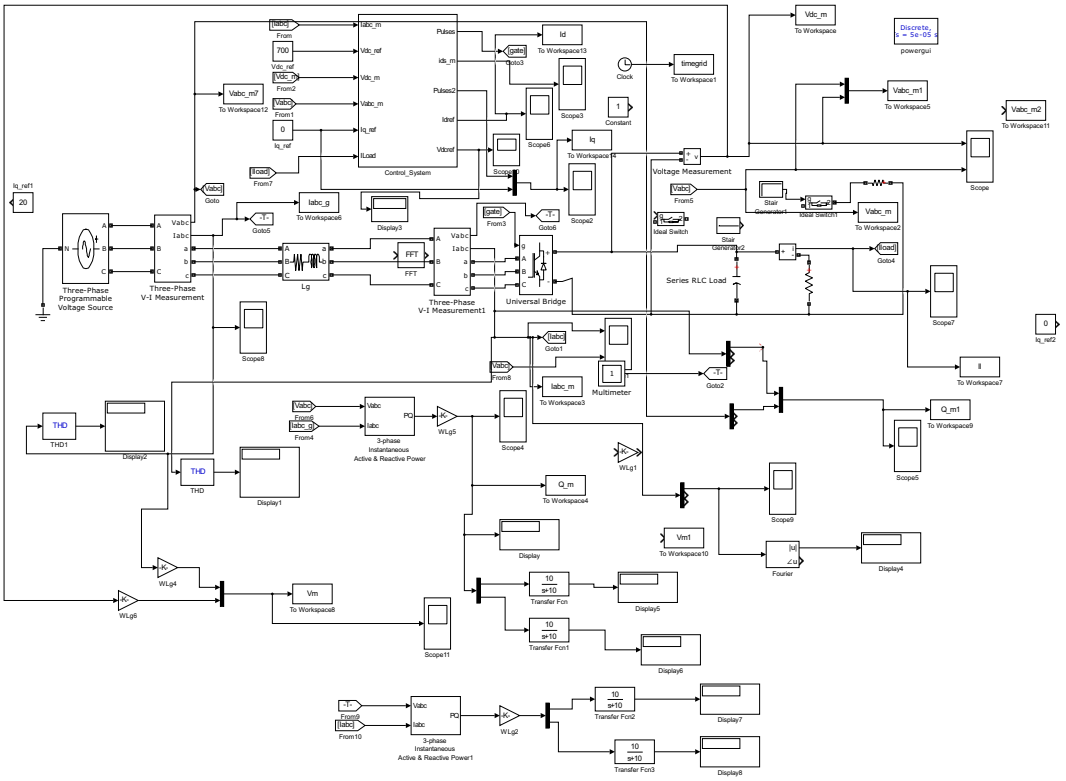

Figure E.3: Grid-connected VSC

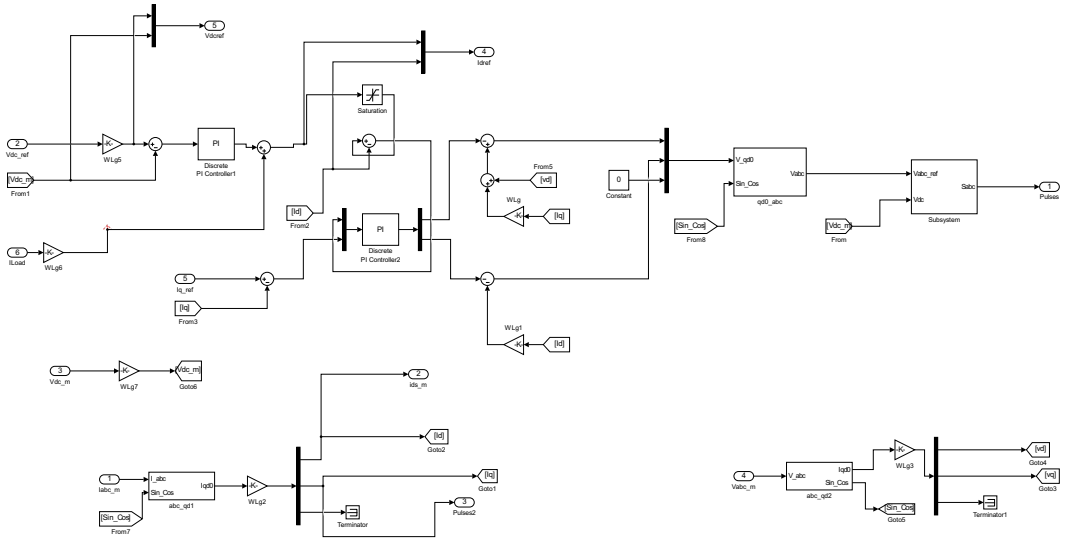

Figure E.4: Control system

E.3 Stand-Alone RSC

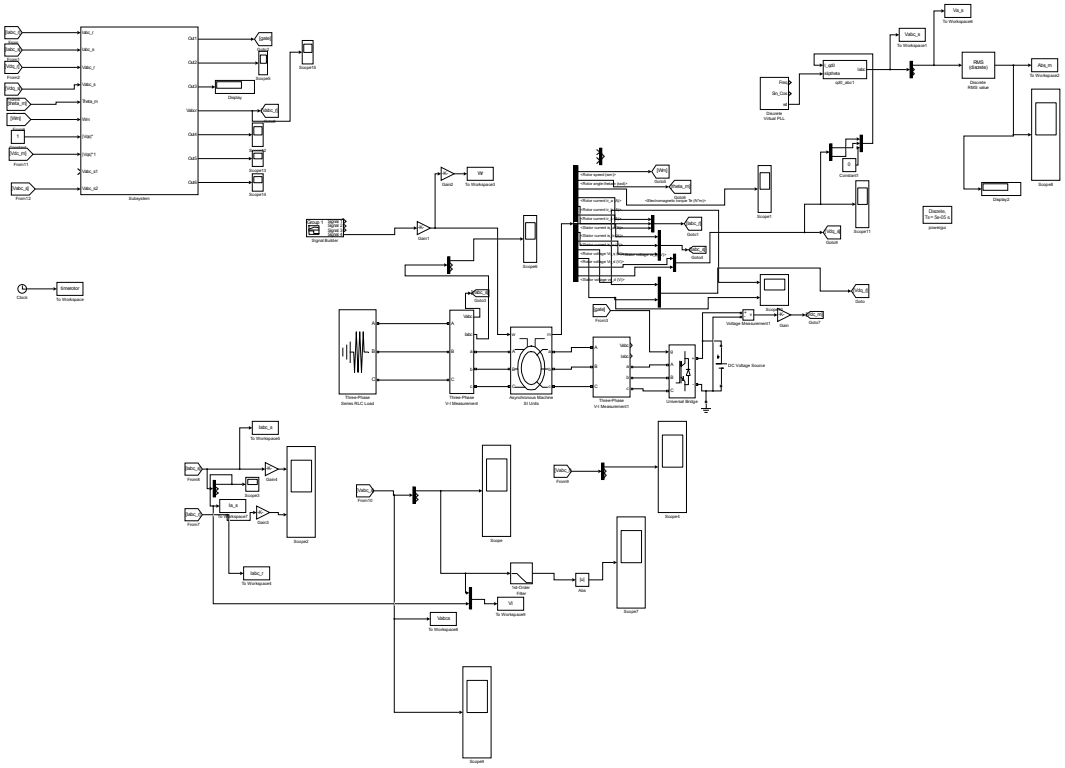

Figure E.5: Rotor-side converter in Stand-alone DFIG system

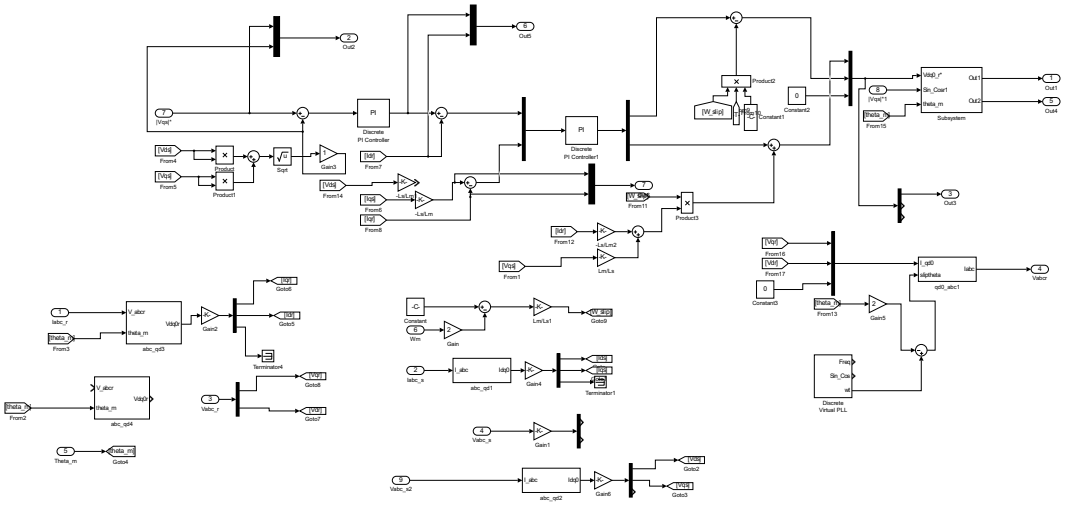

Figure E.6: Control system

E.4 Grid-Connected RSC

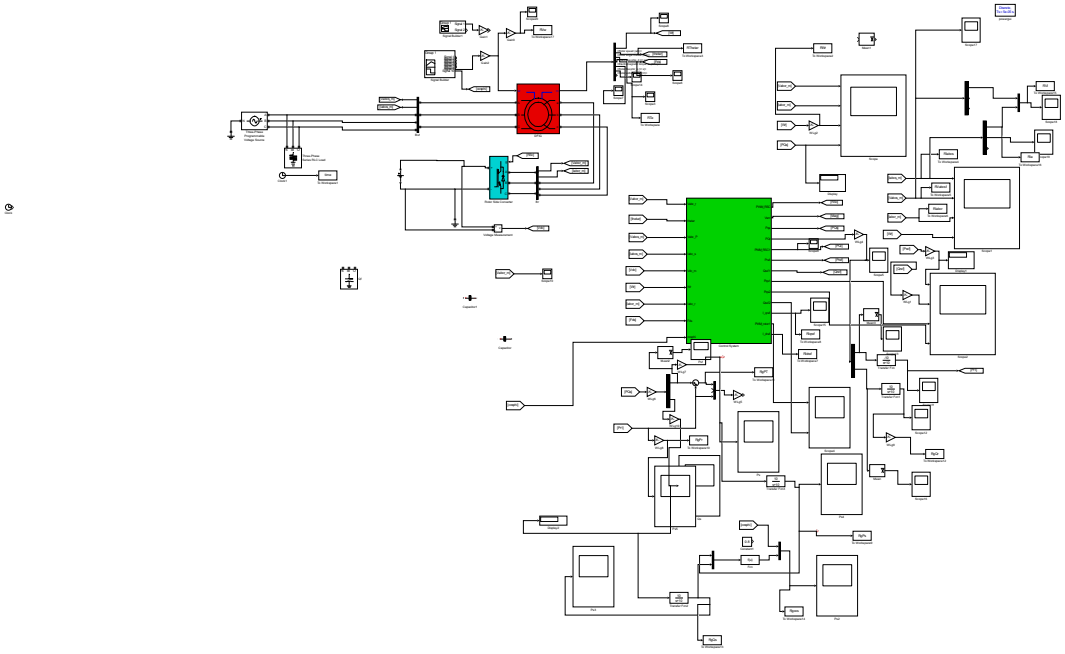

Figure E.7: Rotor-side converter of a grid-connected DFIG system

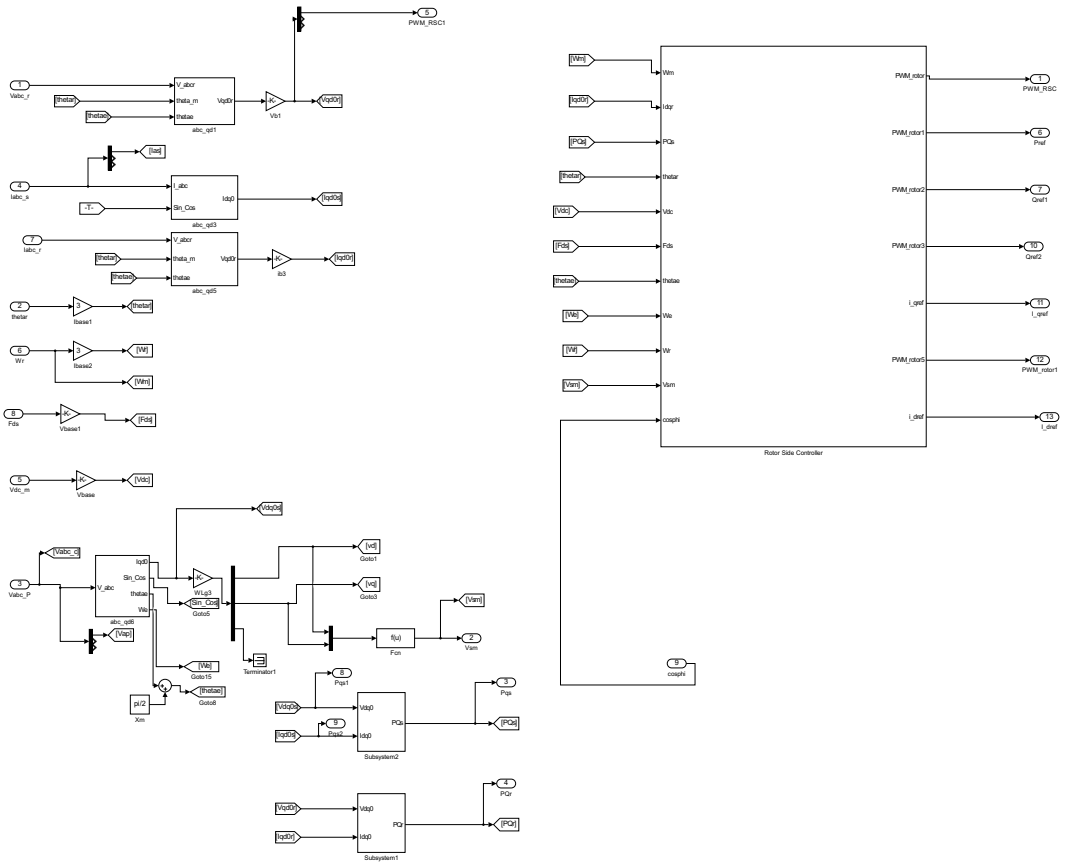

Figure E.8: Control system

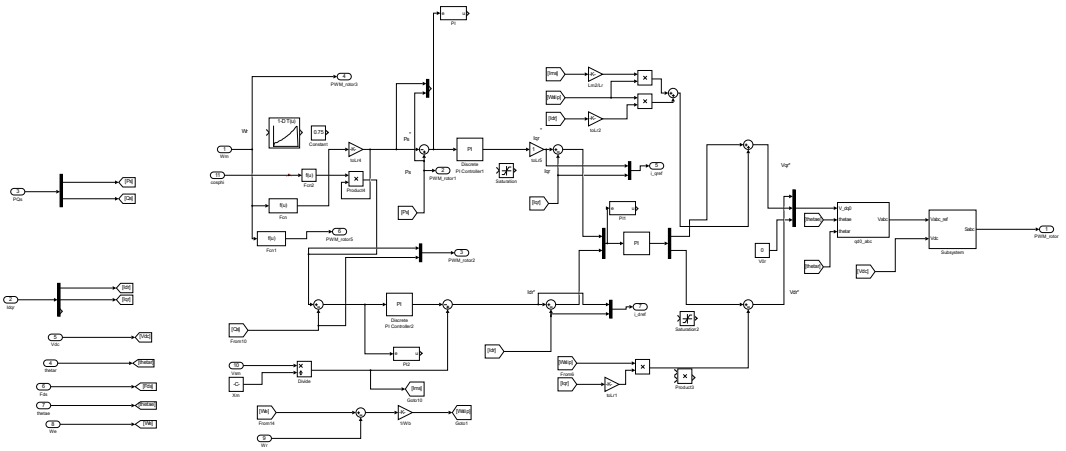

Figure E.9: Control system